Shahrood University of Technology
Faculty of Mining, Petroleum and Geophysics

A model-based approach to the common-diffraction-surface stack

To receive academic degree for

Doctor of Philosophy in Mining and Geophysics

Faculty of Mining, Petroleum and Geophysics

Shahrood University of Technology
Shahrood

DISSERTATION
Of

Hashem Shahsavani

Date of presentation:	08. September 2011
First supervisor :	Dr. Iradj Piruz
Second supervisor:	Dr. Jürgen Mann
Advisor :	Dr. Prof. Peter Hubral

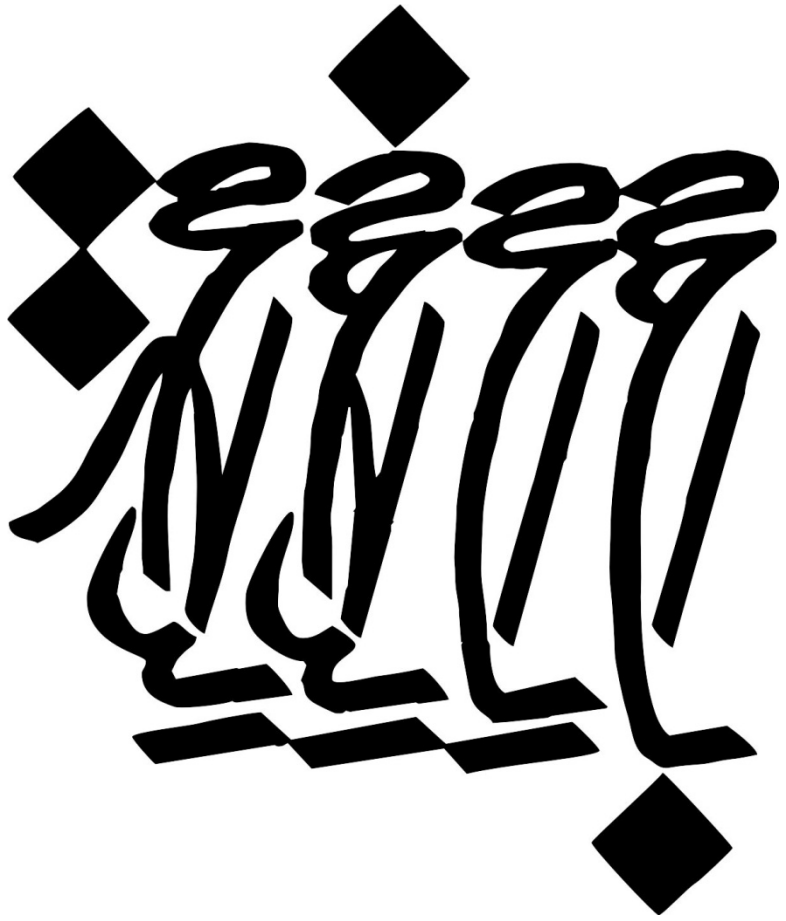

Acknowledgments

I wish to express my deepest gratitude to my supervisor Dr. Iradj Piruz and co-supervisor Dr. Juergen Mann for their guidance, advice, criticism, encouragements and insight through the research. I would also like to thank Prof. Peter Hubral for his suggestions and comments.

I would like to thank Dr. Mehrdad Soleimani for sharing his valuable time and for giving me helpful information. I would like to thank the officials and other staff members of Faculty of Mining, Petroleum and Geophysics who rendered their help during the period of my research. Finally I appreciate my parents and my wife for their patience and supports along my research.

Abstract

The Common-Reflection-Surface stack method parameterizes and stacks seismic reflection events in a generalized stacking velocity analysis. The common 2-D implementation of the Common-Reflection-Surface stack is able to consider a discrete number of events contributing to a given stack sample such that conflicting dip situations can be handled. However, the reliable detection of such conflicting dip situations is difficult and missed contributions to the stacked section might cause artifacts in a subsequent poststack migration, just as unwanted spurious events that might be introduced by this approach. This is deleterious for complex data where prestack migration is no viable option due to its requirements concerning the accuracy of the velocity model. There, we might have to rely on poststack migration, at least for the first structural image in the depth domain.

In addition to the approach which considers a small number of discrete dips, the conflicting dip problem has been addressed by explicitly considering a virtually continuous range of dips with a simplified Common-Reflection-Surface stack operator. Due to its relation to diffraction events, this process was termed Common-Diffraction-Surface stack. In analogy to the Common-Reflection-Surface stack, the Common-Diffraction-Surface stack has been implemented and successfully applied in a data-driven manner. The conflicting dip problem has been fully resolved in this way, but the approach comes along with significant computational costs. To overcome this drawback I now present a much more efficient model-based approach to the Common-Diffraction-Surface stack which is designed to generate complete stack sections optimized for poststack migration. Being a time-domain stacking process, this approach only requires a smooth macro-velocity model of minor accuracy.

In this thesis I present the results for the Sigsbee 2A data set and for a real data set. Afterwards I compare their poststack-migrated results to their counterparts obtained with

the data-driven Common-Diffraction-Surface approach or the Common-Reflection-Surface stack, respectively. The computational effort is dramatically reduced with model-based Common-Diffraction-Surface approach with even improved results very close to the results of the data-driven Common-Diffraction-Surface approach. The result of new introduced method show that even with the smooth macro-velocity model with minor of accuracy it is possible to obtain the same and even better results than the prestack method which are very sensitive to the accuracy of the velocity model.

Abbreviation

In this thesis, I make use of the following abbreviations that are common in literature about reflection seismic:

CMP	Common-midpoint
ZO	Zero-offset
CO	Common-offset
CR	Common-receiver
CS	Common-shot
CDP	Common-depth-point
CRP	Common-reflection-point
NMO	Normal-moveout
DMO	Dip-moveout
MZO	Migration to zero offset
NIP	Normal-incidence-point
N	Normal
CRS	Common-reflection-surface
CDS	Common-diffraction-surface
PreSDM	Prestack depth migration
PostSDM	Poststack depth migration
PreSTM	Prestack time migration
PostSTM	Poststack time migration
RMS	Root mean square
SNR	Signal-to-noise ratio
FD	Finite-difference
x-D	x-dimension
GFT	Green's function table
OOP	Object oriented programming
I/O	Input/output

Contents

List of Figures

List of Tables

Chapter 1

Introduction

The goal of seismic reflection imaging is to obtain an accurate image of subsurface structures to find hydrocarbons i.e., petroleum, natural gas and other resources such as coal, ores, minerals, and geothermal energy. In general, a seismic reflection data set is produced by generating seismic waves at the surface and measuring particle displacement or one of its temporal derivatives as a function of time at a series of receivers positioned properly.

1.1 Geometry of seismic data acquisition

For a 2-D measurement, a common-shot (CS) array moves along a straight line to obtain all CS sections or gathers. Each trace in a CS gather is defined by its shot coordinate (x_S) and receiver coordinate (x_G). The part of the reflector that is illuminated by each CS array, has overlap with previous and subsequent CS arrays, see Figure 1.1. Together, these CS gathers form a so-called *multi-coverage* data set in (x_S-x_G-t) space where *t* corresponds to the recording time, see Figure 1.2. A multi-coverage data set contains a lot of information as points on reflector cover each other illuminated multiple times.

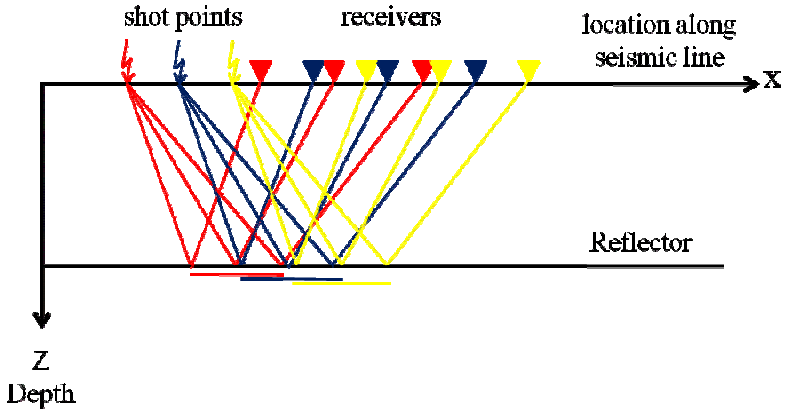

Figure 1.1: For a 2-D measurement the common-shot (CS) array moves along a straight line. Illuminated parts of the reflector which are shown in red, blue, and yellow partly overlap.

By selecting certain traces from multi-coverage data set it would be possible to build up different gathers in order to further processing. Such processing is conventionally performed in midpoint x_m (the center point between shot and receiver location) and half-offset (half distance between shot and receiver). A group of traces with constant x_m+h build up common-receiver (CR) gather and the traces with constant x_m-h build up common-shot (CS) gather. The traces which build CR and CS gathers are shown in Figure 1.2 by brown and yellow colors, respectively.

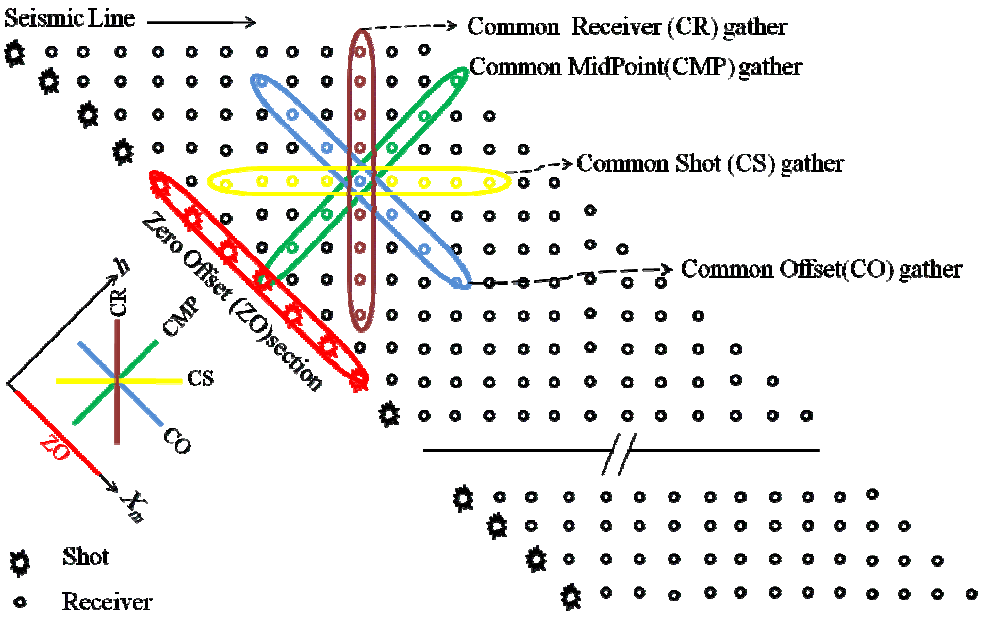

Figure 1.2: 2-D seismic data acquisition: a common-shot (CS) configuration moves along seismic line and generates a multi-coverage data set in three dimensions, x_m midpoint coordinate, h, half-offset and, t, time which is perpendicular to the displayed plane. Different gathers or sections are created by selecting certain traces from multi-coverage data set, see main text.

The traces with the same midpoint but different offsets provide common-midpoint (CMP) gathers. These traces are shown by green color in Figure 1.2. CMP gathers are very important because in this configuration, for a horizontal reflector all rays that contribute to one CMP gather have the same reflection point, see Figure 1.3. Sometimes a CMP gather is also called a common-depth-point (CDP) gather. This is acceptable only when underground layers are horizontal. In such situations the lateral coordinates of CMP and CDP are the same. For dipping reflectors, rays come from smeared area (see Figure 1.4). In such cases the lateral coordinates of CMP and CDP are different.

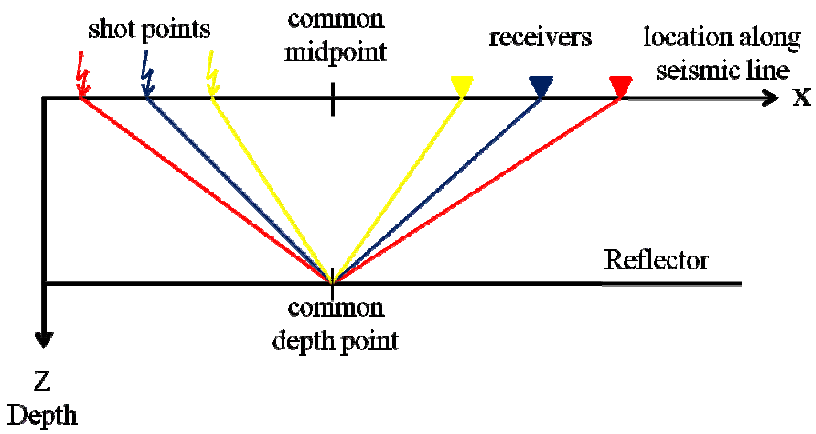

Figure 1.3: All rays are reflected from the same point on the reflector. In presence of a horizontal reflector, x-coordinates of common-midpoint and common-depth-point (CDP) are the same for all shot and receiver pairs.

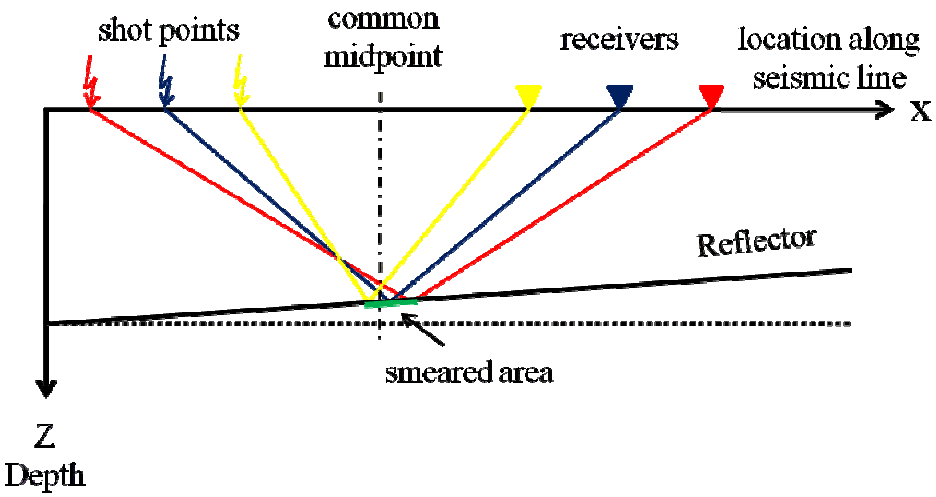

Figure 1.4: For a dipping reflector the rays are reflected from a smeared area.

Another gather which can be created by selecting traces in the multi-coverage data set is a common-offset (CO) gather. A CO gather is a group of traces that is acquired by shifting a single shot-receiver pair with constant offset along the seismic line. As shown in Figure 1.5 all traces in a CO gather have the same half-offset h but different midpoints x_m. These traces are shown in blue in Figure 1.2. A special case of CO gather is the zero-offset (ZO) section. As its name indicates, the offset is equal to zero $h=0$ and, hence, the locations of shot and receiver coincide for all traces, see Figure 1.6. The situation of these traces is shown in red in Figure 1.2. The ZO section is very important for interpretation as it makes an image of subsurface

reflectors in time domain. Indeed, this section shows traveltimes of wavefronts which propagate from the sources and meet the reflection points normally and then back to the receivers which coincide with the sources.

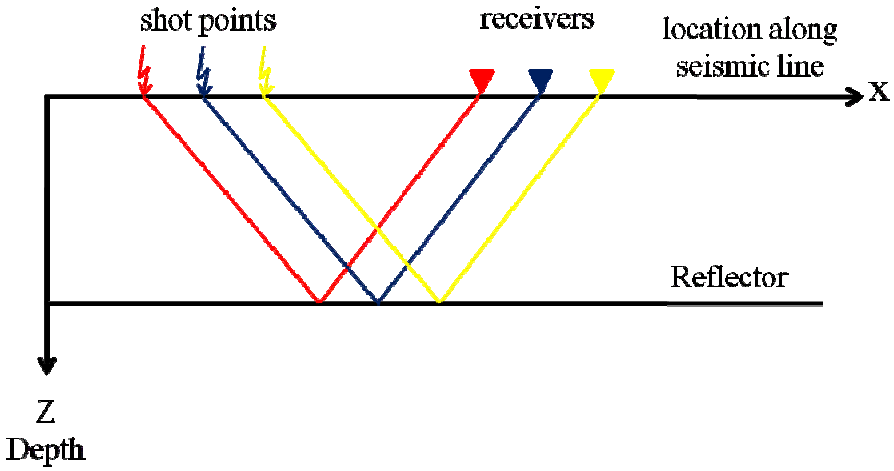

Figure 1.5: For common-offset array, all shot and receiver distances are the same but the midpoints are different.

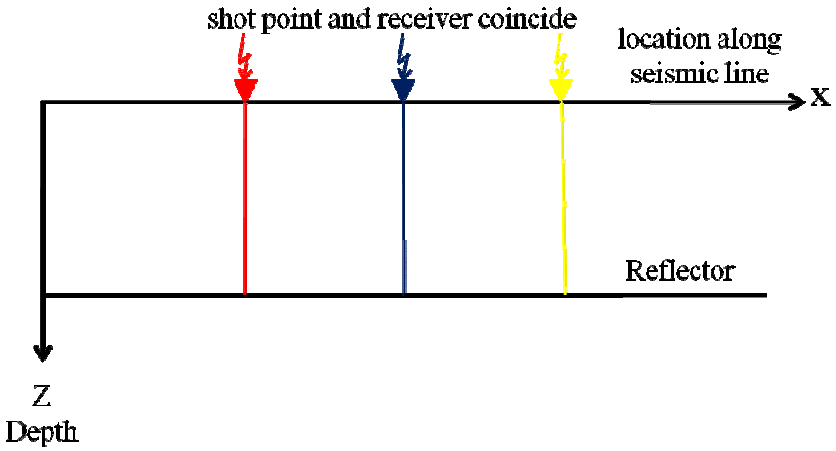

Figure 1.6: The locations of shot and receiver coincide for all traces in ZO section.

The receiver might be placed quite close to sources, at least compared to the target depth to obtain a ZO section. But actually acquiring ZO wouldn't help too much, because it is impossible to perform velocity analysis with ZO only. In addition, shot spacing and, thus, the spacing of actually acquired ZO data is often too coarse, such that we will have spatial aliasing in the ZO section. Accordingly, the ZO section usually has to be simulated which is done by seismic imaging methods.

Due to the wide variety of seismic imaging methods, it is hard to classify them. However, it is possible to organize these methods into two categories: methods which require a priori knowledge of the elastic properties of subsurface layers for next step of processing, so-called *model-based* methods, and methods which do not require a priori knowledge of subsurface elastic properties, so-called *data-driven* methods. In the following section, I will introduce the idea of some standard reflection imaging methods for simulating ZO sections with respect to these two categories.

1.2 Data-driven seismic imaging methods

Reflection imaging process can be accomplished without any knowledge about velocity model of underlying layers and it is possible to achieve all desired properties directly from the acquired data. In this kind of reflection imaging approaches a common task is to use the redundancy in multi-coverage reflection data to simulate a single section. This section is equivalent to the measurement with coincident source and receiver pairs called ZO (see Figure 1.6). In the following, some standard reflection imaging which simulate a ZO section will be introduced.

1.2.1 Common-midpoint stack

In the early days of seismic data processing the available computing power was very limited. Therefore the parameterization of reflection events had to be as simple as possible. The first widely used data-driven approach was introduced by Mayne (1962). He assumes a horizontally layered medium, where the reflection events are considered on different traces in a subset of the pre-stack data, i.e. a CMP gather, see Figure1.2. In this configuration a point in the subsurface placed directly under the CMP location is illuminated several times, see Figure 1.3. The traveltime of single horizontal interface with a homogeneous over burden has shape of hyperbola (Yilmaz, 2001).

$$t^2(h) = t_0^2 + \frac{4h^2}{v_{NMO}^2} \tag{1.1}$$

Here t is the offset-dependent traveltime, t_0 is the ZO traveltime, h is half-offset and v_{NMO} is the normal moveout (NMO) velocity that is identical with the constant velocity in the over burden. In formula (1.1) the traveltime curve is described by using only one parameter, i. e. the well known NMO velocity that is the parameter of

the CMP trajectory in 3-D space (x_m, t, h) of the multi-coverage data set. In presence of *n* iso-velocity horizontal layers, it is still possible to approximate the traveltime curve as long as *h* remains small compare to the depth of the illuminated interface point. For such a horizontally stratified medium, v_{NMO} denotes the root-mean-square (RMS) velocity which is a average velocity of the overburden (Taner and Koehler, 1969). Each interval velocity is weighted with the thickness of the respective depth interval.

In CMP processing, seismic traces are grouped in to CMP gathers. Afterwards for selected CMP gathers the velocities are provided by velocity analysis yielding so-called *stacking velocities* (Yilmaz, 2001). An entire CMP gather is corrected many times with different constant velocities. Then, the coherence value is plotted for all traveltimes and stacking velocities which forms the velocity spectrum. The stacking velocities which yield the maximum coherence value define the best-fit hyperbola for each traveltime. Conventionally, the maxima within velocity spectrum for a CMP are interactively determined in a process called *picking*. This velocity analysis yields a one dimensional stacking velocity function for each CMP gathers by means of interpolation.

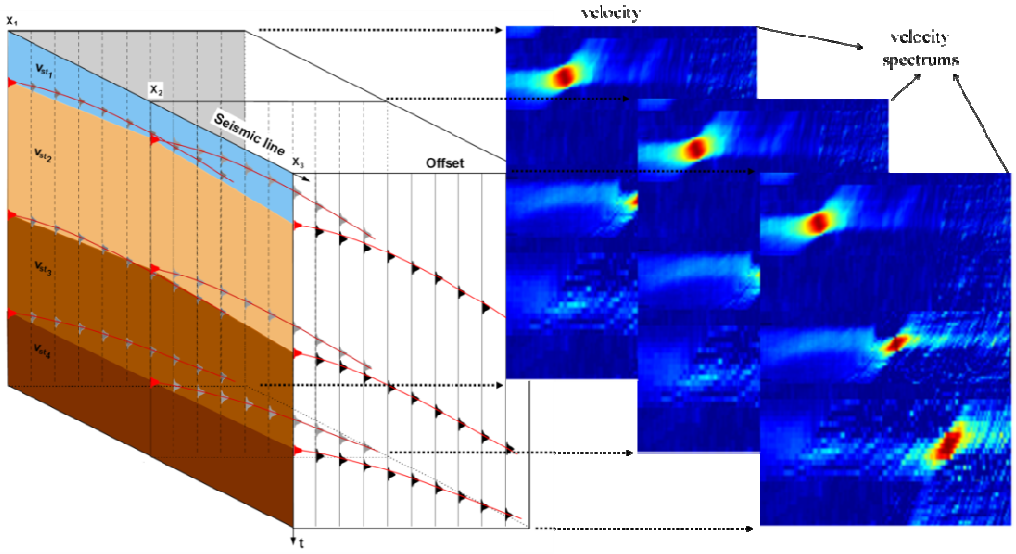

Figure1.7: For each CMP gather, the red curves show the best-fit hyperbolas along the reflection events. In this example, from one picked traveltime to the next in the same trace, the 1-D stacking velocity functions are filled up constantly with the velocities belonging to the next reflection event. A 2-D stacking-velocity model is built up by interpolating between the 1-D velocity functions of chosen CMP gathers (after Koglin, 2001).

By applying velocity analysis to all CMP gathers and interpolating between one dimensional velocity functions it becomes possible to obtain a 2-D velocity model. Figure 1.7 present an example of velocity analysis at the right hand side and a 2-D interpolated stacking-velocity model at the left hand side which also shows the ZO section. Constant stacking velocities between the events have been used in this example. This velocity model is used to perform NMO correction of the multi-coverage data set. The NMO shifts the travel times in a way that the hyperbolas shown by red lines in Figure 1.7 turn to straight lines at the respective $t = t_0$, i. e. the ZO traveltimes. As illustrated in Figure 1.8 after NMO correction the reflection events in CMP gathers become flat so that all traces can be easily summed up, or stacked, to simulate a ZO section. In this way it is possible to reduce the redundancy of data in multi-coverage data set to a single section which corresponds to hypothetical experiments with coincident shot and receiver locations i.e. a ZO section.

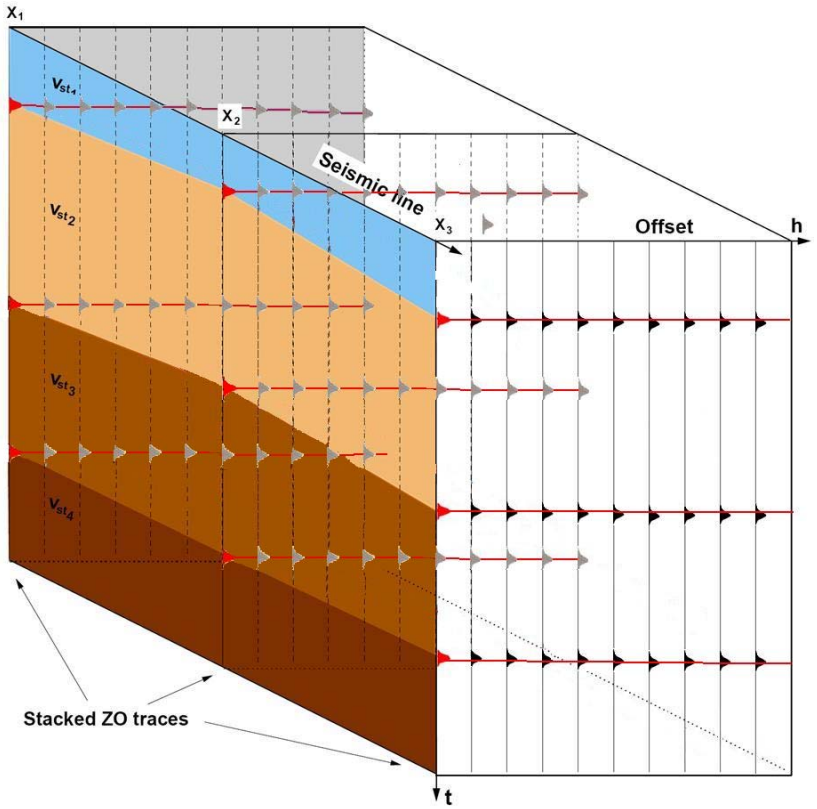

Figure 1.8: All reflection events shown by red lines become flat after NMO correction (after Koglin, 2001).

If the subsurface geology does not violate the assumptions of the CMP method too strongly, the CMP stack collects the energy pertaining to one and the same reflection point at each location in the time domain. Thus, reflection events on the different traces within a CMP gather will sum up constructively and produce a single trace with a signal-to-noise ratio (SNR) that is much higher than that of the individual prestack traces. However, the CMP stack method has some drawbacks. This method cannot handle situation where reflection events, diffraction events, or multiple of various events intersect each other and/or themselves at the same ZO location. Such situations are so-called *conflicting dips* which is the main subject of this thesis.

Additionally, in case of dipping reflectors, the CMP stack combines responses of different reflection points which originate from a smeared area, see Figure 1.4. In such a situation the CMP trajectory deviates from the common-reflection-point (CRP) trajectory. A CRP trajectory specifies the location of the reflection event in the multi-coverage data set which pertains to one and the same reflection point of a reflector. As illustrated in Figure 1.9 the CRP trajectory is, in general, not parallel to the CMP gathers.

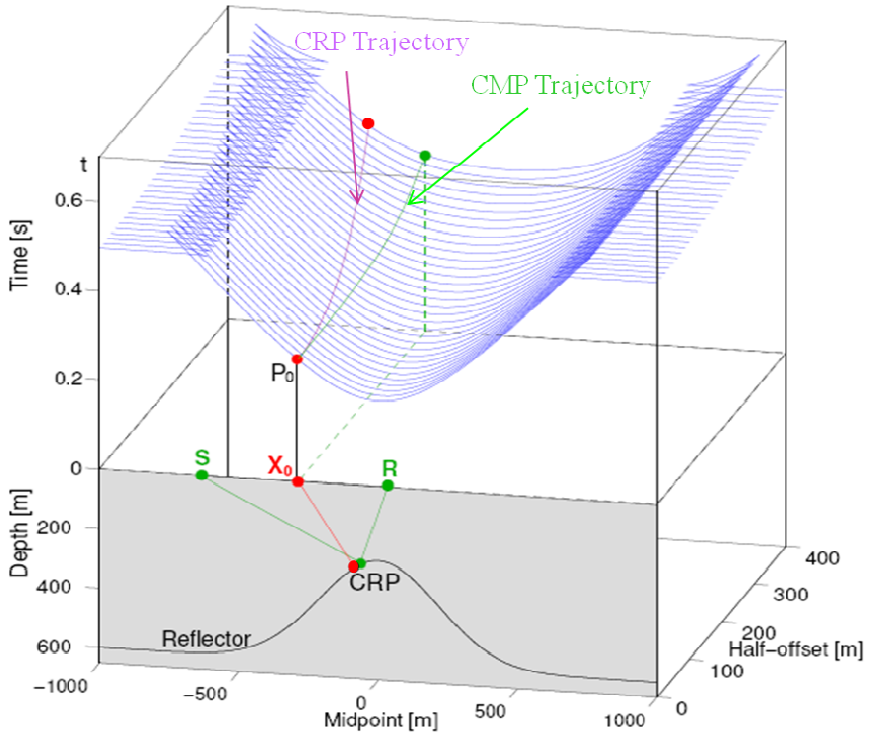

Figure 1.9: The response of a dome-like reflector is illustrated in multi-coverage data set in time domain in blue. In case of a dipping reflector the CRP trajectory, which is shown in magenta, deviates from CMP trajectory indicated in green (Mann et al., 2000).

To overcome the drawbacks of the CMP stack, a new method was introduced to consider the dipping reflectors, the so-called migration to zero offset (MZO) or, in an approximate manner, the normal moveout/dip moveout/stack (NMO/DMO/stack) approach.

1.2.2 Normal-moveout dip-moveout stack or migration to zero offset

In case of dipping reflectors, the dip-moveout (DMO) tries to correct for the reflection point dispersal occurring from the dip of the reflector. From a mathematical point of view, it is possible to divide the NMO/DMO/stack approach into two steps: firstly, the NMO correction within the CMP gather is applied to give an initial estimation of the velocity to remove the influence of the overburden.

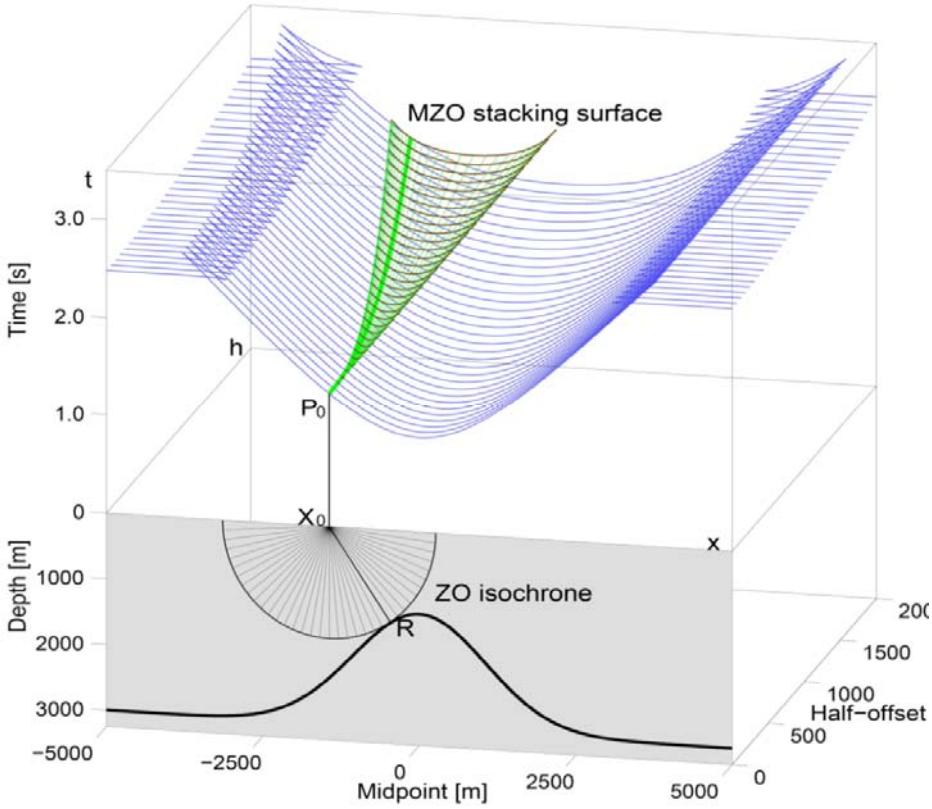

Figure 1.10: Lower half) Dome-like reflector with the reflector being touched at point R by the ZO isochron associated with point P_0. Upper half) CO reflection-time surface (blue) to which the NMO/DMO stack surface for P_0 (in brown) is tangent along the CRP trajectory (in bold green) for point R (Jäger, 1999).

Secondly, one of several different methods (Deregowski, 1986; Hale, 1991) performs the DMO correction to remove the effect of dipping reflector. If we consider

NMO/DMO correction as single procedure it will be clear that NMO/DMO stacking operator is a fan-shaped surface which is the kinematic reflection response of the ZO isochron. This fan-shape surface is also often called the MZO stack surface (Perroud et al., 1997). As shown in Figure 1.10 for a ZO sample P_0 the ZO isochron is shown by a lower half-circle centered at X_0 with radius $vt_0/2$, where t_0 is the time coordinate of point P_0. Accordingly, the travel times of the fan-shaped MZO surface can also be described by the CRP trajectories, which is shown by thin green lines in Figure 1.10, constructed for reflector points on the half-circle isochron of P_0. The MZO stack surface fits not very well to the true travel time surface of the illustrated reflection event. Only along the bold green line the operator sums up the amplitudes of the reflection event which is the CRP trajectory of R in the displayed case. The remaining part of the stack surface only adds noise to the stacked result. Thus, it deteriorates the stacking result because the noise does not always interfere destructively during the stack. However in principle the problem is more complicated, because the velocity analysis gives the wrong stacking velocities in presence of dipping reflector (too large, influenced by the dip).

1.2.3 Common-reflection-surface stack

The common-reflection-surface stack (CRS) follows the concepts of the classical stacking velocity analysis, i. e., the local parameterization and stacking of reflection events by means of an analytic second-order approximation of the reflection traveltime, and the determination of the stacking parameters by means of coherence analysis (Müller, 1999; Mann et al., 1999, Jäger et al. 2001).

The relation between conventional stacking velocity analysis and the CRS approach has, e. g., been described by Hertweck et al. (2007). To highlight the similarities between these approaches, they expressed the CRS operator in terms of horizontal slowness and two imaging velocities, one of the two latter representing the well-known stacking velocity. Equivalent formulations can be given in terms of spatial traveltime derivatives in terms of paraxial ray theory (Schleicher et al., 1993, Bortfeld, 1989; Červený, 2001) or in terms of properties of hypothetical wavefronts (Tygel et al., 1997). For the sake of consistence with related publications, I will use the latter description in the following, although traveltime derivatives will come into play as well.

To obtain the travel time formulation for a 2-D inhomogeneous model with arbitrarily curved interfaces (see Figure 1.11), Hubral (1983) proposed two hypothetical experiments which yield two different waves. One of these experiments is associated with an exploding diffractor and generates the so-called normal incidence point (NIP) wave with radius R_{NIP} at the surface, and the other experiment is associated with an exploding reflector and generates the so-called normal (N) wave with radius R_N at the surface. Both radii are defined at the emergence location of the normal ray.

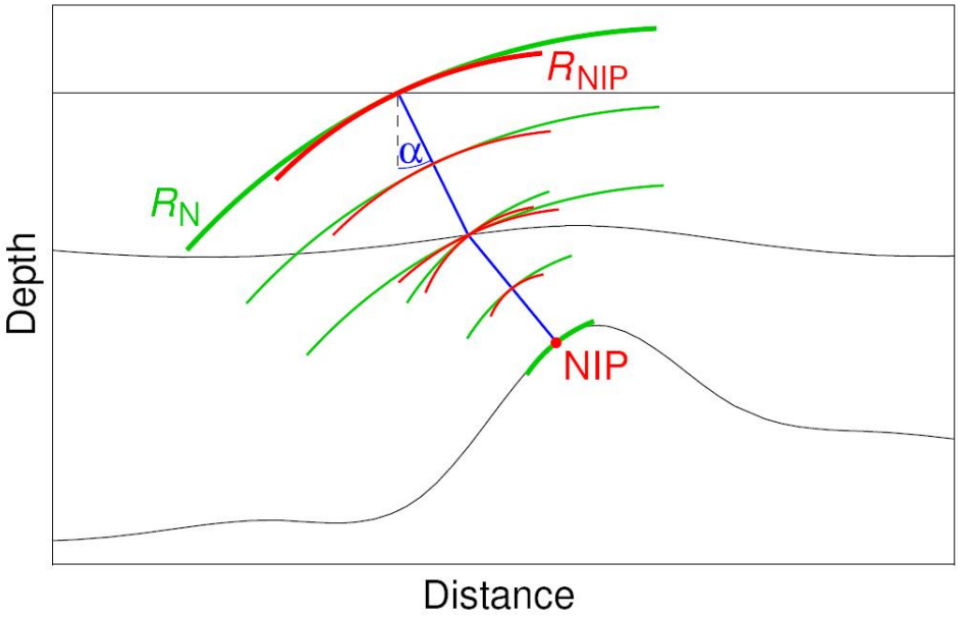

Figure 1.11: Two Hypothetical experiments: The NIP-wave produced by an exploding diffractor experiment is depicted in red. The normal wave generated by an exploding reflector experiment is depicted in green (Hertweck et al., 2007).

The curvature and the emergence angle of the wavefronts of these waves are known as the parameter of CRS stack method. In physical point of view, attribute α shows the orientation of the reflector, R_N relates to the curvature and R_{NIP} shows the location of the reflector. To simulate a ZO sample these three attribute i.e. α, R_N and R_{NIP}, the so-called kinematic wavefield attributes, have to be determined. The lower part of Figure 1.12 depicts a circular reflector segment C_R which is placed into point R. The reflector segment (shown in red) has the same curvature as the investigated reflector in point R. For all points on the reflector segment, the green CRP trajectories build up the CRS traveltime (operator) in time/midpoint/half offset

domain, i.e. (t, x_m, h), assigned to P_0. This surface (shown in green) is tangent to the true reflection response (shown in blue) along the bold green CRP trajectory of point R that has its origin at point P_0. As it is illustrated in Figure 1.12 the CRS operator fits better to the reflection event than the MZO operator.

The same concepts of CRS method are employed in similar imaging methods like Multifocusing (see, e. g., Gelchinsky et al., 1999a,b; Landa et al., 1999).

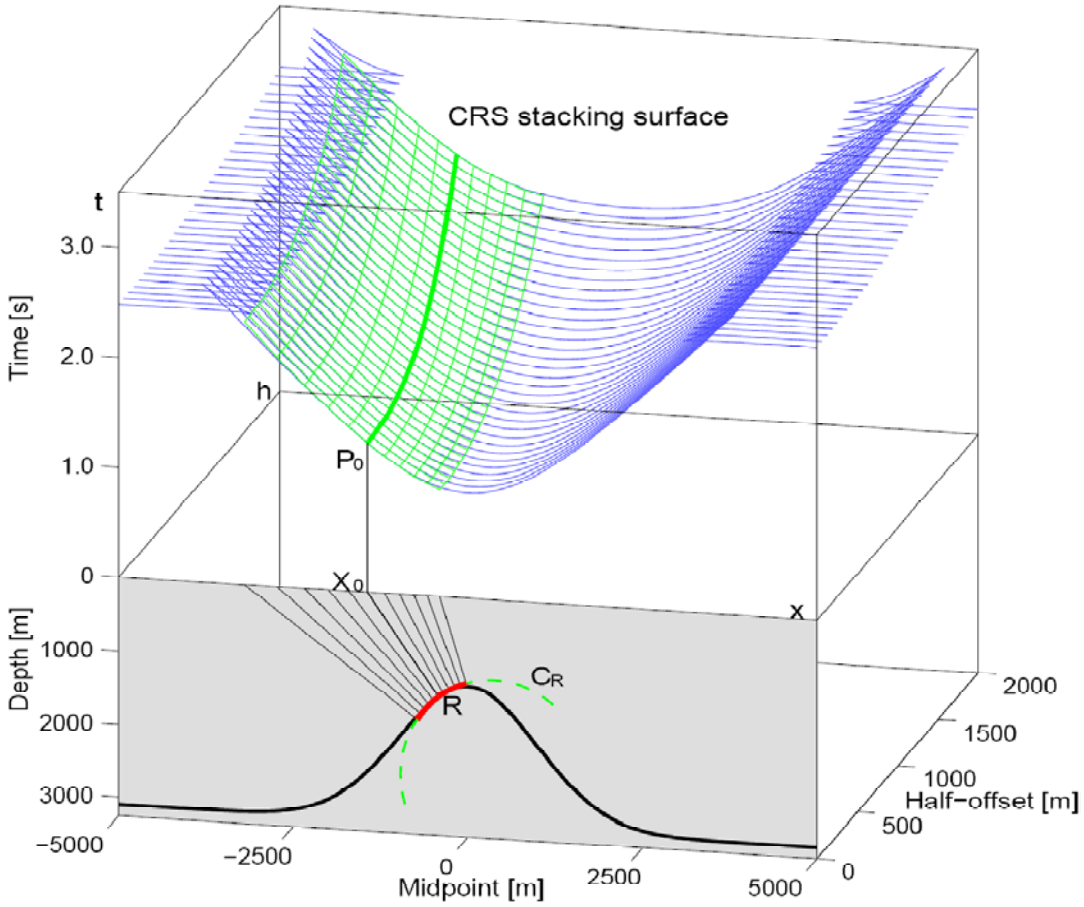

Figure 1.12: Lower half: Dome-like reflector with ZO normal-incidence rays to the reflector segment C_R at R. The orientation of the reflector segment (shown in red) is defined by the direction of the ray from X_0 to R. Upper half: True reflection response (in blue) and CRS stack surface (in green) for the reflector segment at R. Both surfaces touch each other along the CRP trajectory (in bold green) for the reflector point R (Jäger, 1999).

In its simplest implementation, the CRS stack determines only one optimum stacking operator for each zero-offset (ZO) sample to be simulated. Along this optimum operator, we obtain the maximum coherence in the seismic reflection data. If there is only one reflection event contributing to the considered sample or no coherent event

at all, this is sufficient. However, in the presence of curved reflectors, diffractors, or multiples various events might intersect each other and/or themselves, such that a single stacking operator per ZO sample is no longer sufficient to simulate a stacked section containing all relevant contributions. To account for such conflicting dip situations, Mann (2001, 2002) proposed to allow for a small, discrete number of multiple stacking operators for a particular ZO sample. The determination of additional stacking parameters associated with local coherence maxima is quite simple, but the main difficulty in this approach is to identify conflicting dip situations and to decide how many contributions should actually be considered. This implies a tricky balancing between lacking contributions and potential artifacts due to the unwanted parameterization of spurious events. Due to the discrete number of considered events, the number of detected and, thus, imaged events might change from sample to sample such that seismic events might still show up fragmented.

The introduction of inversion methods fully exploiting the information contained in the CRS stacking parameters (Duveneck, 2004a,b) enabled a consistent imaging workflow consisting of CRS stack, NIP-wave tomography, and prestack depth migration (preSDM) (see, e. g., Mann et al., 2003; Heilmann et al., 2004; Hertweck et al., 2004). In this workflow, the stacked section mainly serves as an intermediate result for automated picking rather than as a final image for interpretation. Thus, lacking contributions in the stacked section due to conflicting dip situations are acceptable and do not affect the final depth image. However, in data of complex nature and/or high noise level, generating a macro-velocity model of sufficient accuracy for prestack depth migration might not be feasible with reasonable effort. In such cases, poststack depth migration (postSDM) with its much lower requirements in terms of velocity model accuracy is more attractive and the completeness of the stacked section turns into a relevant issue again.

To obtain a stack section containing all intersecting events, Soleimani et al. (2009a,b) proposed an adapted CRS strategy by merging concepts of the DMO correction (e. g., Hale, 1991) with the CRS approach: instead of only allowing a single stacking operator or a small discrete number of stacking operators per sample, a virtually continuous range of dips is considered. To simplify this process and to further emphasize usually weak diffraction events, this has been implemented with a CRS operator reduced to (hypothetical) diffraction events. This so-called common-diffraction-surface (CDS) stack approach has been successfully applied to complex

land data (Soleimani et al., 2010). However, the approach is quite time consuming, as separate stacking operators have to be determined for each stacked sample to be simulated and each considered dip in a data-driven manner by means of coherence analysis in the prestack data. In the following, we will refer to this approach as the data-driven CDS stack.

1.3 Model-based seismic imaging methods

As mentioned above, the object of almost all seismic imaging methods is to provide a depth domain image of discontinuities of elastic properties from time domain multi-coverage data set. The subsurface reflectors have to be established by transforming the reflection events in the time domain into reflecting interfaces in depth domain. The model of elastic properties generated by inversion should be consistent with the acquired data. In spite of the fact that the final appropriate outcome of imaging is in depth domain, reflection seismic imaging also can be done in time domain as well. Time imaging provides sufficient information for a variety of subsurface models of moderate complexity. Moreover, for more complex models that request the use of prestack depth migration (PreSDM), time imaging usually constitutes a key first step, which facilitates the estimation of the elastic properties for depth imaging.

To go from the time domain to the depth domain an explicit model of the local elastic properties of the subsurface is required. The accuracy of this model has to be sufficient at least on a large scale. If this a priori model is close enough to the real situation, it is possible to achieve the true model of elastic properties just iteratively updating the priori model. This type of imaging so-called model-based method (Mann, 2002).

All common types of migration schemes can be considered as model-based approaches, including prestack time migration (PreSTM), poststack time migration (PostSTM), prestack depth migration (PreSDM) and poststack depth migration (PostSDM). Of course, PreSDM is most sensitive to model inaccuracies, where as postSTM is least sensitive (Yilmaz, 2001).

PreSDM method is a conventional method to obtain an interpretable image of the subsurface. For a Kirchhoff PreSDM, the reflector is build up by the kinematic response of diffractors according to Huygens principle. Thus, the reflected wavefronts is the envelope of all diffraction events from hypothetical diffractors

representing the reflector. The summation surface can then be regarded as a collection of Huygens traveltime curves. This is called a Kirchhoff summation (see Yilmaz, 2001).

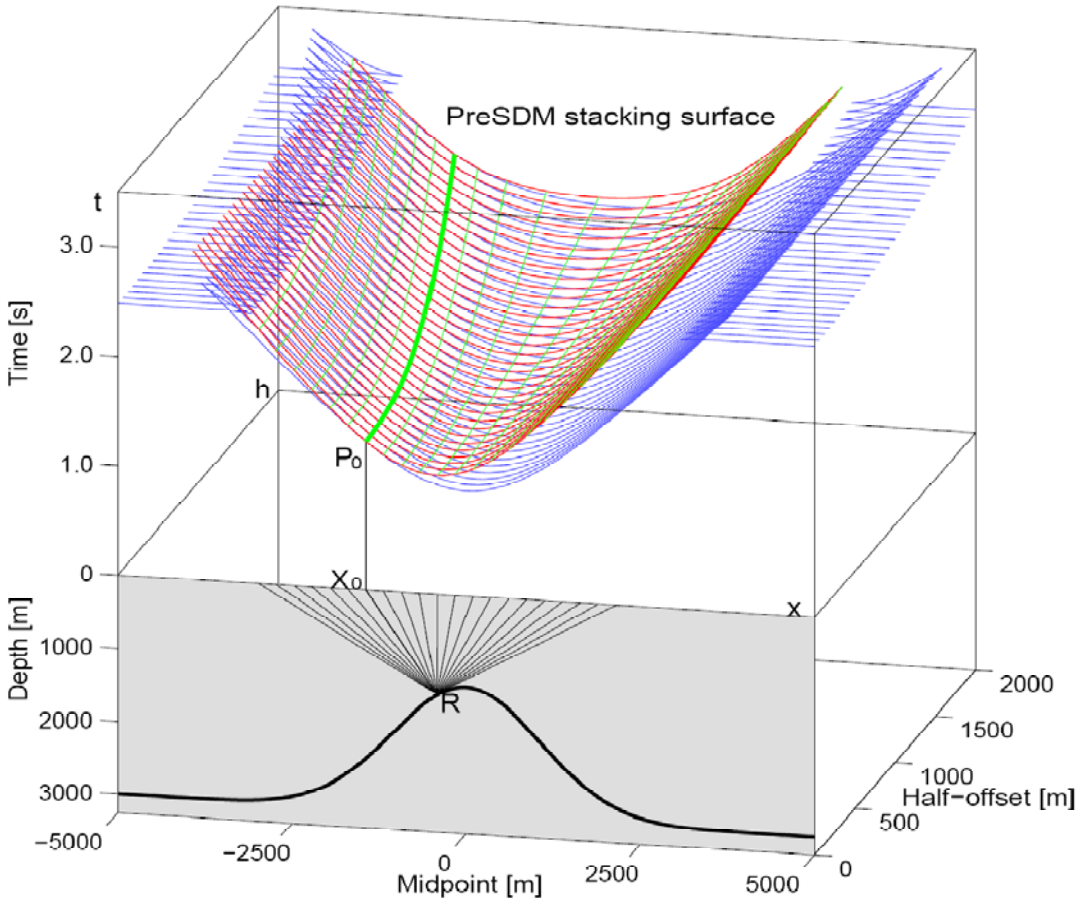

Figure 1.13: Lower half: Dome-like reflector with rays connecting various shot-receiver pairs on the seismic line to a diffraction point at R. Upper half: CO reflection-time surface (dark blue) to which the PreSDM stack surface (red) for diffraction point R is tangent along the CRP trajectory (bold green). The thin green CRP trajectories correspond to different reflector orientations at point R (Jäger, 1999).

The PreSDM operator in Figure 1.13 can be consider as the multi-coverage traveltime response of a diffraction point at R. A PreSDM stack surface can also be described by the thin green CRP trajectories related to hypothetical reflectors of different dips passing through point R (Jäger, 1999). Although the PreSDM operator in Figure 1.13 fits in large area to the reflection traveltime, a precise velocity model to build up this operator is usually not available. An initial velocity model can be obtained from CMP or NMO/DMO/stack by means of a simple 1-D Dix inversion

but these velocity models have to be updated iteratively to improve the result of the PreSDM. In some sense, the DMO correction is a model-based method (for good reason also called partial prestack migration). However in practice, it usually implicitly assumes a local homogeneity or a simple velocity gradient for the velocity model.

Mann (2002) proposed an extended search strategy to the CRS stack method to address the conflicting dip situations. Afterwards Soleimani (2009) by merging the concepts of DMO in to the CRS approach overcame to the drawback of previous methods. This so-called (data-driven) common-diffraction-surface (CDS) stack method computationally is very expensive.

In this thesis, I propose and apply a model-based approach to the CDS stack method. I assume that a smooth macro-velocity model has already been determined, e. g. by means of a processing sequence consisting of CRS stack, automated smoothing and picking, and NIP-wave tomography. Of course, a macro-velocity model generated with any other inversion approach can be used as well. In such a smooth macro model, the parameters of the CDS stacking operators can be easily forward-modeled by means of kinematic and dynamic ray tracing such that their determination by means of coherence analysis in the prestack data set is no longer required. In this way, a complete stacked section optimized for poststack depth migration can be generated in a much more efficient manner compared to the data-driven CDS approach.

1.4 Structure of the thesis

After the initial remarks in this chapter, chapter 2 contains the basic of ray theory. Mathematical concepts and formulas are presented that are relevant to the understanding of the model-based CDS stack method. Starting with the well-known elastodynamic wave equation, the high-frequency approach of ray theory is introduced, which leads to the eikonal equation. Afterwards, solutions to the previously mentioned differential equations are shown and emphasis is put not only on the kinematic parts of the solution but on the dynamic ones as well.

In chapter 3 the very basic essentials of CRS method which are required in scope of this thesis will be explained. In this chapter the conflicting dip problem, how this problem arises and the problems are caused by this issue will be discussed. Then the

idea of Mann (2002) and Soleimani (2009) to overcome to the problem of conflicting dip will be explained.

In Chapter 4, I consider the implementational aspects of the model-based common-diffraction-surface (CDS) stack method. In this chapter it has been shown how to determine the parameter of CDS operator by means of forward modeling based on ray theory instead of using of a very time consuming coherence analysis.

In Chapter 5, the synthetic data of Sigsbee 2A and a real land data set will be processed with the new introduced model-based CDS stack approach. These results are compared with the result of the extended CRS and data-based CDS stack method to examine how much the results have been improved.

In Chapter 6, I conclude the experiences and results and give an outlook.

Chapter 2

The basic ideas of ray theory

Not too long ago many exploration geophysicists believed that ray theory has little to offer in the field of seismic reflection imaging. They thought that ray theory is only useful when the seismic forward modeling problem like the construction of a synthetic seismogram for a given earth model, is considered. This circumstance has changed; several imaging algorithms based on ray theory have been developed. These algorithms can handle kinematic as well as dynamic aspects of imaging in a geometrically and physically appealing way. Although no rays exist in real nature, the ray method turned out to be able to describe real physical phenomena such as the wave propagation process in a flexible, time-saving, and accurate way (Hertweck, 2000).

The propagation of seismic body waves in complex, laterally varying 3-D layered structures is a complicated process governed by the elastodynamic wave equation. Červený (2001) divides these processes into two categories:

1. Methods based on direct solutions of the elastodynamic wave equation, e.g. numerical finite-difference or finite-element methods, and
2. Approximate high-frequency asymptotic methods.

Using a high-frequency assumption, asymptotic solutions of the elastodynamic wave equation can be found. These are the eikonal equation and transport equations. They describe the kinematic and dynamic aspects of the wavefield. Whereas the transport equations are of no further interest in this thesis, the eikonal equation will be solved yielding the so-called ray tracing system.

In this chapter, I will present the basic ideas and formulas of ray theory. Obviously, I am only able to show a summary of the most important facts because a complete description would blow up this thesis. Further details on seismic wave propagation and ray theory may be found in many books, for example in Aki and Richards (1980), Kravtsov and Orlov (1990), and especially Červený (2001).

2.1 The elastodynamic wave equation

In seismology, it is usually assumed that for small-amplitude displacements, the earth behaves as a linear elastic medium. Wave propagation in such a medium is governed by the elastodynamic equation (Aki and Richards, 1980).

Let $\mathbf{x} = (x_1,\ x_2,\ x_3)$ denote the position of a certain particle in Cartesian coordinates. The particle's displacement vector with respect to its position in the unperturbed medium at time t is given by $u(\mathbf{x}, t)$. The elastodynamic equation for an unbound anisotropic, inhomogeneous, perfectly elastic medium reads

$$(c_{ijkl}u_{k,l})_{,j} = \rho\ddot{u}_i\ , i = 1,2,3 \tag{2.1}$$

where c_{ijkl} is the elastic tensor, containing, in the most general case, 21 independent parameters and ρ is the mass density. The notation $u_{i,j}$ denotes the partial derivative $\partial u_i/\partial x_j$, and overdots are used to indicate time derivatives, as in $\ddot{u}_i = \partial^2 u_i/\partial t^2$. Both, the elastic tensor and the density may be spatially variable: $c_{ijkl} = c_{ijkl}(\mathbf{x})$ and $\rho = \rho(\mathbf{x})$. The number of independent component of the elastic tensor reduce into just two parameter (the Lamé parameters, λ and μ) in the case of isotropic media. In such situation the elastodynamic equation reads

$$\left(\lambda u_{,j,j}\right)_{,i} + \left[\mu(u_{i,j} + u_{j,i})\right]_{,j} + f_i = \rho\ddot{u}_i \tag{2.2}$$

Here f_i denote the Cartesian components of body forces (force per volume). It is well-known that in a homogeneous isotropic elastic medium two types of elastic elementary waves of vectorial character exist: the compressional, or so-called primary (P) wave and the shear, or so-called secondary (S) wave. In inhomogeneous media, the wavefield cannot generally be separated into independently traveling waves because the propagation of P- and S-waves is coupled. Thus, the solution of equation (2.2) is considerably more difficult than in a homogeneous medium (Hertweck, 2000). To make the problem of describing and interpreting wavefields measured in reflection seismology tractable, the assumption of high-frequency wave propagation is often made, which allows to construct approximate solutions to the wave equation. In order to find a high-frequency solution to (2.2) in terms of zero order ray theory, a transient time signal of the form

$$u_i(x_j, t) = U_i(x_j)F(t - T(x_j)) \tag{2.3}$$

is considered, where U_i and T are smooth functions of the Cartesian coordinate and $F(t - T(\mathbf{x}))$ represents a high-frequency analytical signal. Equation (2.3) represents a generalization of the plane-wave solution, with U_i and T varying arbitrarily (but slowly) with the spatial coordinates. Here, the point is that the Fourier spectrum of the analytical signal F is assumed to effectively vanish for small frequencies (Červený, 2001). Inserting (2.3) for u_i into (2.2) yields

$$N_i(\vec{U})\ddot{F} - M_i(\vec{U})\dot{F} + L_i(\vec{U})F = 0 \tag{2.4}$$

where

$$\begin{aligned} N_i(\vec{U}) &= -\rho U_i + (\lambda + \mu)U_j T_{,i} T_{,j} + \mu U_i T_{,j} T_{,j}\,, \\ M_i(\vec{U}) &= (\lambda + \mu)\left[U_{j,i} T_{,j} + U_{j,j} T_{,i} + U_j T_{,ji}\right] + \mu\left[2U_{i,j} T_{,j} + U_i T_{,jj}\right] + \\ &\quad + \lambda_{,i} U_j T_{,j} + \mu_{,j} U_i T_{,j} + \mu_{,j} U_j T_{,i}, \\ L_i(\vec{U}) &= (\lambda + \mu)U_{j,ij} + \mu U_{i,jj} + \lambda_{,i} U_{j,j} + \mu_{,j}(U_{i,j} + U_{j,i}) \end{aligned} \tag{2.5}$$

As equation (2.4) must be satisfied for any arbitrary frequency, each term must vanish independently. For high frequencies, the first and second term are expected to dominate over the third term, which is usually neglected. Thus, the following two equations remain

$$N_i(\vec{U}) = 0 \tag{2.6}$$

$$M_i(\vec{U}) = 0 \tag{2.7}$$

Defining the slowness vector **p** as gradient of T(**x**), i.e. $\mathbf{p} = \nabla T$ equation (2.6) reads

$$(\Gamma_{ij} - \delta_{ij})U_j = 0 \tag{2.8}$$

where

$$\Gamma_{ij} = \frac{\lambda+\mu}{\rho} p_i p_j + \frac{\mu}{\rho} p_k p_k \delta_{ij} \qquad \text{and} \qquad \delta_{ij} = \begin{cases} 1 & i = j \\ 0 & i \neq j \end{cases} \tag{2.9}$$

Equation (2.8) represents an eigenvalue problem for the matrix Γ_{ij}. It has non-trivial solutions if

$$\det\left(\Gamma_{ij} - \delta_{ij}\right) = \left(\frac{\mu}{\rho}p_k p_k - 1\right)\left(\frac{\lambda+\mu}{\rho}p_k p_k - 1\right)^2 = 0 \tag{2.10}$$

which leads to the possible solution

$$p_k p_k = \frac{\rho}{\mu} = {v_S}^{-2} \tag{2.11a}$$

$$p_k p_k = \frac{\rho}{\lambda+\mu} = {v_P}^{-2} \tag{2.11b}$$

Equations (2.11a) and (2.11b) are called *eikonal equation*. As can be seen from equations (2.11) there are two different eigenvalues. Therefore two different wave types may be distinguished which propagate independently in isotropic, smoothly inhomogeneous media in the high-frequency approximation: P-waves polarized longitudinally in the direction of the slowness vector, $\mathbf{p} = \nabla T$, and S-waves polarized transversal in the plane perpendicular to **p**. The polarization direction follows from the eigenvectors corresponding to the eigenvalues (2.11). The eikonal equations (2.11) control the kinematic characteristics of seismic wave propagation in smoothly inhomogeneous, isotropic media. From equation (2.7) the transport equations for P- and S-waves can be derived (Červený, 1972), which are of no interest in this thesis. Thus, this equation will not be further investigated.

The conditions of validity of the high-frequency solution of the wave equation are difficult to quantify. In general, it can be said that for ray theory to be valid, the involved signal wavelengths should be much smaller than the length scale of medium heterogeneities. A number of conditions for the validity of ray theory have been given by Ben-Menahem and Beydoun (1985a,b), Popov and Oliveira(1997), and Červený (2001).

2.2 Ray tracing systems in inhomogeneous isotropic media

Rays play a basic role in various branches of physics. For this reason, it is not surprising that many different approaches can be used to define them and to derive ray tracing systems. The most general approach to derive seismic ray tracing systems is based on the asymptotic high-frequency solution of the elastodynamic equation.

This approach yields a very important result, namely that the high-frequency seismic wave field *in a smoothly inhomogeneous isotropic medium* is approximately separated into two independent waves: the P and the S wave. The traveltime fields of these two independent waves satisfy the respective eikonal equations. The eikonal equation is a nonlinear partial differential equation of the first order. In mathematics, such equations are usually solved for *T* in terms of characteristics (e. g. Herzberger, 1958; Bleistein, 1984). The characteristics of the eikonal equation are trajectories in the six dimensional (x, y, z, p_x, p_y, p_z,) , described by a system of six ordinary differential equations in 3-D, usually called (kinematic) ray tracing system, which can be easily solved by means of standard numerical procedures. The main advantage of this formalism is that the traveltime along such a trajectory can be obtained by a simple integration.

2.2.1 Rays as characteristics of eikonal equation

Since the following derivations are equally valid for both wave types the more general quantity *V* is introduced to denote either the P-wave or the S-wave velocity. The eikonal equation for body waves propagating in smoothly inhomogeneous isotropic media was derived in Section 2.1. In Cartesian coordinates, it reads

$$p_i p_i = 1/V^2(\mathbf{x}), \qquad \text{where} \qquad p_i = \partial T/x_i \tag{2.12}$$

Here T=T(**x**) is traveltime, p_i are components of slowness vector, and **p**=∇T. This equation is a nonlinear partial differential equation of the first order for T(**x**) (Červený, 2001). It is possible to write the general form of eikonal equation in the following form:

$$\mathcal{H}(x_i, p_i) = 0 \tag{2.13}$$

here $\mathcal{H}$ is the Hamiltonian which can be express in different ways. For example $\mathcal{H}(x_i, p_i) = p_i p_i - V^{-2}$, $\mathcal{H}(x_i, p_i) = \frac{1}{2}(V^2 p_i p_i - 1)$, or $\mathcal{H}(x_i, p_i) = (p_i p_i)^{1/2} - 1/V$

The nonlinear partial differential equation (2.13) is usually solved in terms of the above mentioned *characteristics* along which (2.13) is satisfied. With *u* as parameter along this trajectory, the characteristic system of the nonlinear partial differential equation (2.13) reads

$$\frac{dx_i}{du} = \frac{\partial \mathcal{H}}{\partial p_i}, \qquad \frac{dp_i}{du} = -\frac{\partial \mathcal{H}}{\partial x_i}, \qquad \frac{dT}{du} = p_k \frac{\partial \mathcal{H}}{\partial p_k} \tag{2.14}$$

Bleistein (1984) offers a very detailed and tutorial treatment for derivation of the characteristic system. In a 3-D medium, the system consists of seven equations. The six equations for $x_i(u)$ and $p_i(u)$ are, in general, coupled and must be solved together. The solution to these six equations is $x_i = x_i(u)$, the characteristic curve as a 3-D trajectory, and $p_i = p_i(u)$, the components of the slowness vector along the characteristic. The seventh equation for the travel time along the trajectory, $T = T(u)$, is not coupled with the other six equations and can be solved independently, as soon as the characteristic is known. Since the rays have been defined as characteristic curves of the eikonal equation, the system of equations (2.14) can be used to determine the ray trajectory and the travel time along it. It is called the *system of ray equations*, or the *ray tracing system* (Červený, 2001).

Now I will express a rather general form of Hamiltonian, which includes many other forms:

$$\mathcal{H}(x_i, p_i) = n^{-1}\left[(p_i p_i)^{n/2} - 1/V^n\right] \tag{2.15}$$

where n is real number. Using L'Hôpital's rule for (2.15) for $n \to 0$ yields the Hamiltonian

$$\mathcal{H}(x_i, p_i) = \frac{1}{2}\ln(p_i p_i) + \ln V = \frac{1}{2}\ln(V^2 p_i p_i) \tag{2.16}$$

The factor *n* in (2.15) is used to obtain a suitable parameter *u* along the characteristic. The characteristic system of equations (2.14) corresponding to Hamiltonian (2.16) reads

$$\frac{dx_i}{du} = (p_k p_k)^{(n/2)-1} p_i, \quad \frac{dp_i}{du} = \frac{1}{n}\frac{\partial}{\partial x_i}\left(\frac{1}{V^n}\right), \quad \frac{dT}{du} = (p_k p_k)^{n/2} = V^{-n} \tag{2.17}$$

It is possible to write down several forms of ray tracing system for different *n* and, thus, for different parameters *u* along the ray (Červený, 2001). Since the desired parameter along the ray trajectory, which is considered in this thesis, is traveltime we

choose $n=0$ in (2.17), then $dT/du = 1$ and the parameter u is directly equivalent to traveltime. The ray tracing system then reduce to six coupled equations

$$\frac{dx_i}{dT} = (p_k p_k)^{-1} p_i \,, \qquad \frac{dp_i}{dT} = -\frac{\partial \ln V}{\partial x_i} \tag{2.18}$$

Inserting $p_k p_k = V^{-2}$ into (2.18) yields

$$\frac{dx_i}{dT} = V^2 p_i \,, \qquad \frac{dp_i}{dT} = -\frac{\partial \ln V}{\partial x_i} \tag{2.19}$$

The six coupled equations of (2.19) describe the ray path in a six-dimensional phase space with coordinates (x, y, z, p_x, p_y, p_z). To achieve dynamic information like second derivative of traveltime fields, which is of interested in this thesis, we have to perform dynamic ray tracing along ray path knowing from (2.19).

2.3 Dynamic ray tracing

Dynamic ray tracing is a powerful approach which nowadays has been frequently applied to evaluate high-frequency seismic wavefields in laterally inhomogeneous layered structures and in the solution of inverse seismic problems (e. g. Duveneck, 2004c; Klüver, 2007). It involves solving a system of ordinary differential equations along a ray Ω which the characteristic or phase space trajectory (position, slowness vector components) along ray Ω has been determined by kinematic ray tracing in advance. Many forms and various coordinate systems can be use to express the dynamic ray tracing system. The simplest form of the dynamic ray tracing system in isotropic media is obtained in ray-centered coordinates connected with ray Ω (Červený, 2001). Therefore, the derivations are limited to this coordinate system throughout this section. The eikonal equation in ray-entered coordinates will be used to derive a simple system of linear ordinary differential equations of the first order known as the paraxial ray tracing system. Such rays are called the paraxial rays, and the relevant system is called the paraxial ray tracing system (see Červený at al., 1984; Beydoun and Keho, 1987). The term *paraxial* has his roots in optics were it represents the vicinity of the axis of the optical system. In our case it denotes the vicinity of so-called central ray. The dynamic ray tracing system can be immediately

obtained from the paraxial ray tracing system. Both systems are closely connected: their system matrices are identical, only the computed quantities have a different physical meaning. Solving the dynamic ray tracing system for two sets of mutually orthogonal initial conditions yields the ray propagator matrix **Π**, which describe the second derivative of the traveltime wave fields in a very convenient way. In addition, the dynamic ray tracing system provides dynamic information which is very useful, e. g., to calculate the geometrical spreading for true amplitude imaging (Červený and Hron, 1980; Hubral et al., 1995).

2.3.1 Ray-Centered Coordinates

As mentioned above, the simplest form of dynamic ray tracing is obtained in ray-centered coordinattes q_1, q_2 and q_3. The ray-centered coordinate system is a curvilinear orthogonal coordinate system introduced in such a way that the ray Ω itself represents the q_3-axis of the system. Two other axis q_1 and q_2 are formed by two mutually perpendicular lines intersecting at the ray Ω, situated in a plane perpendicular to the ray Ω at q_3, Thus, the coordinate plane $q_3 = const.$, is tangent to the wavefront and the ray Ω is specified by equations $q_1 = q_2 = 0$.

The vector basis of the ray-centered coordinate system connected with Ω is formed at an arbitrary point corresponding to the arclength $q_3 = s$ of ray Ω by a right-handed triplet of unit vectors $\vec{e}_1$, $\vec{e}_2$ and $\vec{e}_3$ where $\vec{e}_3(s) = \vec{t}(s)$ is the unit tangent to ray Ω. Vectors $\vec{e}_1$, $\vec{e}_2$ are situated in plane $\Sigma^{\perp}$, perpendicular to Ω at a given q_3 and mutually perpendicular, see Figure (2.1). The orientation of unit vectors $\vec{e}_1$, $\vec{e}_2$ along the ray is described by the following differential equations

$$d\vec{e}_I/ds = (e_I.\nabla V)\mathbf{p}, \quad I = 1,2 \tag{2.20}$$

Here **p** is the slowness vector, known from the kinematic ray tracing, see equation (2.19). A point Ŕ outside the ray trajectory is described in ray-centered coordinates as follows:

$$\vec{r}(q_1, q_2, s) = q_1\vec{e}_1(s) + q_2\vec{e}_2(s) + \vec{r}(0, 0, s) \tag{2.21}$$

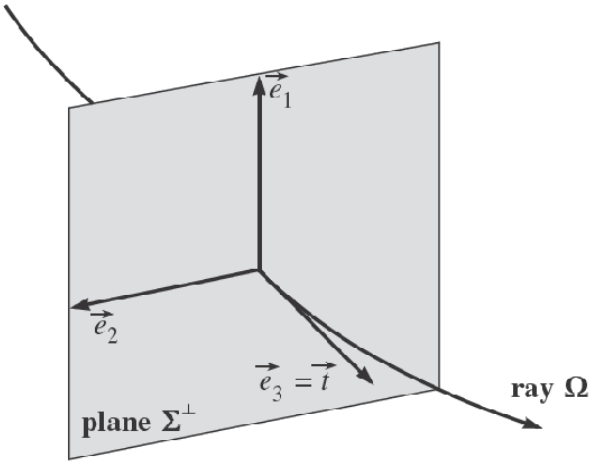

Figure 2.1: Basis vectors $\vec{e}_1$, $\vec{e}_2$, and $\vec{e}_3$ of the ray-centered coordinate system q_I connected with ray Ω. Ray Ω is the q_3-axis of the system. At any point on the ray (q_3 fixed), unit vector $\vec{e}_3 = t$ (the unit tangent to Ω). Unit vectors, $\vec{e}_1$, and $\vec{e}_2$ are situated in the plane $\Sigma^\perp$, perpendicular to Ω at a given q_3, and are mutually perpendicular. The triplet, $\vec{e}_1$, $\vec{e}_2$, $\vec{e}_3$ is right-handed (Červený, 2001).

Keeping the arclength s fixed, only points in the plane perpendicular to the ray can be described. In order to describe points outside of this plane in ray-centered coordinates one has to move along the ray to change the origin of the ray-centered coordinate system. A sketch of the situation described here is given in Figure 2.2.

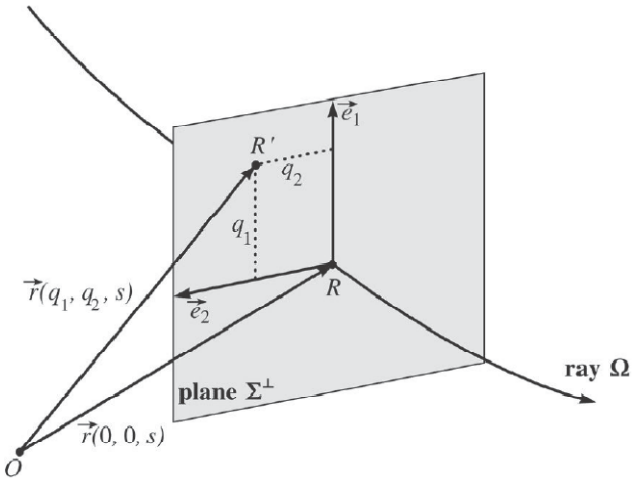

Figure 2.2: Ray-centered coordinates q_1, q_2, and q_3 of point $\acute{R}$ situated in the vicinity of ray Ω. Point $\acute{R}$ is situated in plane $\Sigma^\perp$ perpendicular to Ω and crossing Ω at point R. The position of point R determines $q_3(\acute{R})$ because $q_3(\acute{R}) = q_3(R)$. Then, $q_1(\acute{R})$ and $q_2(\acute{R})$ are determined as Cartesian coordinates of $\acute{R}$ in plane $\Sigma^\perp$, with basis vectors $\vec{e}_1$, $\vec{e}_2$ (Červený, 2001).

The coordinates $\vec{r}(q_1, q_2, s)$ of a point in the vicinity of a ray are uniquely defined if there is only one plane perpendicular to the ray which contains that point. If several such planes can be constructed the point is no longer uniquely defined. The validity of the ray-centered coordinate system is restricted to that range around the ray, in which points may be uniquely described. Obviously, this range of validity depends on the curvature of the ray and, thus, the model complexity (Červený, 2001).

Using $\vec{t}(s) = d\vec{r}(0, 0, s)/ds$, an infinitesimal line segment dS is given by the relation

$$dS^2 = d\vec{r}.d\vec{r} = dq_1{}^2 + dq_2{}^2 + h^2 ds^2 \tag{2.22}$$

where h is a scale factor and reads

$$h = 1 + (V^{-1}\,\partial V/\partial q_I)_{q_1=q_2=0} q_I \tag{2.23}$$

2.3.2 Paraxial Ray tracing in ray-centered coordinates

Paraxial ray can be described by a second order approximation of the eikonal equation around the central ray. The eikonal equation $(\nabla T)^2 = V^{-2}$ in ray-centered coordinates for the 3-D case reads (see, e. g., Červený, 2001)

$$\left(\frac{\partial T}{\partial q_1}\right)^2 + \left(\frac{\partial T}{\partial q_2}\right)^2 + \frac{1}{h^2}\left(\frac{\partial T}{\partial q_3}\right)^2 = \frac{1}{V^2(q_1,q_2,q_3)} \tag{2.24}$$

we denote

$$p_1^{(q)} = \partial T/\partial q_1\,,\; p_2^{(q)} = \partial T/\partial q_2\,,\; p_3^{(q)} = \partial T/\partial q_3 \tag{2.25}$$

The Hamiltonian can be written as

$$\mathcal{H}^R = -h\left[V^{-2}(q_i) - p_1{}^{(q)2} - p_2{}^{(q)2}\right]^{1/2} \tag{2.26}$$

From (2.26) the paraxial ray tracing system in ray-centered coordinates finally reads (Červený, 2001)

$$dq_I/ds = vp_I^{(q)},\ dp_I^{(q)}/ds = -v^{-2}v_{,IJ}q_J \tag{2.27}$$

In equation (2.27) the monotonic parameter along the ray Ω is arclength *s*. By taking into account $ds = vdT$ equation (2.27) reformulated as following

$$dq_I/dT = v^2 p_I^{(q)},\ dp_I^{(q)}/dT = -v^{-1}v_{,IJ}q_J \tag{2.28}$$

$v_{,IJ}$ is second derivative of velocity with respect to q_I which physically means the second derivatives of velocity in a plane perpendicular to the ray Ω and obtain by following equation

$$v_{,IJ} = \left(\partial^2 V(q_1, q_2, s)/\partial q_I \partial q_J\right)_{q_1=q_2=0} \tag{2.29}$$

It is possible to express the paraxial ray tracing system (2.28) in a more compact form. We define **W** matrix as following

$$\mathbf{W}(\mathrm{T}) = \left(\mathrm{q}_1, \mathrm{q}_2, \mathrm{p}_1^{(\mathrm{q})}, \mathrm{p}_2^{(\mathrm{q})}\right)^{\mathrm{T}} \tag{2.30}$$

and express (2.29) as

$$d\mathbf{W}(T)/dT = \mathbf{SW} \tag{2.31}$$

where **S** is 4 × 4 matrix which reads as

$$\mathbf{S} = \begin{bmatrix} \mathbf{0} & v^2\mathbf{I} \\ -v^{-1}\mathbf{V} & \mathbf{0} \end{bmatrix} \tag{2.32}$$

Here **0** is 2 × 2 null matrix, **I** is a 2 × 2 identity matrix, and **V** is the 2 × 2 matrix given by (2.29).

2.3.3 Dynamic ray tracing in ray-centered coordinates

Dynamic ray tracing determines the first partial derivatives of the phase space coordinates q_I and p_I along a known ray Ω with respect to its initial parameters. All

paraxial rays in its vicinity belonging to the same wavefront can be uniquely described by two parameters in the general 3-D case. For the case of a point source these may, for example, be the two take-off angles so-called ray-parameters γ_1 and γ_2, in a spherical polar coordinate system fixed at the central ray's starting point, see Figure (2.3). Due to the fact that the partial derivative $\partial/\partial\gamma$ commutes with d/ds we easily obtain from the paraxial ray tracing system (2.27) the dynamic ray tracing system

$$\frac{d}{ds}\left(\frac{\partial q_I}{\partial \gamma}\right) = v\,\frac{\partial p_I}{\partial \gamma}\,, \quad \frac{d}{ds}\left(\frac{\partial p_I}{\partial \gamma}\right) = -v^{-2}\,\frac{\partial v}{\partial q_I \partial q_J}\frac{\partial q_I}{\partial \gamma} \tag{2.33}$$

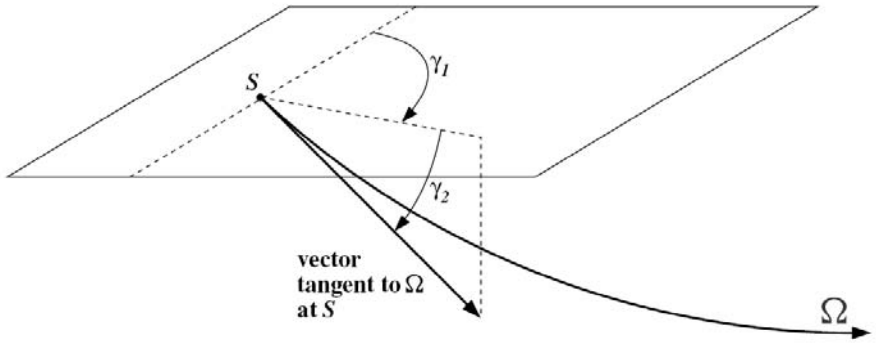

Figure 2.3: Definition of ray coordinates: for a wavefront emanating from a point source at $\boldsymbol{S}$, an arbitrary ray of the associated ray field can by specified by the two ray parameters γ_1 and γ_2, defined, e. g., as the two take-off angles in $\boldsymbol{S}$. The traveltime, arclength, or any other parameter varying monotonically along the ray Ω can be chosen for γ_3. Figure modified from Koglin (2005).

By introducing two transformation matrices **Q** and **P** as follows

$$Q_{ij} = \left(\frac{\partial q_i}{\partial \gamma_j}\right)_{q_1=q_2=0}, \quad P_{ij} = \left(\frac{\partial p_i}{\partial \gamma_j}\right)_{q_1=q_2=0} \tag{2.34}$$

the dynamic ray tracing system (2.33) then can be written as

$$d\mathbf{Q}/ds = v\mathbf{P}, \quad d\mathbf{P}/ds = -v^{-2}\mathbf{V}\mathbf{Q} \tag{2.35}$$

Like the paraxial ray tracing system (2.28), it is possible to use time *T* as monotonic parameter along the ray Ω instead of arclength *s*. The dynamic ray tracing system then reads

$$d\mathbf{Q}/dT = v^2\mathbf{P}, \quad d\mathbf{P}/dT = -v^{-1}\mathbf{V}\mathbf{Q} \tag{2.36}$$

The more compact form of dynamic ray tracing is

$$d\mathbf{X}/dT = \mathbf{SX}, \quad \text{where } \mathbf{X} = \begin{pmatrix} \mathbf{Q} \\ \mathbf{P} \end{pmatrix} \tag{2.37}$$

Here the definition of **S** and **V** is the same as in paraxial ray tracing system. Equation (2.35) or (2.36) represents one of the important forms of dynamic ray tracing system first introduced by Popov and Pšenčík (1978). Hereafter I will consider equation (2.36) as dynamic ray tracing system.

Once the dynamic ray tracing system has been solved along the central ray many other important quantities may also be computed by using the matrices **Q** and **P**. Some of these quantities which are considered in this thesis are: the matrix **M** of the second derivatives of the travel-time fields with respect to q_I, the matrix of the curvature of wavefront **K** and the matrix of radii of the curvature of wavefront **R**. The element of matrix **M** is define as following

$$M_{IJ} = \left(\partial^2 T/\partial q_I \partial q_J\right)_{q_1=q_2=0} \tag{2.38}$$

As $\partial^2 T/\partial q_I \partial q_J = (\partial^2 T/\partial q_I \partial \gamma_K)(\partial \gamma_K/\partial q_J)$, we obtain

$$\mathbf{M} = \mathbf{P}\mathbf{Q}^{-1} \tag{2.39}$$

The relation between the matrix of curvature of the wave front **K** and the matrix of the second derivatives of traveltime field **M** reads

$$\mathbf{K} = v\mathbf{M} \tag{2.40}$$

Finally, the relation between the matrix of radii of the curvature of the wavefront **R** and the matrix of second derivatives of traveltime field **M** reads

$$\mathbf{R} = \mathbf{K}^{-1} \tag{2.41}$$

It has to be emphasized that the role of **M** is considerably greater than **K** or **R** in seismic ray theory (V. Červený, personal communication, October 26, 2010).

2.3.4 Transformation from ray-centered to Cartesian coordinates

The transformation relations form ray-centered coordinate system $q_1, q_2, q_3 = t$ to the general Cartesian coordinate system x_1, x_2, x_3 are given as follows:

$$dx_k = H_{kj} dq_j \quad \text{or} \quad d\hat{\mathbf{x}} = \hat{\mathbf{H}} d\hat{\mathbf{q}} \tag{2.42}$$

where $\hat{\mathbf{H}}$ is a so-called transformation matrix. Using the basis vectors $\vec{e}_1$ and $\vec{e}_2$, we can construct the 3×3 transformation matrix $\hat{\mathbf{H}}$ from the ray-centered coordinate system $q_1,\ q_2,\ q_3$ to the general Cartesian coordinate system x_1, x_2, x_3 at any point of the ray. The first column of the transformation matrix $\hat{\mathbf{H}}$ represents Cartesian components of basis vector $\vec{e}_1$, the second column the Cartesian components of the basis vector $\vec{e}_2$, and the third column the Cartesian components of the basis vector $\vec{e}_3 = t$, the unit vector tangent to the ray. The vector t is known from kinematic ray tracing, see equation (2.19), and does not need to be computed again. If we denote the k[th] Cartesian component of the unit basis vector $\vec{e}_1$ by $\vec{e}_{k1}$ and similarly the k[th] Cartesian component of the unit basis vector $\vec{e}_2$ by $\vec{e}_{k2}$, we have

$$H_{kj} = e_{kj}\,, \quad j = 1,2\,; k = 1,2,3 \tag{2.43}$$

The basis unit vectors $\vec{e}_1$, $\vec{e}_2$, and $\vec{e}_3 = t$ form a right-handed triplet of unit vectors at any point of the ray Ω. Consequently, there is no need to compute the unit basis vector $\vec{e}_2$ ($\vec{e}_1$) using the ordinary differential equation along the ray as it can be computed from known $\vec{e}_1$ ($\vec{e}_2$) and *t*, see Červený and Pšenčík (1979).

Using the 3×3 transformation matrix $\widehat{\mathbf{H}}$, we can compute the second derivatives of velocity in ray centered coordinates from the second derivatives of velocity in Cartesian coordinates, using the following equation

$$V_{,ij} = H_{ki}{}^{T} [\partial V / \partial x_k \partial x_l] H_{lj} \tag{2.44}$$

Finally, knowing the second derivatives of the velocity in ray-centered coordinates from the second derivatives of velocity in Cartesian coordinates we can perform dynamic ray tracing.

2.3.5 The ray propagator matrix

As the system of dynamic ray tracing is linear, its general solution may be written in terms of a fundamental matrix. In this case, we can introduce the 4×4 integral matrix $\mathbf{\Pi}(T,\ T_0)$ so-called propagator matrix, which satisfies the condition $\mathbf{\Pi}(T_0,\ T_0) = \mathbf{I}$, the 4×4 identity matrix, and solves

$$\mathrm{d}\mathbf{\Pi}/\mathrm{d}T = \mathbf{S}\mathbf{\Pi} \tag{2.45}$$

If we consider two point S and R situated on ray Ω with travel time T_0 and T it is possible to introduce following notation

$$\mathbf{\Pi}(R,S) = \begin{pmatrix} \mathbf{Q}_1(R,S) & \mathbf{Q}_2(R,S) \\ \mathbf{P}_1(R,S) & \mathbf{P}_2(R,S) \end{pmatrix} \tag{2.46}$$

Where $\mathbf{Q}_1, \mathbf{Q}_2, \mathbf{P}_1$ and $\mathbf{P}_2$ are 2×2 matrixes. The propagator matrix (2.46) is obtained by solving the dynamic ray tracing system twice for two orthogonal initial conditions. $\mathbf{Q}_1$ and $\mathbf{P}_1$ are solution of dynamic ray tracing system for initial conditions

$$\mathbf{Q}(S) = \mathbf{I}, \quad \mathbf{P}(S) = \mathbf{0} \tag{2.47}$$

where $\mathbf{I}$ is a 2×2 identity matrix and $\mathbf{0}$ is a 2×2 null matrix. This initial condition is known in case of ray center coordinates as normalized plane wavefront (Červený, 2001). For such an initial condition, matrix $\mathbf{M}$ is equal to $\mathbf{0}$. Therefore the wave front at $\boldsymbol{S}$ is locally planar and the initial slowness vectors are parallel in the vicinity of $\boldsymbol{S}$ see Figure 2.4(a). In contrast, $\mathbf{Q}_2$ and $\mathbf{P}_2$ are solution of dynamic ray tracing system for initial conditions

$$\mathbf{Q}(S) = \mathbf{0}, \quad \mathbf{P}(S) = \mathbf{I} \tag{2.48}$$

This initial condition represent the so-called normalized point source (Červený, 2001). Matrix $\mathbf{M}$ of the second derivatives of the traveltime field is infinite at the initial point $\mathbf{S}$ because $\mathbf{Q}(\mathrm{S}) = \mathbf{0}$, See Figure 2.4(b).

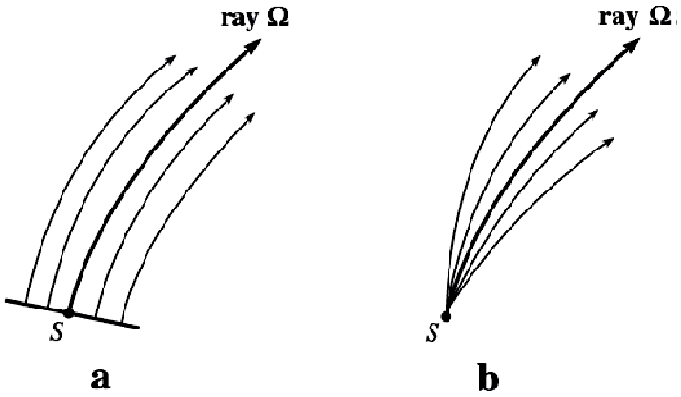

Figure 2.4: Definition of two orthogonal initial conditions for dynamic ray tracing along the ray Ω from *S*; (a) plane wave as initial condition (b) point source as initial condition (Červený, 2001).

A similar formulation of (2.46) in the global Cartesian coordinate system, the so-called surface-to-surface ray propagator matrix **T** was presented by Bortfeld (1989). The mutual relationship between **T** and **Π** was discussed by Hubral et al. (1992). Some useful properties of these matrices, namely their symplecticity, the so-called chain rule, and their corresponding back propagator matrices, are given in Červený (2001).

2.3.6 Backward propagator matrix

In certain applications, especially when the desired direction of dynamic ray tracing is opposite to the direction of kinematic ray tracing, it is useful to compute the back propagation matrix (from *R* to *S*) from the forward propagator matrix (from *S* to *R*). In the backward propagation, we must consider an orientation of the slowness vector opposite to that in the forward propagation (Červený, 2001).

The simple relation between the forward propagator matrix $\mathbf{\Pi}(R, S)$ and the backward propagator matrix $\mathbf{\Pi}^{b}(S, R)$ reads

$$\mathbf{\Pi}^{b}(S,R)= \begin{pmatrix} \mathbf{Q}_1^b(S,R) & \mathbf{Q}_2^b(S,R) \\ \mathbf{P}_1^b(S,R) & \mathbf{P}_2^b(S,R) \end{pmatrix} = \begin{pmatrix} \bar{\mathbf{Q}}_1(S,R) & -\bar{\mathbf{Q}}_2(S,R) \\ -\bar{\mathbf{P}}_1(S,R) & \bar{\mathbf{P}}_2(S,R) \end{pmatrix} = \begin{pmatrix} \bar{\mathbf{P}}_2{}^T(R,S) & \bar{\mathbf{Q}}_2{}^T(R,S) \\ \bar{\mathbf{P}}_1{}^T(R,S) & \bar{\mathbf{Q}}_1{}^T(R,S) \end{pmatrix} \tag{2.49}$$

Here, $\bar{\mathbf{Q}}_{\mathrm{I}}$ and $\mathbf{Q}_{\mathrm{I}}$ are the same; only their off-diagonal terms have opposite signs. The relations between $\bar{\mathbf{P}}_{\mathrm{I}}$ and $\mathbf{P}_{\mathrm{I}}$ are the same.

2.3.7 2-D dynamic ray tracing

In 2-D dynamic ray tracing, as considered in this thesis, the wave propagation is confined to a plane. Without loss of generality, I choose the plane defined by $x_2 = 0$. Thus, ray trajectories may be described by two spatial coordinates. Consequently, only two ray-centered coordinates remain: arclength s measured along the ray Ω and q measured perpendicular to the ray in the wave propagation plane, see Figure 2.5.

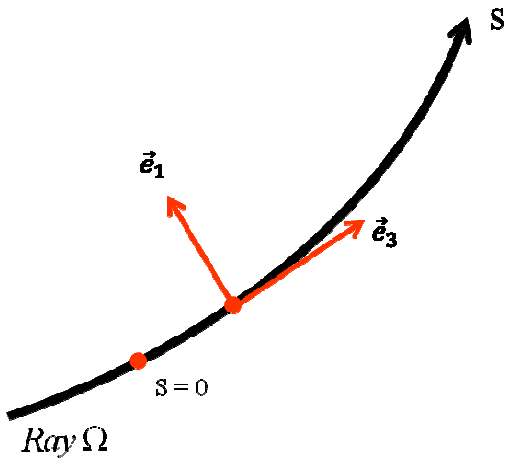

Figure 2.5: In the 2-D case, the coordinate *s* measures the arclength along the ray from an arbitrary reference point, q represent a length coordinate in the direction perpendicular to Ω at *s*. The basis of the coordinate system is formed by two unit vector $\vec{e}_1$ and $\vec{e}_3$, where $\vec{e}_1$ is the unit normal and $\vec{e}_3 = \vec{t}$ the unit tangent to the ray Ω (in the 2-D case, $\vec{e}_2 = 0$). Figure modified from Červený (1981a).

Thus, all derivatives reduce to scalar quantities in 2-D case. The dynamic ray tracing in such situation reads

$$dq/dT = v^2 p, \quad dp/dT = -v^{-1} V_{,11} q \tag{2.50}$$

Where $V_{,11}$ with the respect to Equation (2.29) is $\partial^2 V/\partial q^2$. Note that the parameter q, appears in Equation (2.50) is related to transformation matrix **Q** which become scalar in 2-D space, while the parameter q which appears in $\partial^2 V/\partial q^2$ relates to the coordinate normal to the ray. To avoid misunderstanding I will refer to the later one by *n* in chapter 4. In addition the parameter p, appears in Equation (2.50) is relate to

transformation matrix **P** which become scalar and should not confuse with slowness vector.

The more convenient matrix form reads

$$\frac{d\mathbf{X}}{ds} = \mathbf{C}\mathbf{X} \tag{2.51}$$

where **X** is a column vector and **C** is a square 2×2 matrix,

$$\mathbf{X} = \begin{bmatrix} \mathrm{q} \\ \mathrm{p} \end{bmatrix}, \quad \mathbf{C} = \begin{bmatrix} 0 & v^2 \\ -\frac{1}{v}\mathrm{v}_{,11} & 0 \end{bmatrix} \tag{2.52}$$

the 2×2 ray propagator matrix associate with system (2.50) is denoted by

$$\mathbf{\Pi}(R,S) = \begin{pmatrix} \mathrm{q}_1(R,S) & \mathrm{q}_2(R,S) \\ \mathrm{p}_1(R,S) & \mathrm{p}_2(R,S) \end{pmatrix} \tag{2.53}$$

where $(\mathrm{q}_1,\ \mathrm{p}_1)^{\mathrm{T}}$ is the solution of (2.50) for the initial condition $(1,\ 0)^{\mathrm{T}}$, known as initial normalized plane-wave condition in the case of ray-centered coordinates, and $(\mathrm{q}_2,\ \mathrm{p}_2)^{\mathrm{T}}$is a solution for the initial normalized point source condition $(0,\ 1)^{\mathrm{T}}$. The back propagator matrix in the 2-D case with respect to (2.49) reads

$$\mathbf{\Pi}^{\mathrm{b}}(S,R) = \begin{pmatrix} \mathrm{p}_2(R,S) & \mathrm{q}_2(R,S) \\ \mathrm{p}_1(R,S) & \mathrm{q}_1(R,S) \end{pmatrix} \tag{2.54}$$

The second derivative of traveltime for the initial condition of a point source is of special importance in this thesis: for forward propagation it reads

$$\mathbf{M}(R,S) = \mathrm{p}_2(R,S)/\mathrm{q}_2(R,S) \tag{2.55}$$

and for backward propagation

$$\mathbf{M}^{\mathrm{b}}(S,R) = \mathrm{q}_1(R,S)/\mathrm{q}_2(R,S) \tag{2.56}$$

In the 3-D case the kinematic ray tracing system (2.19) consists of six nonlinear partial differential equations and the dynamic ray tracing system consists of eight linear ordinary differential equations (Popov et al., 1978). Therefore, to calculate the back propagation matrix (2.49), twenty two differential equations have to be solved simultaneously. In the 2-D case the number of equation reduce to four and two in kinematic ray tracing and dynamic ray tracing, respectively. Consequently, for the calculation of the back propagation matrix (2.54), just eight differential equations are needed to be solved. For more details I refer to Červený (1981a, b, and c).

Chapter 3

Common-Reflection-Surface stack and the conflicting dip problem

Stacking approaches like the frequently applied NMO/DMO/stack chain make a central part of the seismic processing workflow. The principle of all these processes is based on the use of the redundancy of multi-coverage data set to determine so-called stacking parameters which allow correcting for the effects of measurement geometry in prestack data. A simulated zero-offset (ZO) section with a higher signal-to-noise ratio can be created by summing up these moveout corrected traces which gives the first image of the subsurface and can be used as an input for subsequent time or depth migration. Conventional stacking methods, e.g. the common-midpoint (CMP) stack, provide only a single stacking parameter. This parameter, the so-called stacking velocity, is interpreted as an integral velocity of the overburden of the reflection point. Afterwards, stacking velocities for selected locations are determined then interpolated to build a velocity model of subsurface structures.

During the last decade, the common-reflection-surface (CRS) stack method has been extensively discussed in various publications as a powerful alternative to the conventional stacking procedures. The CRS method follows the concepts of classical stacking velocity analysis i.e., the local parameterization and stacking of reflection events by means of an analytic second-order approximation of the reflection traveltime, and the determination of the stacking parameters by means of coherence analysis (see, e.g., Mann et al., 1999; Jäger et al., 2001). Conventional stacking velocity analysis is applied within individual CMP gathers with the stacking velocity as the only stacking parameter and often on a relatively coarse grid, only. In contrast, the CRS approach is applied on a fine grid and also takes neighboring CMP gathers into account, acknowledging the fact that reflection events are caused by spatially contiguous reflector elements in depth. In this way, an increased number of traces

contributing to the stack allows to obtain a simulated ZO section with higher signal-to-noise ratio. At the same time, a whole set of stacking parameters, the so-called kinematic wavefield attributes, is obtained for each simulated ZO sample without explicit knowledge about the subsurface structure and velocity model. Thus, *data-driven stacking method* might be a more appropriate terminology because it emphasizes that the results depend on the data which, in turn, depend on the subsurface structure and velocity model (Vieth, 2001).

In this chapter I will restrict the discussion of the CRS method to its very basic essentials which are required in the scope of this thesis. Afterwards, the conflicting dip problem and most important reason for inability of CRS to handle this problem will be discussed. Then, the extended search strategy and the common-diffraction-surface (CDS) stack method, their capabilities and their drawbacks to solve the conflicting dip situations will be explained.

3.1 The CRS stacking operator

The CRS operator describes a reflection event in vicinity of a ZO sample by means of a second-order approximation of travel time. A special appropriate form of CRS the operator is obtained in midpoint and half-offset coordinates. By using these coordinates, it is possible to interpret the stacking parameters geometrically, i.e., in terms of wavefronts properties.

3.1.1 Traveltime approximation

As already mentioned, the CRS method is based on an analytical approximation of the traveltime up to second-order in terms of half source/receiver offset h, and the displacement of the source/receiver midpoint x_m with respect to the location of stacked trace x_0. Possible ways to derive this approximation are

- Paraxial ray theory, i.e., the assumption of a linear relation between the properties of neighboring rays (see, e.g., Ursin, 1982; Bortfeld, 1989; Schleicher et al., 1993)
- Geometrical optics using the concept of object and image points (see, e.g., Höcht et al., 1999)
- The pragmatic way: a second-order approximation of travel time initially without any physical interpretation (Mann and Zhang, 2003).

In the following I will briefly discuss the pragmatic approach. A second-order traveltime approximation with respect to an arbitrarily chosen point on a reflection event in the prestack data (like P_0 in Figure 1.9) can be described by any (hyper-)surface that includes the point P_0 itself and coincides with the actual reflection event with respect to its first and second spatial derivatives at P_0. The surface fitting best the actual reflection events, together with the spatial derivatives that serve as its parameters, can be determined by means of a coherence analysis within an appropriate aperture in the prestack data.

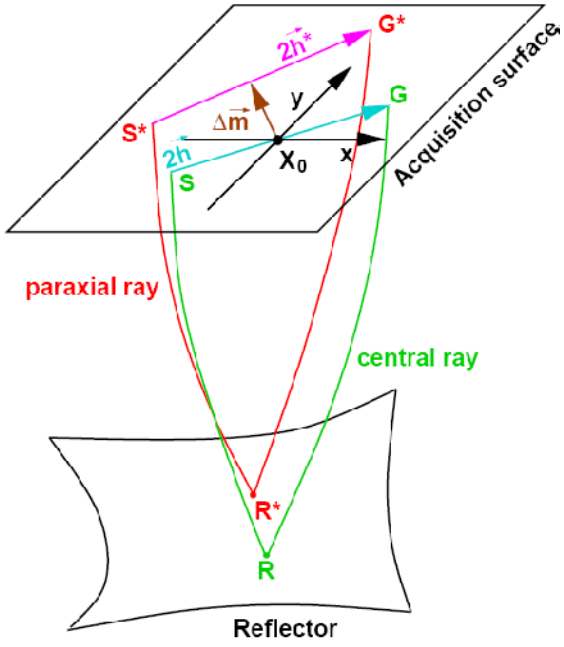

Figure 3.1: Geometry of seismic data acquisition in the general 3-D case. The traveltime up to second order along the paraxial ray (shown in red) is derived by a Taylor expansion from the known traveltime along the central ray (shown in green).

In Figure 3.1 a planar measurement surface which coincides with the (x, y)-plane of the general Cartesian coordinate system is considered. Source and receiver on the measurement surface both are defined by vectors with two components. For a source and a receiver with coordinate $\vec{s}=(s_x, s_y)$ and $\vec{g}=(g_x, g_y)$ respectively, midpoint and half-offset are given by the relations

$$\vec{m} = \begin{pmatrix} m_x \\ m_y \end{pmatrix} = \frac{1}{2}\begin{pmatrix} g_x + s_x \\ g_y + s_y \end{pmatrix}, \quad \vec{h} = \begin{pmatrix} h_x \\ h_y \end{pmatrix} = \frac{1}{2}\begin{pmatrix} g_x - s_x \\ g_y - s_y \end{pmatrix} \tag{3.1}$$

Therefore, in the general case of 3-D acquisition with full azimuth coverage the prestack data consist of a 5-D (hyper-)volume spanned by the traveltime *t*, the midpoint coordinate $\vec{m}$, and the half-offset coordinate $\vec{h}$. The traveltime of reflection events in prestack data with 5-D (hyper)volume is define by (hyper-)surface with midpoint and half-offset coordinates $t(\vec{m},\vec{h})$.

Let us assume that the travel time $t(\vec{m},\vec{h})$ along the central ray from source S to the reflector R and from reflector R to the receiver G is known, see Figure 3.1. Now the approximation for travel time $t(\vec{m}+\Delta\vec{m},\vec{h}+\Delta\vec{h})$ along the paraxial ray $(S^*R^*G^*)$ by applying a Taylor expansion reads as follows

$$\begin{aligned} t(\vec{m}+\Delta\vec{m},\vec{h}+\Delta\vec{h}) \\ &\approx t(\vec{m},\vec{h})+\frac{\partial t}{\partial m_x}\Delta m_x+\frac{\partial t}{\partial m_y}\Delta m_y+\frac{\partial t}{\partial h_x}\Delta h_x+\frac{\partial t}{\partial h_y}\Delta h_y \\ &+\frac{1}{2}\left(\frac{\partial^2 t}{\partial m_x^2}\Delta m_x^2+\frac{\partial^2 t}{\partial m_y^2}\Delta m_y^2+\frac{\partial^2 t}{\partial h_x^2}\Delta h_x^2+\frac{\partial^2 t}{\partial h_y^2}\Delta h_y^2\right) \\ &+\frac{\partial^2 t}{\partial m_x\partial m_y}\Delta m_x\Delta m_y+\frac{\partial^2 t}{\partial m_x\partial h_x}\Delta m_x\Delta h_x \\ &+\frac{\partial^2 t}{\partial m_x\partial h_y}\Delta m_x\Delta h_y+\frac{\partial^2 t}{\partial m_y\partial h_x}\Delta m_y\Delta h_x \\ &+\frac{\partial^2 t}{\partial m_y\partial h_y}\Delta m_y\Delta h_y+\frac{\partial^2 t}{\partial h_x\partial h_y}\Delta h_x\Delta h_y \end{aligned} \tag{3.2}$$

Thus, four first spatial derivatives and ten second spatial derivatives are required to fully describe a second-order approximation of the traveltime (Mann and Zhang, 2003). If we consider the particular problem of ZO simulation, where shot and receiver coincide, the terms in Equation (3.2) which include exactly one derivative with respect to $\vec{h}$ will vanish. Accordingly, two first derivatives and six second derivatives remain in 3-D:

$$\begin{aligned} t(\vec{m}+\Delta\vec{m},\vec{h}+\Delta\vec{h}) \\ &\approx t(\vec{m},\vec{h})+\frac{\partial t}{\partial m_x}\Delta m_x+\frac{\partial t}{\partial m_y}\Delta m_y \\ &+\frac{1}{2}\left(\frac{\partial^2 t}{\partial m_x^2}\Delta m_x^2+\frac{\partial^2 t}{\partial m_y^2}\Delta m_y^2+\frac{\partial^2 t}{\partial h_x^2}\Delta h_x^2+\frac{\partial^2 t}{\partial h_y^2}\Delta h_y^2\right) \\ &+\frac{\partial^2 t}{\partial m_x\partial m_y}\Delta m_x\Delta m_y+\frac{\partial^2 t}{\partial h_x\partial h_y}\Delta h_x\Delta h_y \end{aligned} \tag{3.3}$$

and for 2-D acquisition one first derivative and two second derivatives remain. Therefore, Equation (3.3) reads

$$t(\vec{m}+\Delta\vec{m},\vec{h}+\Delta\vec{h}) \approx t(\vec{m},\vec{h}) + \frac{\partial t}{\partial m_x}\Delta m_x + \frac{1}{2}\left(\frac{\partial^2 t}{\partial m_x^2}\Delta m_x^2 + \frac{\partial^2 t}{\partial h_x^2}\Delta h_x^2\right) \tag{3.4}$$

or

$$t(x_m,h) = t_0 + \frac{\partial t}{\partial x_m}(x_m - x_0) + \frac{1}{2}\left[\frac{\partial^2 t}{\partial x_m^2}(x_m - x_0)^2 + \frac{\partial^2 t}{\partial h^2}h^2\right] \tag{3.5}$$

Because of its parabolic form, Equation (3.5) is called parabolic traveltime. If we restrict our traveltime approximation (3.5) to the CMP gather only, $x_m - x_0 = 0$, we obtain a single second derivative which is traditionally interpreted in term of stacking velocity. Obviously, this is a special case of the general second-order approximation.

3.1.2 Physical interpretation of the stacking parameters

To obtain a more descriptive from of the CRS operator in the 2-D case the traveltime derivatives (see Equation 3.4) are expressed in terms of kinematic properties of two wavefronts emerging at the surface.

The derivative $\frac{\partial t}{\partial x_m}$ defines the horizontal component of the slowness vector $\vec{p}$ of the central ray, thus, it can be related to emergence angle α and near surface velocity v_0 via

$$p_x = \frac{1}{2}\frac{\partial t}{\partial x_m}\bigg|_{(x_m = x_0, h = 0)} = |\vec{p}|\sin\alpha = \frac{\sin\alpha}{v_0} \tag{3.6}$$

The derivatives $\frac{\partial^2 t}{\partial x_m^2}$ and $\frac{\partial^2 t}{\partial h^2}$ can be related to the wavefronts curvature of two hypothetical experiments (see Figure 1.11). The derivative $\frac{\partial^2 t}{\partial x_m^2}$ can be related to the normal (N) wave via

$$K_N = \frac{v_0}{2}\frac{1}{cos^2\alpha}\frac{\partial^2 t}{\partial x_m^2}\bigg|_{(x_m = x_0, h = 0)} \tag{3.7}$$

The derivative $\frac{\partial^2 t}{\partial h^2}$ is the curvature of CMP wavefront. Due to the fact that, up to second-order, CMP traveltimes and ZO diffraction traveltimes coincide (Hubral, 1983) it is possible to approximate the CMP wavefront by an exploding diffractor experiment which yields the so-called normal-incident-point (NIP) wavefront. The curvature of CMP wavefront is written as

$$K_{NIP} = \frac{v_0}{2}\frac{1}{cos^2\alpha}\frac{\partial^2 t}{\partial h^2}\bigg|_{(x_m = x_0, h = 0)} \tag{3.8}$$

Inserting (3.6), (3.7) and (3.8) into (3.5), the CRS operator can be expressed in term of kinematic wave field attributes

$$t(x_m, h) = t_0 + \frac{2\sin\alpha}{v_0}(x_m - x_0) + \frac{cos^2\alpha}{v_0}[K_N(x_m - x_0)^2 + K_{NIP}h^2] \tag{3.9}$$

If Equation (3.9) is squared and only the terms up to second-order in $(x_m - x_0)$ and h are retained (Schleicher et al., 1993), the hyperbolic counterpart reads

$$\begin{aligned} t^2(x_m, h) = & \left[t_0 + \frac{2\sin\alpha}{v_0}(x_m - x_0)\right]^2 \\ & + \frac{2t_0 cos^2\alpha}{v_0}[K_N(x_m - x_0)^2 + K_{NIP}h^2] \end{aligned} \tag{3.10}$$

With respect to Equation (2.41) it is possible to rewrite Equation (3.10) in terms of the radii of the curvatures of N and NIP waves

$$\begin{aligned} t^2(x_m, h) = & \left[t_0 + \frac{2\sin\alpha}{v_0}(x_m - x_0)\right]^2 \\ & + \frac{2t_0 cos^2\alpha}{v_0}\left[\frac{(x_m - x_0)^2}{R_N} + \frac{h^2}{R_{NIP}}\right] \end{aligned} \tag{3.11}$$

Tygel et al. (1997), Jäger (1999), and Müller (1999) have compared the parabolic and hyperbolic traveltimes. They showed that the hyperbolic approximation gives consistently better results than its parabolic counterpart.

3.1.3 Parameter search

The three attributes of the CRS stack operator which build up the best-fit traveltime with the kinematic response of the subsurface layers are determined by coherence analysis. The desired attributes yield the maximum value of coherence within the user-defined range for each attribute. In other words, the coherence analysis is performed in a 3-D space, formed by one emergence angle and two curvatures. The used coherence analysis criterion is semblance defined together with different other coherence measurements in Taner and Koehler (1969) and Neidell and Taner (1971). Computationally, it is very expensive to determine the three attributes at once. Therefore, Müller (1999) and Jäger (1999) introduced a pragmatic search strategy which involves three subsequent one-parameter search steps. Optionally, a local optimization can be performed in the 3-D attribute domain where the initially found parameters are the starting points and the optimized values are obtained simultaneously. The optimization strategy, which is very time consuming, uses the flexible polyhedron search proposed by Nelder and Mead (1965). In the following, I will briefly explain how a ZO section is simulated from multi-coverage data set by means of the CRS stack method. The following steps are described for the hyperbolic traveltime Equation (3.10), but they are the same for the use of the parabolic traveltime, Equation (3.9).

- **First step:** A one-parameter search for the combined parameter v_{NMO} is performed within the CMP gather, $x = x_0$, and Equation (3.11) reads

  $$t^2(x_m, h)\Big|_{x = x_0} = t_0^2 + \frac{2t_0 cos^2\alpha h^2}{v_0 R_{NIP}} \tag{3.12}$$

  Comparing to Equation (1.1) the stacking velocity can be expressed by means of α and R_{NIP} (Hubral and Krey, 1980).

  $$v_{NMO}^2 = \frac{2v_0 R_{NIP}}{t_0 \cos^2 \alpha} \tag{3.13}$$

  This step is called Automatic CMP stack (Mann et al., 1999) and proposes a non-interactive velocity analysis which is a well-known procedure for the CMP stack method.

- **Second step:** the automatic CMP stack provides a ZO section in which Equation (3.11) reduces to

$$t(x_m, h)\Big|_{h=0, R_N=\infty} = t_0 + \frac{2sin\alpha}{v_0}(x_m - x_0) \tag{3.14}$$

This first-order approximation is equivalent to a plane wave approximation as $R_N=\infty$. From this step, the so-called plane wave stack, the emergence angle α is obtained. Inserting this angle into Equation (3.13), a solution for R_{NIP} is found.

- **Third step:** while α and R_{NIP} are already known, the third parameter R_N is searched in the CMP stacked section by means of

$$t^2(x_m, h)\Big|_{h=0} = \left[t_0 + \frac{2\sin\alpha}{v_0}(x_m - x_0)\right]^2 + \frac{2t_0 cos^2\alpha (x_m - x_0)^2}{v_0 R_N} \tag{3.15}$$

The value of R_N associated with the maximum coherency is chosen to simulate the corresponding ZO point in step four.

- **Fourth step:** After all parameters have been determined for a certain ZO sample, they can be used for traveltime computation with Equation (3.11). The subsequent stack along the traveltime surface is called initial CRS stack. The word initial is used to emphasize that the determined parameters serve as initial values for the optional optimization process which is yielded the optimized CRS stack.

Mann (2002) summarized these four steps into a flowchart which is shown in Figure 3.2.

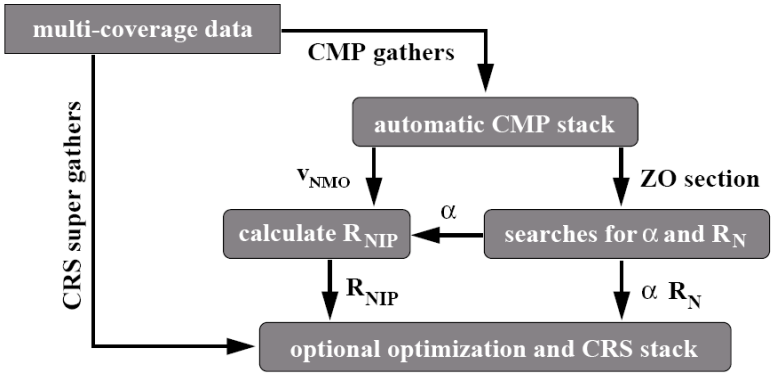

Figure 3.2: Flowchart of the pragmatic search strategy. The indicated processing steps have to be performed for each ZO sample to be simulated. All traces in the spatial CRS aperture are denoted as CRS super gather (Mann, 2002).

The validity of the second-order traveltime approximation (3.9) and (3.10) depends on the aperture chosen for the determination of the stacking parameter. In general, for a certain ZO sample, the aperture decreases with increasing distance in midpoint and half-offset direction such that the aperture is of elliptical shape. For further details on the implementation of the aperture, see, e.g., Mann (2000), Vieth (2001), Mann (2002), and Müller (2006).

The main drawback of the CRS stack procedure is that this method cannot handle conflicting dip situations (Mann, 2002). In the following, I will shortly explain a) how the conflicting dip situations arise, b) why the CRS stack procedure cannot address such conflicting dip situations, and c) what kinds of problems might occurs in the presence of conflicting dip situations.

3.2 Conflicting dip situations

A very simple model of geological structures which consist of several reflector and diffraction sources is depicted in Figure 3.3a. The kinematic response of this model for the ZO configuration is illustrated in Figure 3.3b. The edges of the faults act as point sources and appear as hyperbolic in the ZO section. Additionally, the response of syncline appears as a bow-tie in the ZO section. As indicated by the arrows in Figure 3.3b various events intersect each other such that several events contribute to the same ZO location (sample) which causes conflicting dip situations.

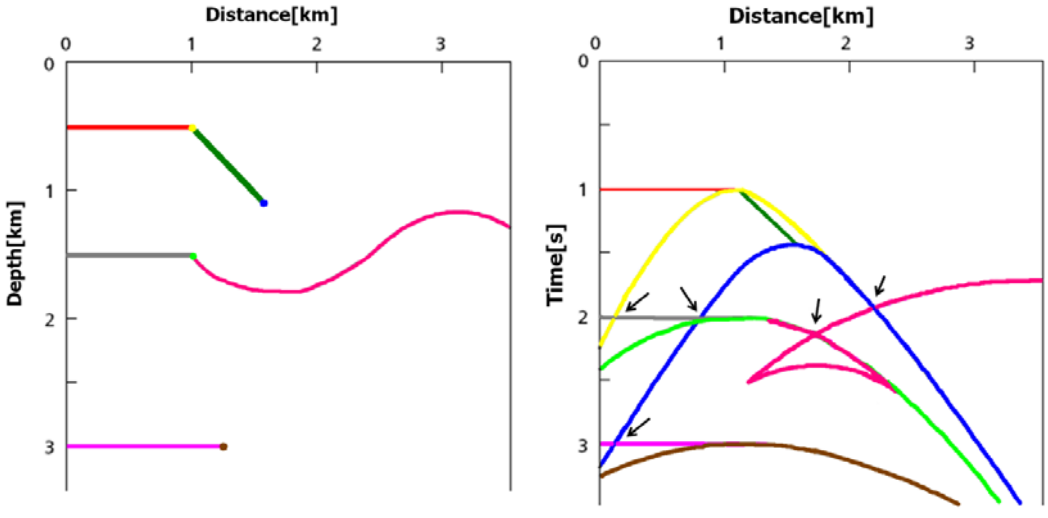

Figure 3.3: a) A structural model of the subsurface b) Its kinematic response in the ZO section containing numerous conflicting dip situations (after Kearey, 2002).

In terms of ray theory, conflicting dip situations are generated by contribution of multiple ZO rays with different emergence angles to one and the same ZO sample. Handling the conflicting dip to simulate a ZO section is very important for a subsequent poststack migration process, because the lack of coherent energy along the less prominent events might case shadow zones in the migration result.

The CRS stack approach in its simplest implementation determines only one stacking operator for each ZO sample to be simulated. Along this optimum operator, we obtain the maximum coherence in seismic reflection data. If there is only one reflection event contributing to the considered sample or no coherent event at all, this is sufficient. However in presence of curved reflectors or diffractors various events might intersect each other or/and themselves, such that a single stacking operator per ZO sample is no longer sufficient to simulate a stacked section containing all relevant contributions. To account for such conflicting dip situations another configuration should be considered to search for the other attributes.

3.3 Extended search strategy in the CRS stack method

The three steps of the pragmatic search strategy see section 3.1.3, have to be modified if conflicting dips are to be correctly taken into account. According to Equation (3.13) the stacking velocity v_{NMO}, is not very sensitive to the emergence angle α, thus, we cannot rely on the first step of pragmatic search strategy, i.e. the automatic CMP stack to separate events with different emergence angles because the associated stacking velocities might be similar or even identical. In addition, the sign of emergence angle α cannot be determined by means of Equation (3.14).

To resolve the problem of conflicting dips, Mann (2001, 2002) introduced the extended search strategy into the CRS stack method. In contrast to the DMO correction which collects the information of all possible contributing events with different dips, he proposed to allow for a small discrete number of stacking operators at each ZO sample to be simulated. Consequently, it is firstly required to identify the samples where such conflicting dip situations occur. For this purpose the angle spectrum, which is the coherence as function of emergence angle along a linear operator in the CMP stacked section, should be calculated. An angle spectrum is depicted in Figure 3.4 for a ZO sample located on an actual event. Three distinct maxima can be observed that in this example, correspond to two diffraction events

and one reflection event intersecting each other in the chosen ZO location. Furthermore, there are various local maxima that do not appear to belong to any visible events.

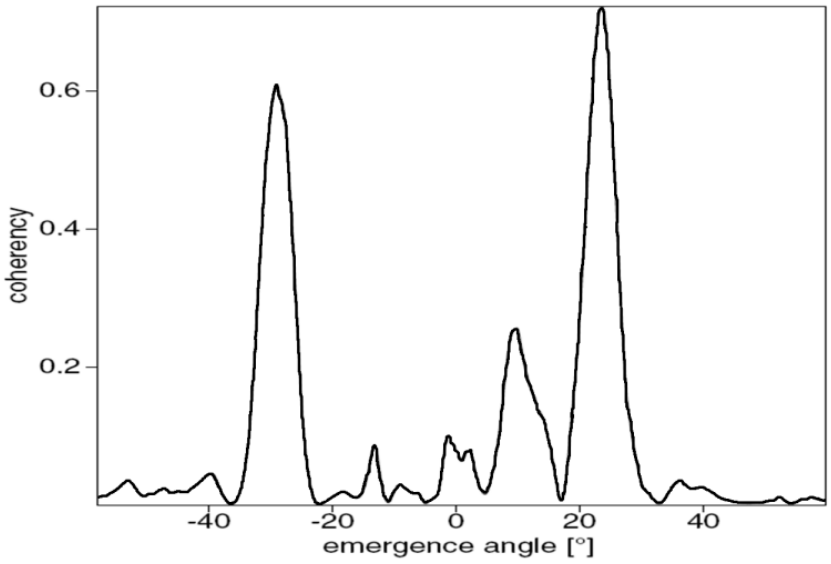

Figure 3.4: Coherence as function of emergence angle α calculated along a linear operator in the CMP stacked section for a chosen ZO sample. The three clear maxima relate to two diffractions at ≈-30° and ≈ 25°and one weak reflection at ≈12° (Mann, 2001)

If an event exceeds a user-defined coherence threshold the related operator will be considered for the stacking process, else it will be rejected. After detecting the samples where the conflicting dip problem occurs, the linear ZO search is performed for each separate emergence angle $\alpha^{(i)}$ (i denotes different contributing events) that was determined at the previous step. Afterwards the hyperbolic ZO search is done again separately for each detected event and provides the radius of curvature $R_N^{(i)}$ for each contributing dip. In the pragmatic CRS strategy, R_{NIP} is calculated from the relation between v_{NMO}, obtained in the first step and the emergence angle. However, the calculation of R_{NIP} from α and v_{NMO} according to Equation (3.13) is no longer possible because in general we will detect more than one emergence angle but only one value for the stacking velocity v_{NMO}. According to the stacking operator (3.11), $R_{NIP}^{(i)}$ does not influence in ZO section (h=0) and cannot be separated from α in the CMP gather ($x_m=x_0$), thus, $R_{NIP}^{(i)}$ can be determined neither in the CMP stack section nor in the original CMP gathers. To solve this problem, Mann (2001)

proposed the additional search for $R_{NIP}^{(i)}$ in another subset of the multi-coverage data set, namely the CS/CR gathers where $h^2 \approx (x_m - x_0)^2$. Consequently, in this step for each angle $\alpha^{(i)}$ and each $R_N^{(i)}$, one search for $R_{NIP}^{(i)}$ is performed. Finally, all wavefield attributes are available for each ZO location. A simplified flowchart of this strategy is depicted in figure 3.5.

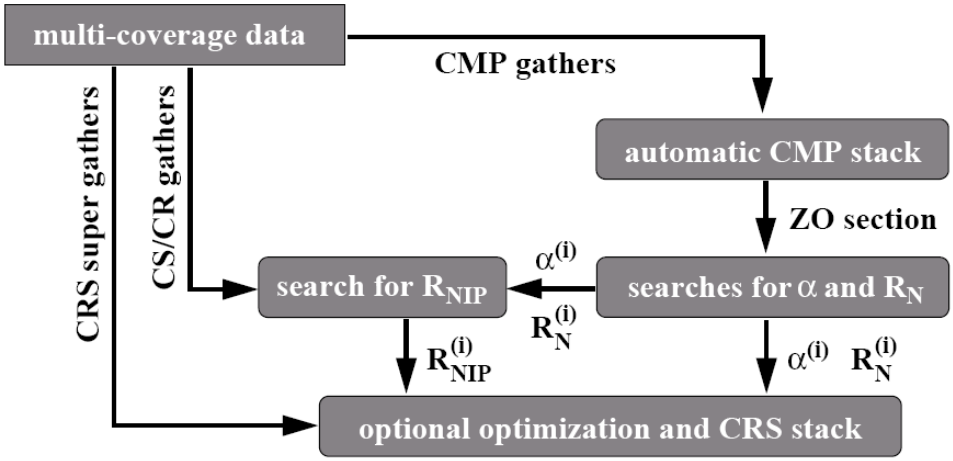

Figure 3.5: Simplified flowchart of the extended search strategy. The indicated processing steps have to be performed for each ZO sample to be simulated. All traces within the spatial CRS aperture are denoted as CRS super gather (Mann, 2002).

Here, the important point is that, if the user-defined threshold is set too low, not only many spurious events are consider as contributing events, but also more computation time is needed. In contrast, if it has been set too high, some relevant contributing events may be lost. The main difficulty in this approach is to identify the conflicting dip situations and to decide how many contributions should actually be considered. This implies a tricky balancing between lacking contributions and potential artifacts to the unwanted parameterization of spurious events. Due to the discrete number of considered events, the number of detected and, thus, imaged events might change from sample to sample such that seismic events might still show up fragmented.

3.4 Common-Diffraction-Surface (CDS) stack

To obtain a stack section containing all intersecting events Soleimani et al. (2009a,b) proposed an adapted CRS strategy by merging concepts of the DMO correction (e.g. Hale, 1991) with the CRS approach: instead of allowing only a small discrete

number of stacking operators per sample, a virtually continuous range of dips is considered.

3.4.1 Dip-Moveout (DMO) operator

The MZO can be split into two approximate processes, namely the NMO correction and the DMO correction. The NMO correction considers the moveout due to the overburden of a reflector while the DMO correction considers the moveout due to the dip of a reflector. The pragmatic search strategy specifies only one optimum emergence angle and the extended strategy determines only a small discrete number of emergence angles to simulate a ZO sample. However, as there is no reliable criterion to determine the number of optimum emergence angles for each ZO location, this strategy fails to preserve the continuity of event particularly in presence of complex structures. To overcome the drawback of previous strategy, Soleimani (2009) proposed to use the idea of DMO operator.

Deregowski and Rocca (1981) described the time domain impulse response of DMO operator. In 2-D homogeneous media the impulse response is a semicircle for ZO and an ellipse for finite offset. Each point on a DMO operator corresponds to a particular reflector dip. In other words all slopes on the semicircle ($h=0$) or ellipse ($h\neq0$) construct the DMO operator. In Figure 3.6, different DMO Huygens image wave for different offsets are shown. One of these image waves (shown in green) will be applied for DMO processing. In Figure 3.7 the result of DMO processing on the image wavefront (dark blue curve) is depicted by a cyan curve for constant offset ($h=200m$). This figure shows that the DMO operator provides lateral moveout for each dip. Since a DMO operator considers all reflectors with different dips, the DMO processing can handle conflicting dip problem (Mann, 1997).

3.4.2 The concept of the CDS stack approach

In CDS stack method the same idea as in the DMO process was used to address the problem of conflicting dips. In the view of the angle spectrum, it is like to neglect the coherence threshold, i.e. for all dips we have a stacking surface without taking the value of coherence into account. Instead, a user-defined angle search range ($\alpha_{min}, \alpha_{max}$) is defined with increment $d\alpha$.

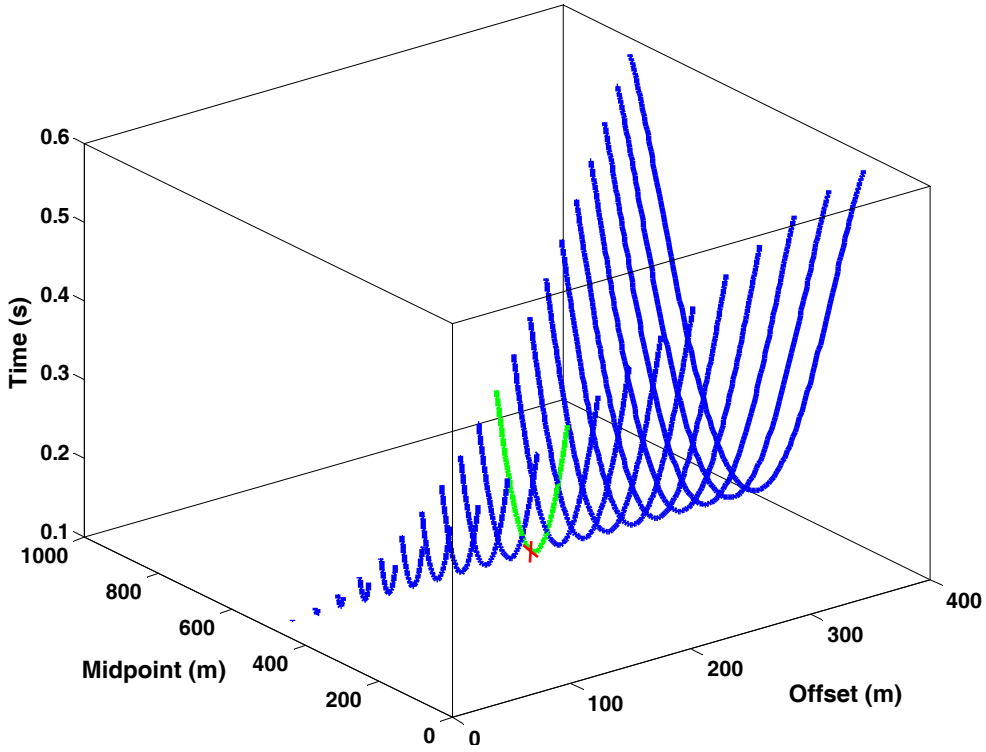

Figure 3.6: Snapshot of the DMO Huygens image wave for different offset. One of this image wave is shown in green for offset *h=200m*.

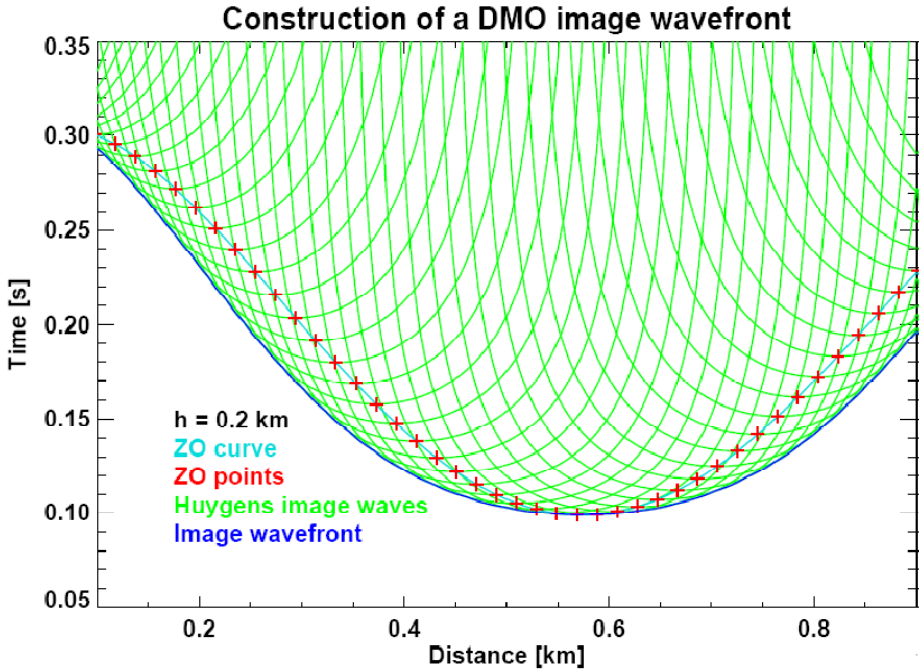

Figure 3.7: Construction of an image wavefront for the inverse DMO problem for constant offset (*h=200m*) (Mann, 1997).

Thus, in the multi-coverage data set instead of one emergence angle several angles are considered, corresponding to the number of angles in desired angle range. The lower part of Figure 3.8 shows the isochrone for a ZO sample $P_0(x_m, t)$ in the depth domain. For each ray emerging at the surface at x_m within the desired angle range, a stacking surface contributes to the stack to simulate a ZO sample. This multitude of operator establishes so-called operator volume, which is shown at the upper part of Figure 3.8 in time domain.

As the coherence analysis is done for an entire range of angles for each ZO sample, there are hundreds of different contributions to each ZO sample. Consequently, having a unique coherence section is impossible (Soleimani, 2009).

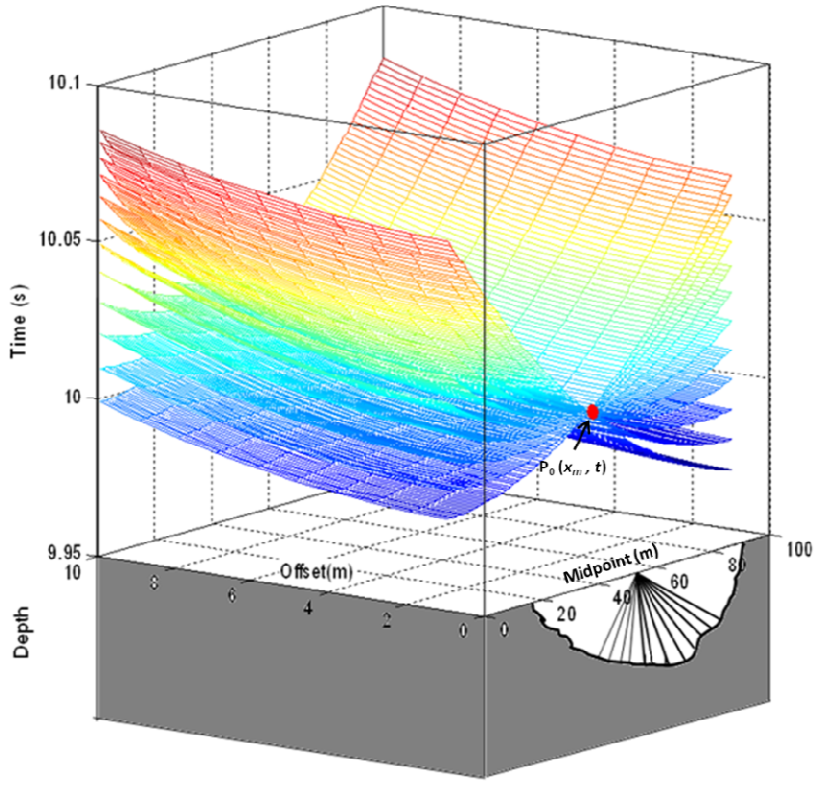

Figure 3.8: Lower part: isochrone for a ZO sample $P_0(x_m, t)$. All rays emerge at the surface at point x_m. Upper part: the multitude of stacking surface whichs set up the operator volume.

In the ZO section we often encounter intersection of reflections and diffraction events (see, e.g., Figure 3.3). The new strategy proposed by Soleimani (2009) enhances the diffraction events by applying CRS operator which is reduced to hypothetical exploding point source (diffraction). This so-called common-

diffraction-surface (CDS) stack not only addresses diffraction events but also considers the reflection events within a reasonable aperture.

3.4.3 CDS traveltime approximation

For a true diffractor in the subsurface, an exploding point source experiment and an exploding reflector experiment obviously coincide such that $R_{NIP} \equiv R_N$. Thus, for diffraction events, the CRS traveltime Equation (3.11) reduces to the CDS traveltime approximation

$$t^2(x_m, h) = \left[t_0 + \frac{2\sin\alpha}{v_0}(x_m - x_0)\right]^2 + \frac{2t_0 cos^2\alpha}{v_0 R_{CDS}}[(x_m - x_0)^2 + h^2] \qquad (3.16)$$

with $R_{CDS} \equiv R_{NIP} \equiv R_N$. For reflection events, the CDS operator (3.16) is an inferior approximation compared to the full CRS operator (3.11) as $R_{NIP} \neq R_N$ if the curvature of the reflector is not too large (a diffractor can be seen as a reflector with infinite curvature). Nevertheless, Equation (3.16) still allows to approximating the events within a reasonably chosen aperture.

3.4.4 CDS search strategy

The only unknown wavefield attribute in Equation (3.16) is R_{CDS}. As illustrated in Figure 3.9 for a fixed emergence angle $\alpha^{(i)}$, $R_{CDS}^{(i)}$ is searched in a user-defined range and the coherence value is calculated along all operators which are specified by $\alpha^{(i)}$ and $R_{CDS}^{(i)}$. The parameter $R_{CDS}^{(i)}$ within its related operator yielding the maximum coherence is the desired $R_{CDS}^{(i)}$. This process is repeater for all angles in a user-defined angle range. Consequently, by considering all possible angle in Equation (3.16) a set of weighted operators constituting a volume instead of a single stacking surface are taken in to account to simulate a ZO sample. This will enhance any weak reflection and diffraction events which were obscured by dominant coherent events in previous strategy. Figure 3.10 shows a simplified flowchart of the CDS stack strategy. Garabito et al. (2001a,b) also used the CDS operator (3.16) for stacking. However, they applied it in a simultaneous two-parameter search for the combination of emergence angle α and the radius R_{CDS} yielding the highest coherence. Using only one operator per ZO sample, this data-driven approach does not address the conflicting dip problem considered here.

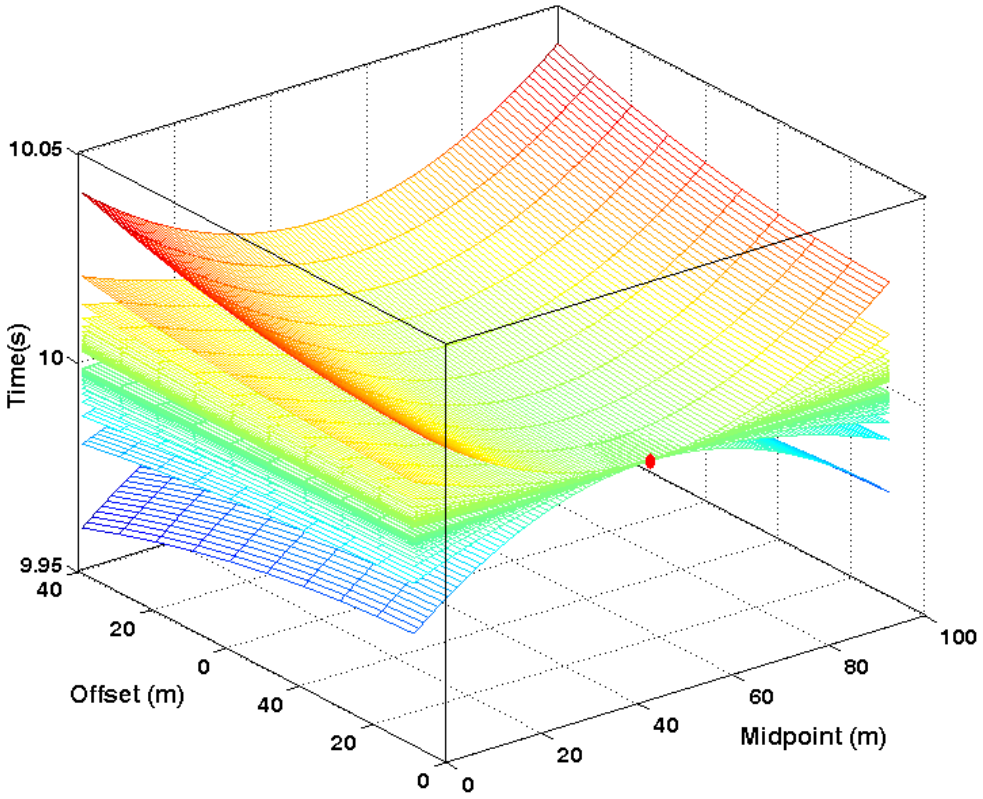

Figure 3.9: For a fixed emergence angle α (in this figure $\alpha = 0$) the radius R_{CDS} is searched within a user-defined range.

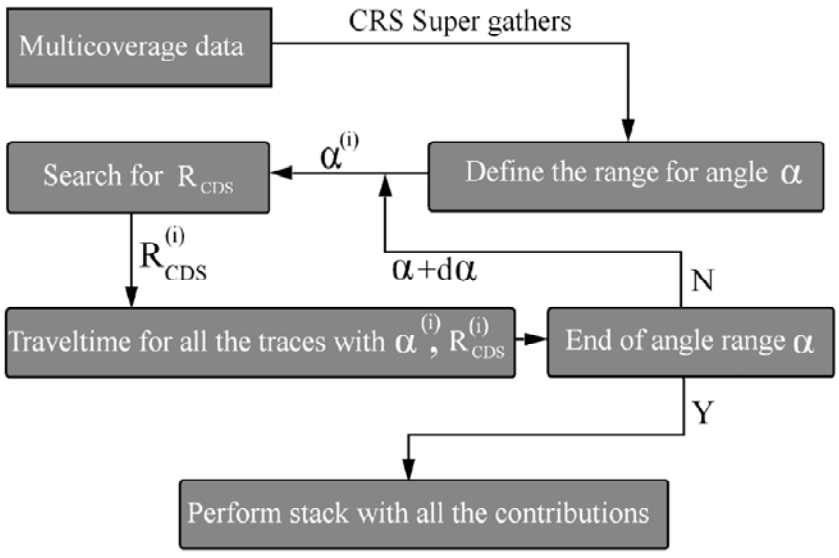

Figure 3.10: Simplified flowchart of the CDS search strategy (Soleimani, 2009).

3.4.5 Limitations

The background noise effectively influences the resolution and quality of the output section in the CDS stack strategy. Since for each angle there is a stacking surface that can be related to a spurious event, the CDS stack approach may enhance the noise compare to the CRS stack (Soleimani, 2009).

In addition, the CDS stack approach which has been successfully applied to complex land data (Soleimani et al., 2010), is quite time consuming, because separate stacking operators have to be determined for each stacked sample to be simulated and each considered dip in a data-driven manner by means of coherence analysis in the prestack data.

In the following chapters I will propose and apply a model-based approach to the CDS stack to overcome the drawback of the data-driven CDS stack.

Chapter 4

Model-based common-diffraction-surface stack method

In the previous chapters the concept of ray theory and the latest data-driven method i.e. the CDS stack, have been explained. Although the data-driven CDS method has been successfully applied on a synthetic and real data (Soleimani, 2009), it has some limitations.

This chapter is devoted to the implementation of a model-based CDS stack which uses the concepts of ray theory to overcome the drawbacks of the previous method. In the proposed method, the attribute R_{CDS} can be easily forward-modelled by means of kinematic and dynamic ray tracing. In this way, a complete stacked section optimized for poststack depth migration can be generated in a much more efficient manner compared to the data-driven CDS approach.

4.1 Forward modeling

As mentioned in section 3.4.3, the radius of the NIP wave occurring in the CDS operator (3.16) is associated with a hypothetical exploding diffractor at the NIP. The local curvature of the hypothetical wavefront triggered by such a point source is considered along the normal ray. The wavefront finally reaches the acquisition surface with the curvature $1/R_{NIP}$, see Figure 4.1. Consequently, the first step to model this parameter is to determine the potential normal ray by means of kinematic ray tracing. As we need these rays for a given surface location and emergence angle, the kinematic ray tracing should be done for down-going rays.

4.1.1 Kinematic ray tracing

Kinematic ray tracing consists in the calculation of the characteristic of the eikonal equation which governs the kinematics of a wavefield in a 2-D velocity field $v(x, z)$ (see Equation 2.12) for given initial conditions. I have chosen a particular system for which the variable along the ray is directly the travel time, as I have to compute the ray tracing result for a regular grid in ZO travel time (see Equation 2.19).

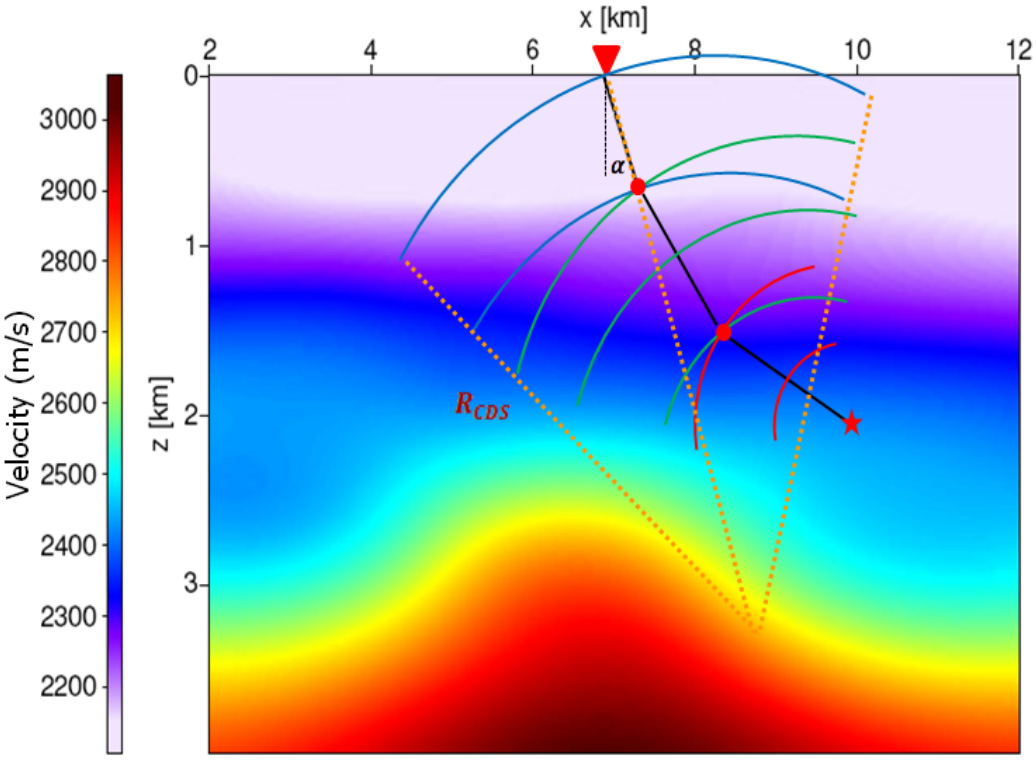

Figure 4.1: A point source (diffractor) in depth emits a wave to the surface. One ray of this wave (shown by a black line) connects the diffractor to the surface. The curvature of the wave that arrives at the surface with the emergence angle α is the curvature of NIP wave.

The corresponding kinematic ray tracing system that in 2-D consists of a system of four coupled nonlinear partial differential equations of first order can be numerically integrated with the well-known Runge-Kutta scheme of fourth order (Butcher, 1993). The step length in the numerical solution is chosen as an integer fraction of the sampling rate of the stacked section to be simulated. In this way, we directly obtain the discrete points along the ray paths corresponding to the desired output locations in the ZO time domain.

As $|\vec{p}| \equiv 1/v(x,z)\ \forall\ \vec{x}$ the slowness components are not independent of each other such that the system of equations can be further reduced. However, using Cartesian coordinates, the reduced system is not able to handle turning rays. In fact due to numerical inaccuracies, $|\vec{p}|$ slowly starts to deviate from $1/v(x,z)$ with increasing length of the ray path which would violate the eikonal Equation (2.12). Therefore, I use the full system of equations and enforce the relation between slowness and velocity by an according rescaling of $\vec{p}$ after each ray tracing step.

4.1.2 Dynamic ray tracing

The determination of R_{NIP} additionally requires dynamic ray tracing along the ray path. The derivation of the dynamic ray tracing system again starts with the eikonal equation, now defined in ray-centered coordinates (u, n), with u being the coordinate tangent to the ray and n the coordinate normal to the ray. A Taylor expansion of the phase function $T(u, n)$ in the vicinity of the central ray Ω up to the second order in n yields (Červený, 1981a)

$$T(u,n) \approx T(u,0) + \frac{1}{2}\left[\frac{\partial^2 T(u,n)}{\partial n^2}\right]_{n=0} n^2 \tag{4.1}$$

which introduces the second partial derivative **M** of the traveltime normal to the central ray

$$M(u) = \left[\frac{\partial^2 T(u,n)}{\partial n^2}\right]_{n=0} \tag{4.2}$$

The resulting ordinary differential equation of Riccati type (Hille, 1997) finally yields the dynamic ray tracing system consisting of two coupled ordinary differential equations of first order. For our chosen propagation variable $u \equiv t$ along the central ray, this system reads

$$\frac{dt}{dq} = v^2 p, \quad \frac{dt}{dp} = -\frac{1}{v}\frac{\partial^2 v}{\partial n^2} q \tag{4.3}$$

which can be easily numerically integrated along the ray in parallel to the kinematic ray tracing described above. The properties p and q are related to different coordinate transforms, see Section 2.3.3 for details. The only important property here is that their ratio coincides with the second traveltime derivative normal to the ray, equation (4.2)

$$M(u) = \frac{p(u)}{q(u)} \tag{4.4}$$

In turn, for a point source at the NIP, $M(u_0)$ at the emergence point of the normal ray is directly related to the searched-for value of R_{CDS}:

$$\frac{1}{R_{CDS}} = v_0 M(u_0) = v_0 \frac{p(u_0)}{q(u_0)} \tag{4.5}$$

with v_0 again representing the near-surface velocity at the emergence point.

A straightforward approach to this task is to integrate the dynamic ray tracing system upwards along the ray for a given point on the known down-going ray path with the according initial condition for a point source initial condition in the starting point, i. e., q = 0 and p = 1. However, this approach is highly inefficient for two reasons:

- dynamic ray tracing had to be performed separately for each considered point on the ray, i. e., hundreds or thousands of times along each ray
- either the entire down-going ray paths had to be kept in memory, or kinematic ray tracing has to be repeated along the up-going ray path again

Instead, it is far more efficient to perform the dynamic ray tracing in parallel to the kinematic ray tracing along the down-going ray. However, in this way I cannot directly control the desired "initial" condition at the NIPs, because now the initial conditions are defined at the acquisition surface rather than at the NIPs. Fortunately, this problem can be addressed by solving the dynamic ray tracing system for two mutually orthogonal initial conditions, a point source and a plane wave at the initial point. The initial condition for the latter reads q = 1 and p = 0. Using the index 1 for the plane wave initial condition and index 2 for the point source initial condition, the solutions can be gathered in a ray propagator matrix Π:

$$\Pi(\mathrm{u}, \mathrm{u}_0) = \begin{pmatrix} \mathrm{q}_1 & \mathrm{q}_2 \\ \mathrm{p}_1 & \mathrm{p}_2 \end{pmatrix} \tag{4.6}$$

which can be computed for any value of u along the ray with the two initial conditions being defined at the emergence location of the central ray associated with u_0. The ray propagator matrix $\Pi(u, u_0)$ can be easily converted into the corresponding propagator matrix $\Pi^{\mathrm{b}}(u_0, u)$ describing the dynamic properties in opposite propagation direction along the ray:

$$\Pi^{b}(u_0, u) = \begin{pmatrix} p_2 & q_2 \\ p_1 & q_1 \end{pmatrix} \tag{4.7}$$

The first column of Π^{b} again corresponds to the plane wave initial conditions and the second column to the point source initial conditions, but these initial conditions are now defined at the considered point *u* on the central ray. As we compute Π along the down-going ray for all required locations *u* on the ray, Π^{b} is readily available, too. Its second column directly provides the searched-for solution of the dynamic ray tracing system at the emergence point of the central ray for a point source initial condition at any considered point *u* along the ray:

$$\frac{1}{R_{cds}} = v_0 \frac{q_1(u)}{q_2(u)} \tag{4.8}$$

Note that the meaning of R_{CDS} depends on the way this stacking parameter is determined: in the forward-modeling discussed here, it is a completely local second-order property $R_{NIP,mod}$ of the emerging NIP wavefront at the considered ZO location. In the CRS stack, the second-order property $R_{NIP,data}$ is determined from the prestack data within a finite aperture. Thus, $R_{NIP,data}$ is, in general, subject to spread length bias and does not exactly coincide with the forward-modeled $R_{NIP,mod}$ (Müller, 2006). In the data based CDS stack, R_{CDS} is influenced by both data-derived attributes $R_{NIP,data}$ and $R_{N,data}$. It represents a kind of weighted average of these both attributes, depending on the aspect ratio of the used aperture. In the context of this thesis, I consider the forward-modeled case, i. e., $R_{CDS} \equiv R_{NIP,mod}$.

4.2. Implementation aspects

The existing 2-D implementation of the CRS stack discussed in Mann (2002) has been extended to allow for a model-based calculation of the stacking parameters. The developed source code was written in an object-oriented-programming (OOP) way applying the well-known programming language C++ (Stroustrup, 1997).

The implementation relies on all the existing classes for Input/Output (I/O), stacking, semblance calculation aperture handling etc., just as the data-driven counterparts. Note that I have changed the aperture definition according to section 4.4. In addition to a new class which actually performs the stacking process, two additional classes

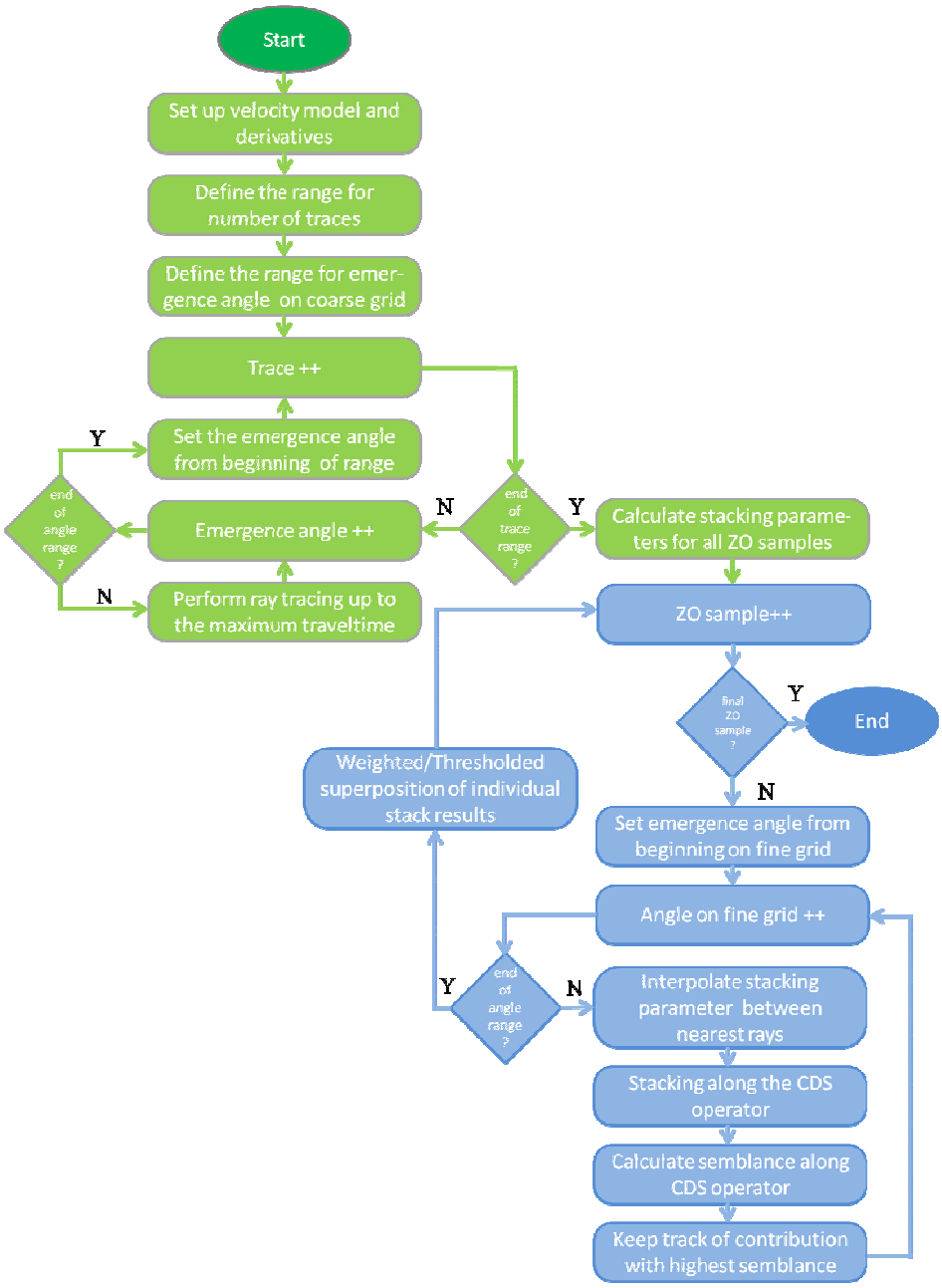

Figure 4.2: Model-based CDS stack process algorithm: ray tracing is performed on a coarse grid as R_{CDS} is not very sensitive to the emergence angle grid. This part is highlighted in green. In contrast, stack and semblance are calculated on a fine grid as they are sensitive to the emergence angle grid. This part of the process is shown in blue.

have been added: the first one provides the velocity model and its various spatial derivatives interpolated to any required depth location, the second one implements the kinematic and dynamic ray tracing systems and provides the CDS stacking

parameter directly on the ZO target grid. The algorithm of the model-based CDS stack approach is summarized in Figure 4.2.

In view of the fact that the stacking parameter varies smoothly for a smooth velocity model, the ray tracing can be performed on a relatively coarse emergence angle grid. The steps of this part of the process are highlighted by green in Figure 4.2. In contrast, stack and semblance are calculated on a finer emergence angle grid using linearly interpolated stacking parameters. These steps are indicated by blue in Figure 4.2.

The implemented ray tracing system generally supports turning rays such that e. g. overhanging flanks can be imaged. A smooth macro-velocity model which is obtained by sequence of CRS stack and NIP-wave inversion (Mann et al, 2003) is shown in Figure 4.3. Ray tracing is performed in this model for emergence angles ±50°@ 2° spacing. The ray fan for one of the ZO trace locations is superimposed on the model in Figure 4.3.

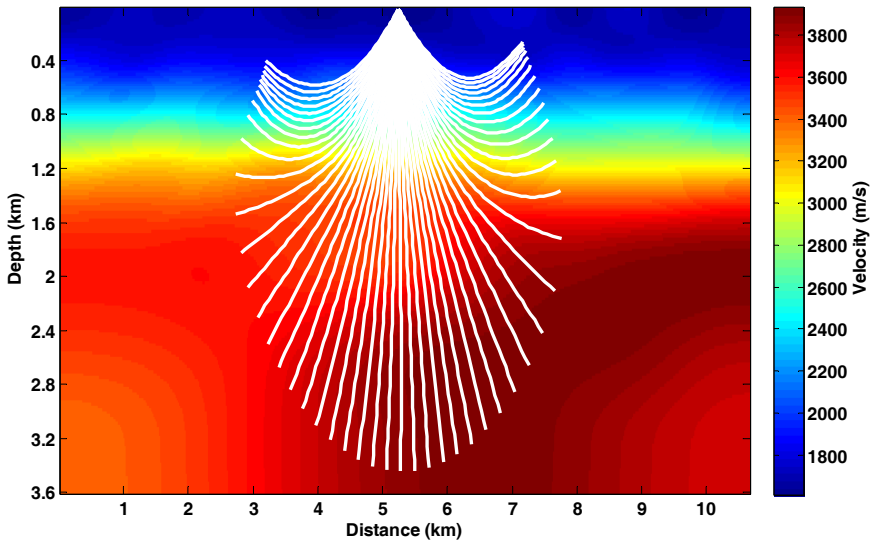

Figure 4.3: Macro-velocity model obtained by sequential application of CRS stack and NIP-wave inversion. For one emergence location, the ray fan for the coarse emergence angle grid is superimposed in white.

Depending on the complexity of the considered data, the user can decide whether turning rays should be further traced or simply terminated at their turning points. The latter option significantly speeds up the code, as many CDS operators unlikely to actually contribute to the image will not be evaluated at all. This especially applies to large ZO traveltimes combined with large emergence angles.

4.3 Model-based CDS stack attributes

Although the stacking parameters do not have to be optimized as in the data-driven approaches, it turned out to be quite useful to calculate semblance along the individual CDS operators anyway. Note that this has to be performed only once per emergence angle for each ZO sample rather than dozens or hundreds of times as in the data-driven CDS stack. Thus, the semblance calculation is not a performance issue in the model-based case but enables several additional features:

- I can keep track of the CDS operator yielding the highest semblance. In this way I can obtain

  - a section of the highest encountered semblance,
  - a section with the corresponding emergence angle α, and
  - a section with the corresponding radius of curvature R_{CDS}

  Obviously, these sections resemble the coherence section, the emergence angle section, and the R_{NIP} section of the data-driven CRS stack to some extent. Thus, they allow for the identification of ZO reflection events, the assessment of the quality of the operator fit, and plausibility analyses.
  Note that a CDS operator with higher semblance is only accepted as supremum if the numbers of contributing traces is not lower than for any other operator for the same ZO sample. This prevents e. g. very steep operators from being selected for such suprema. Semblance will generally increase with decreasing number of contributing traces which renders the semblance values incomparable and obscures the actual quality of the operator fit (Mann, 2002).

- The semblance associated with a particular CDS operator can be used as a weight factor for its contribution to the final stack section, probably in combination with a semblance threshold which allows to reduce the overall noise level. This development is not yet included in current implementation and, thus, remains as an option for further extensions.

4.4 Aperture

In data-driven stack approaches, the size of the search and stacking aperture in midpoint direction is often based on the size of the (estimated) projected first Fresnel zone (Vieth, 2001). As mentioned above, the coherence measures are sensitive to the number of contributing traces which might deteriorate the coherence analysis, thus, the aperture size has to be kept constant for a particular ZO sample. In the model-based approach, coherence analysis is not employed, such that there is no need for a fixed aperture. In addition, the aperture size in midpoint direction has to be chosen smaller than it has been applied in CRS stack method, as the CDS approximation with $R_{CDS} \equiv R_{NIP,mod}$ quickly deviates from the actual event in case of a reflection event. Therefore, I propose to use a smaller aperture centered around the so-called CRP trajectory, where CRS operator and CDS operator are both tangent to the actual event. In a second order approximation, the CRP trajectory describes the reflection response originating from a single reflection point with an inhomogeneous overburden. Its projection into the acquisition surface reads (Höcht et al., 1999)

$$x_m(h) = x_0 + r_T\left(\sqrt{\left(\frac{h}{r_T}\right)^2 + 1} - 1\right) \quad \text{with} \quad r_T = \frac{R_{NIP}}{2\sin\alpha} \tag{4.9}$$

and provides the lateral position of the center of the stacking aperture for each half-offset h. Obviously, all required properties in Equation (4.9) are readily available from the dynamic ray tracing. The projections of the CRP trajectories for $R_{NIP}=1000m$ and for the emergence angles ±50° @ 2° spacing are shown in Figure 4.4.

Along the CRP trajectory, I can use comparatively small midpoint apertures and still ensure that I capture the contributions from the area of tangency between event and operator. With the width of the aperture, I can further control to some extent whether diffraction events should be preferred against reflections events, as the CDS operator (3.16) fits diffraction events in a larger area of tangency.

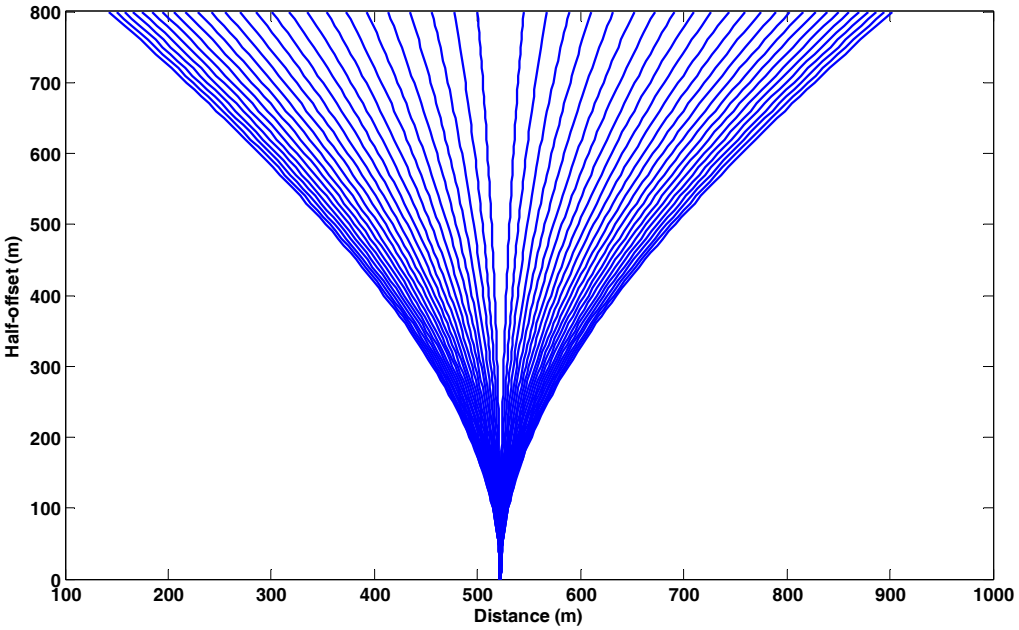

Figure 4.4: The projections of CRP trajectories for one emergence angle location and different emergence angles.

Chapter 5

Synthetic and real data example

To allow for a direct comparison with the CRS result by Mann (2002) and the data-driven CDS results by Soleimani (2009) I applied the model-based CDS approach to the well-known synthetic Sigsbee2A data set (Pfaffenholz, 2001) and a real land data set. The results of the CRS process are three optimized kinematic wave field attributes, a coherence section, and an optimized stack section. Since the CRS process is performed in three steps, the intermediate result, like CMP coherence section, automated CMP stack section etc., are in hand. However, there is no interest to consider these results in the context of this thesis.

The processing of the prestack data set with the model-based CDS stack yields a stack section, a section of the highest encountered semblance, a section with the corresponding emergence angle α, and a section with the corresponding radius of curvature R_{CDS}. In contrast, for the data-driven CDS stack, only the stack section is available. In the following I will compare the results of these different approaches.

5.1 Synthetic example: Sigsbee 2A data

The so-called Sigsbee 2A data set has been simulated by the *Subsalt Multiples Attenuation and Reduction Technologies* (SMAART) oil industry joint venture by acoustic finite-difference (FD) method for the stratigraphic model shown in Figure 5.1. This data set is a sample of a 2-D marine seismic data acquisition that mimics the observed geology in the Gulf of Mexico that contains a stratified back ground with a relatively smooth macro-velocity model. The model also contains a salt body with a quite complicate geometry and a group of diffraction points on a regular grid that implemented by means of higher velocity points in the model.

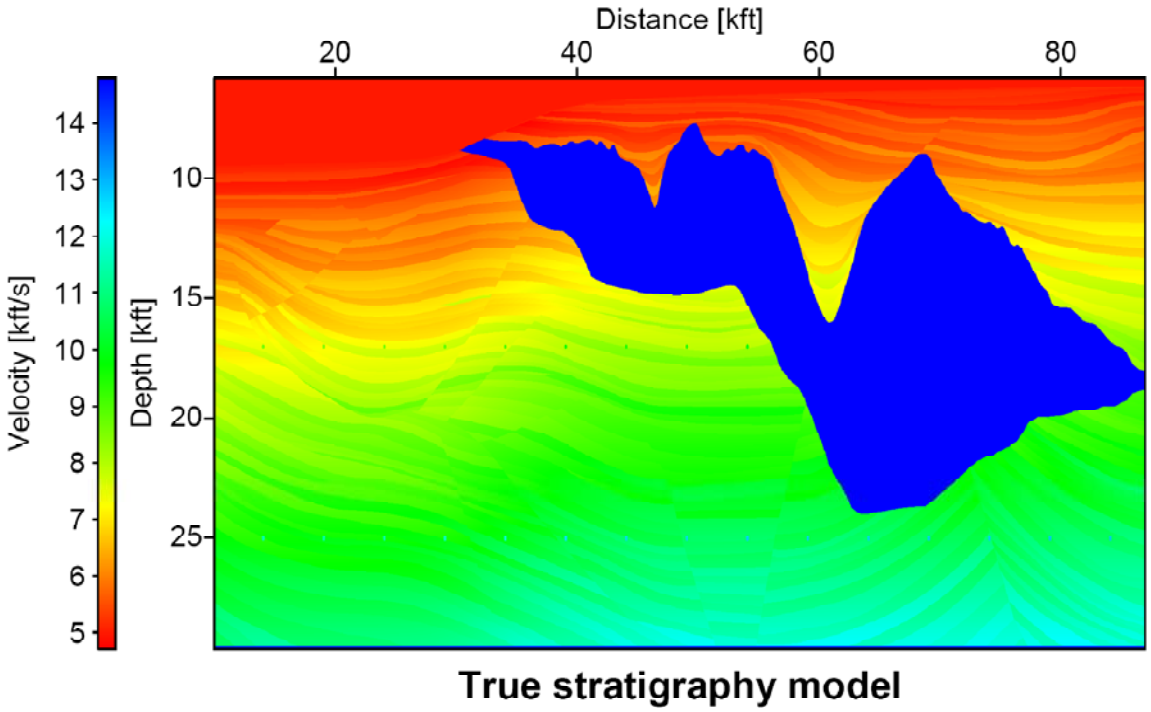

Figure 5.1: Stratigraphic model used for the simulation of the Sigsbee 2A data.

I did not change the geometry of data which is given in Imperial Unit to allow for an easier comparison with the other results obtained for these data. Due to an absorbing top surface, the data contain no free-surface multiples. Sources and receivers are located 25ft below the sea surface and the measured quantity is pressure. All obtained results are related to the datum of source and receiver locations. All relevant acquisition parameter are shown in Table 5.1. As depicted in Figure 5.2 not all shot gathers contain 348 traces, although the acquisition parameters offer a quite regular acquisition geometry.

Shot and receiver geometry	
Number of shots	500
Shot interval	150ft
Number of receivers	348
Receiver interval	75ft

Midpoint and offset geometry	
Number of CMP bins	2053
Maximum CMP fold	87
CMP bin interval	37.5ft
Offset range	0…26025ft

Recording parameters	
Recording time	12s
Sampling interval	8ms

Frequency content	
Dominant frequency	20Hz
Maximum frequency	40Hz

Table 5.1: Acquisition parameters of the prestack data set. The first receiver in each shot gather always coincides with the corresponding shot (Mann, 2002).

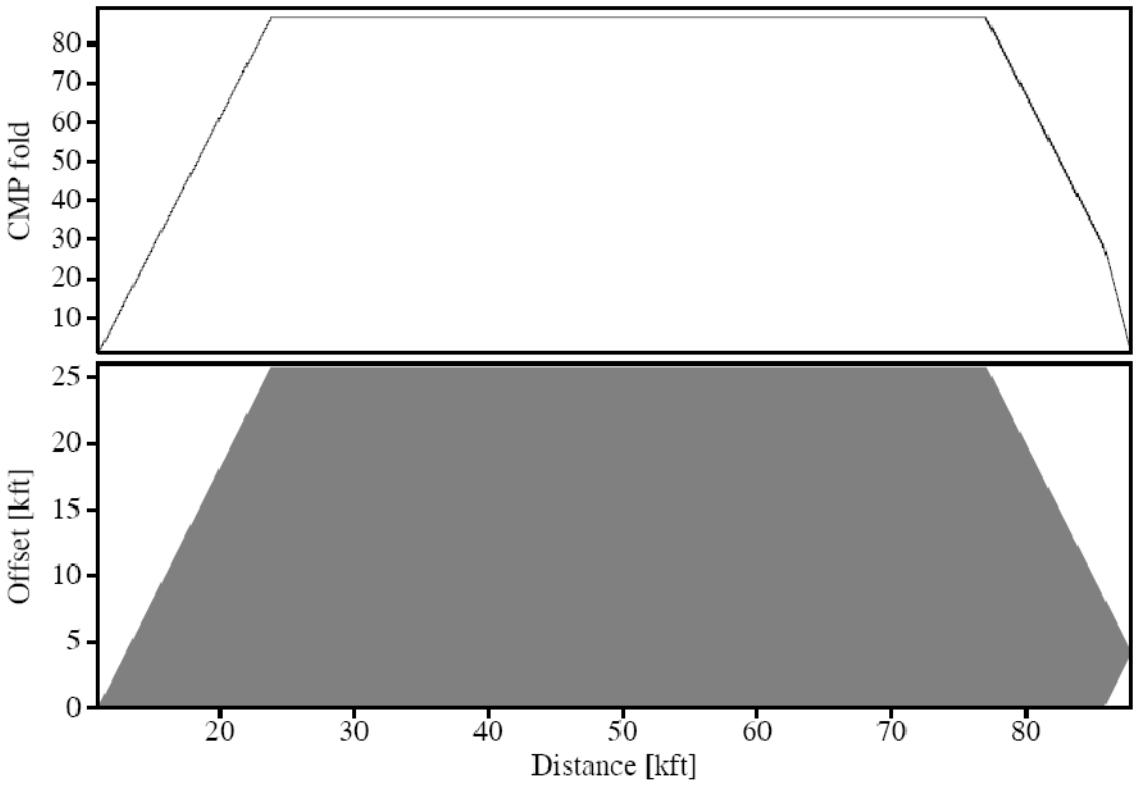

Figure 5.2: CMP fold and area covered with prestack data. The shot gathers on the right-hand side do not contain all 348 receivers. In usual marine acquisition, the number of receivers is constant (Mann, 2002).

According to Figure 5.1, the salt body has a strongly curved surface. The syncline segments in top of the salt produce the well-known bow-tie structures in the ZO section. Obviously, a bow-tie shape in ZO section will be resolved by a migration process. However this strange bow-tie shape with a multitude strange event in its vicinity is present through all proceeding steps. Mann (2002) showed that these strange events are related to prismatic waves generated by multiple reflection of the waves in the syncline structures, see Figure 5.3. However, the CRS stack method assumes primary events associated with central ZO rays with normal incidence on the reflector, only. This assumption is strongly violated in this situation, thus it is not possible to obtain a reasonable image of the syncline structures and anything beneath it (Mann, 2002).

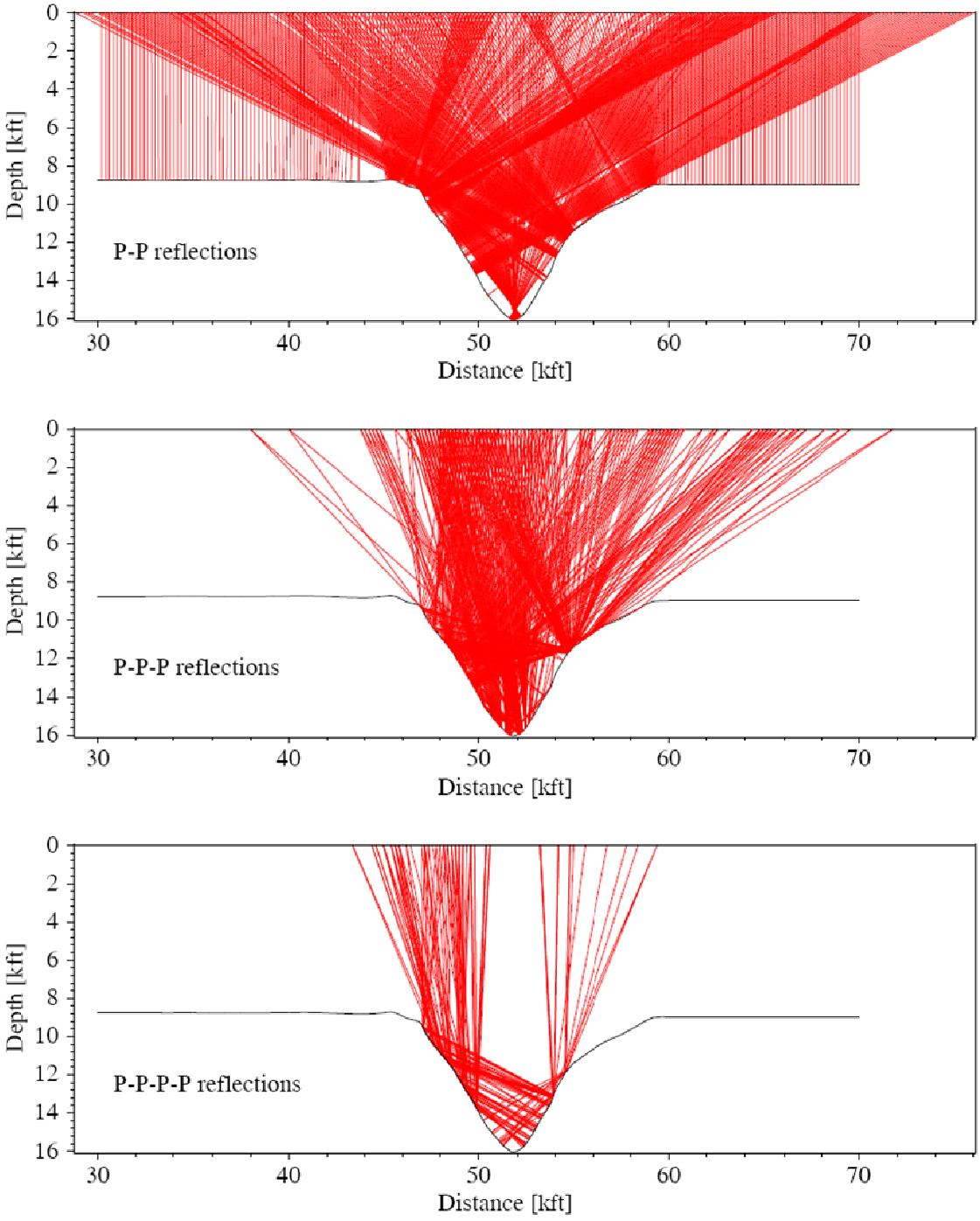

Figure 5.3: A simple model consisting of two homogeneous layers. The syncline structure mimics a feature of the salt top. The red lines represent unconverted ZO rays reflected at the interface once (top), twice (middle), and three times (bottom), respectively (Mann, 2002).

Mann (2002) extracted a near offset section which has been built up from four CO sections with the smallest offsets, in order to get first impression of the data, see Figure

5.4. According to the acquisition parameters mentioned in table 5.1 the offset of these four traces are 0, 75, 150, and 225ft, respectively. Note that no NMO correction has been applied on this section. This section includes 2000 traces ranging from CMP bin number 25 to 2024. In the following I will restrict the traveltime range from 2 to 9 s as above this area, there is only the water column and below this area due to the lack of data for large offsets the ZO simulation fails in the prestack data. Actually, Figure 5.4, represents a reference result for any ZO simulation method applied to these data. As can be seen in Figure 5.4 the complicated geometry of the salt body causes numerous diffraction patterns and bow-tie structures without any similarity to the real geological structures. To resolve the diffraction patterns and bow-tie structures to some extent, Mann (2002) applied an NMO correction to the near-offset section followed by a constant velocity Stolt time migration (Stolt, 1978) because no velocity model was available at that time. The result of this processing sequence shown in Figure 5.5 is consistent with the true model illustrated in Figure 5.1. Several structural features of the subsurface model can be identified in this time-migrated section, e. g., the top of the salt body and at the side edges of the salt body also its lower boundary. In the stratified areas on the left, some faults can be observed.

The processing of the prestack data set for the Sigsbee 2A model with the CRS stack approach lead to total number of 62 sections. Although all these sections carry useful information I will not show all these sections for two reasons: first, showing up all these sections will blow the thesis up and the second, some of these section are not inherently generated by the data-driven and model-based CDS stack method as they use a different search strategy. I will focus on the final results and the most important intermediate results in the following. The benefits of the complete handling of conflicting dip situations are best seen after a subsequent migration. Fortunately, at this stage the macro-velocity model of Sigsbee 2A is at hand. Hence, I have generated a Green's function table (GFT) using an eikonal solver. Afterwards I obtained the poststack depth migration of the relevant stacked sections. Finally, I have applied a Kirchhoff prestack depth migration using the same macro-velocity model to generate a final reference. These processes have been done by applying Uni3D program which uses a

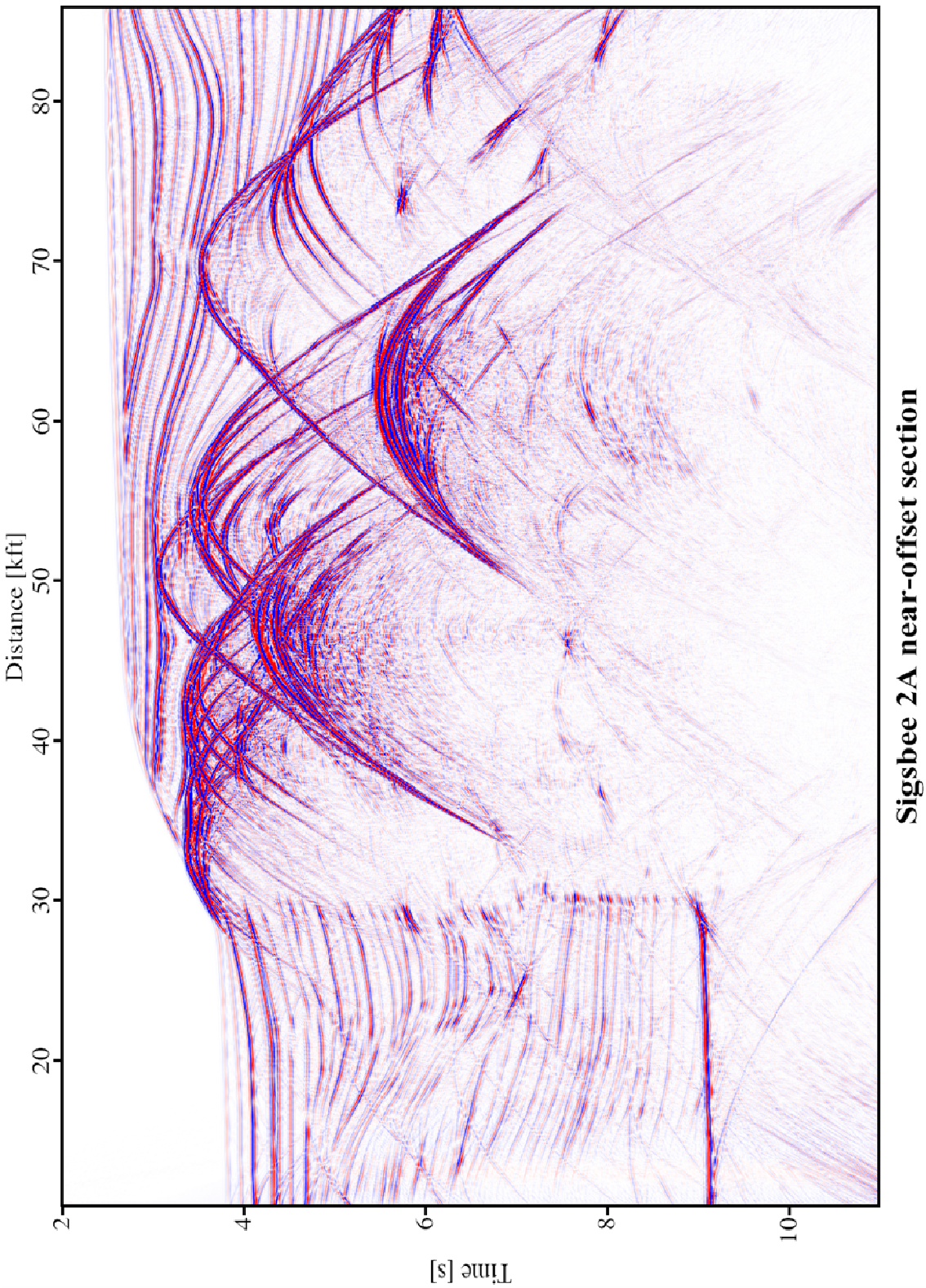

Figure 5.4: Near-offset section extracted from the prestack data. The offsets vary between 0 and 225 ft on neighboring traces. The image of the salt body is dominated by bow-tie structures and diffraction patterns (Mann, 2002).

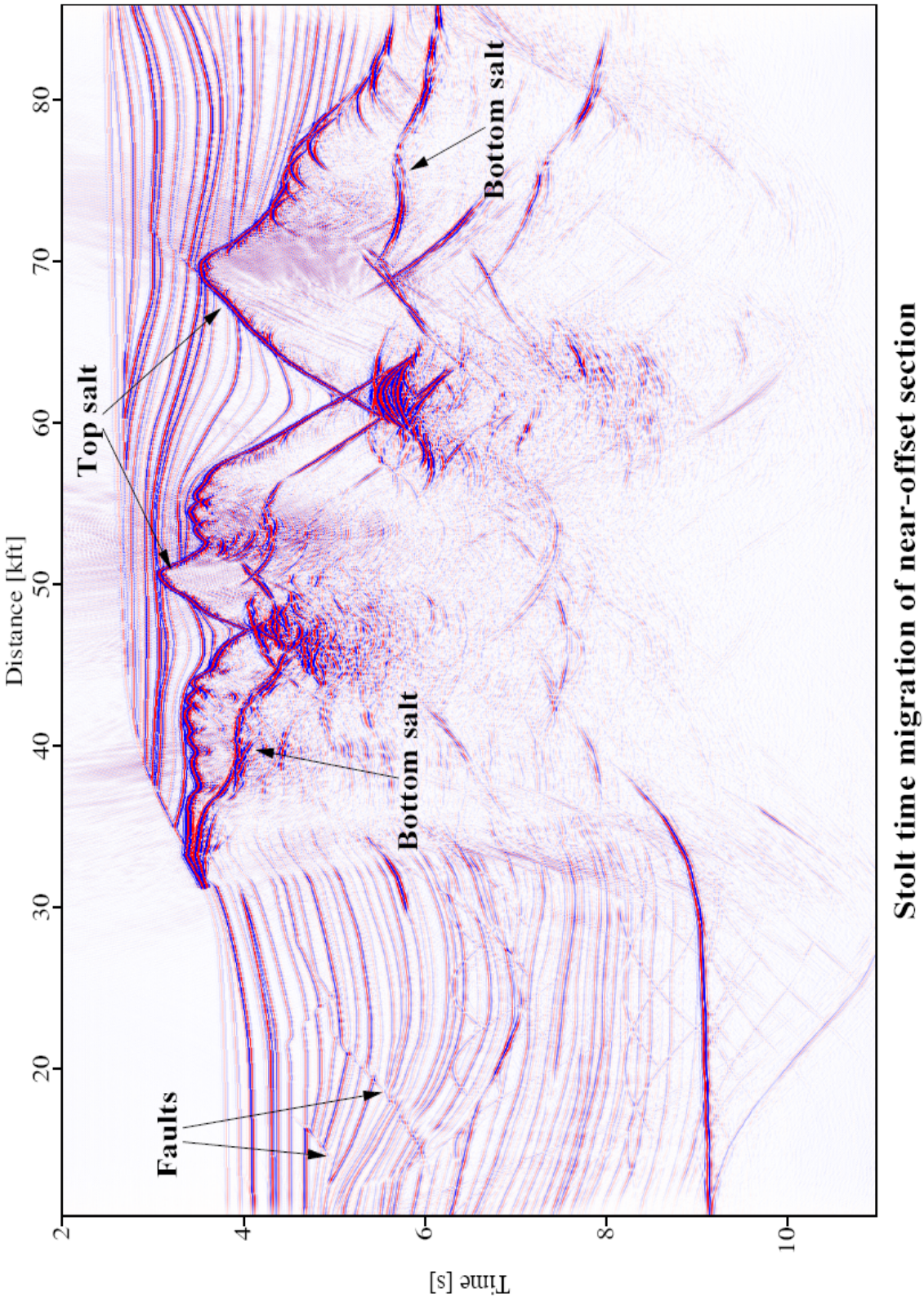

Figure 5.5: Constant velocity Stolt time migration of the NMO corrected near-offset section. Water velocity (4920 ft/s) was used for the NMO correction and the migration (Mann, 2002).

Kirchhoff true-amplitude migration algorithm. This program was developed at the University of Karlsrule (Hertweck, 2000). As the migration process is not the subject of my thesis, I refer to Yilmaz (2001) for that a general overview of migration methods.

5.1.1 CRS results for the Sigsbee 2A data

The Sigsbee 2A data set has been used by several authors to test their new idea. Mann (2002) applied the pragmatic and extended CRS search strategies to these data for the first time. To evaluate the new model-based CDS stack, I revisited the results of the extended search strategy presented by Mann (2002). The CRS stack procedure starts with an automatic CMP stack. The stacked section obtained from this step serves as input for the next steps, the linear and hyperbolic ZO stacks. These steps provide the emergence angle α and the radius of emerging normal wavefront. With the emergence angle and the stacking velocity section obtained from the automatic CMP stack, the radius of the normal incidence point wavefront R_{NIP} could be calculated. So far, all three wavefield attributes are available. They are called initial attributes as they serve as an input for optional optimization step. The final step is the optional local optimization that uses the initial wavefield attributes to perform stack and coherence analysis along the entire spatial CRS stacking operators. The basic processing parameters are collected in Table 5.2 and the computational time that was needed for processing of each step is given in Table 5.3. Obviously this computation time strongly depend on the used hardware operating system, compiler, and the implementation of the CRS stack itself.

The results shown here are the optimized section of the emergence angle, the radius of the NIP-wave ($R_{NIP,data}$), and the coherence, and as well as the stacked section. In the extended search strategy, the coherence and attribute values are separately available for each contributing event in case of conflicting dip situations. In the following I only refer to the sections associated with the most dominant events.

The optimized emergence angles shown in Figure 5.6. On the left hand side of this section the strong horizontal reflections events obscure the diffraction events and only some part of the diffractions can be observed. On the right part there are also strong diffraction events which intersect each other and obscure the horizontal weak reflectors. These conflicting dip situations arise as only the most prominent event contributes to simulate a ZO sample.

Context	Processing parameter	Setting
General parameters	Dominant frequency	20 Hz
	Coherence measure	Semblance
	Data used for coherence analysis	Original traces
	Temporal width of coherence band	56 ms
Velocity and constrains	Near surface velocity	4920 ft/s
	Tested stacking velocities	4500…20000 ft/s
Target zone	Simulated ZO traveltimes	2…11s
	Simulated temporal sampling interval	8ms
	Number of simulated ZO traces	2053
	Spacing of simulated ZO traces	37.5 ft
Aperture and taper	Minimum ZO aperture	1700 ft @ 2 s
	Maximum ZO aperture	5830 ft @ 11 s
	Minimum CMP aperture	6000 ft @ 2.3 s
	Maximum CMP aperture	25000 ft @ 11 s
	Relative taper size	30%
Automatic CMP stack	Initial moveout increment for largest offset	16 ms
	Number of refinement iterations	3
Liner ZO stack	Tested emergence angles	-60…60°
	Initial emergence angle increment	1°
	Number of refinement iterations	3
Hyperbolic ZO stack	Initial moveout increment for largest ZO distance	8ms
	Number of refinement iterations	3
Hyperbolic CS/CR stack	Initial moveout increment for largest offset	8ms
	Number of refinement iterations	3
Conflicting dip handling	Maximum number of dips	3
	Absolute coherence threshold for global maximum	0.05
	Relative coherence threshold for local maxima	0.25
Local optimization	Coherence threshold for smallest traveltime	0.5
	Coherence threshold for largest traveltime	0.02
	Maximum number of iterations	100
	Maximum relative deviation to stop	10^{-4}
	Initial variation of emergence angles	6°
	Initial variation of R_{NIP}	5%
	Initial variation of transformed R_N	6°
	Transformation radius for R_N	350ft

Table 5.2: processing parameters used for the ZO simulation by means of the CRS stack (Mann, 2002).

Processing step	absolute CPU time [h]	relative CPU time [%]
Automatic CMP stack	25	0.6
Zero-offset stacks	65.5	15.2
Initial stack	26.7	6.2
Local optimization	335.8	78.0
Total	430.5	100.0

Table 5.3: absolute and relative CPU times required for the successive processing steps. All times refer to a 400 MHz Pentium II processor and the processing parameters compiled in Table 5.2 (Mann, 2002).

The values of the radius of curvature of the NIP-wavefront are shown in Figure 5.7 for the dominant events. As expected, R_{NIP} increases continuously with increasing the traveltime which is seen in stratified areas above and left to the salt body. Below the salt, the section is dominated by the tails of bow-tie structures and diffraction patterns stemming from the top and possibly also from the bottom of the salt body. There are only few indications of events related to reflectors actually located below the salt. As I mentioned in the previous chapter the radius of curvature of the NIP-wavefront $R_{NIP,data}$, which is calculated from the prestack data set in the CRS stack approach, does not exactly coincide with the forward-modeled $R_{NIP,mod}$. Nevertheless, for the sake of comparison I have presented this section here.

The coherence section for the dominant events is shown in Figure 5.8. This section allows to identify the detected events and to estimate the reliability of the image as well of its associated wavefield attributes. In the left part of this section the strong reflections show a dominant coherence and, thus, obscure the weak diffraction events. In contrast, in the right part, above the salt body in the absence of any diffraction events, the continuity of the horizontal reflector has been preserved. In some parts of this section the semblance value reaches 1. Obviously this occurs because of very low background noise of the data set which does not happen during process of real data set.

The result of CRS stacked section obtained from optimized attributes shown in Figure 5.9. The stacking process is limited to the projected first Fresnel zone determined from the wavefield attributes (see e.g. Vieth, 2001). This section is very similar to the reference section Figure in 5.4. At the left and above the salt body the horizontal

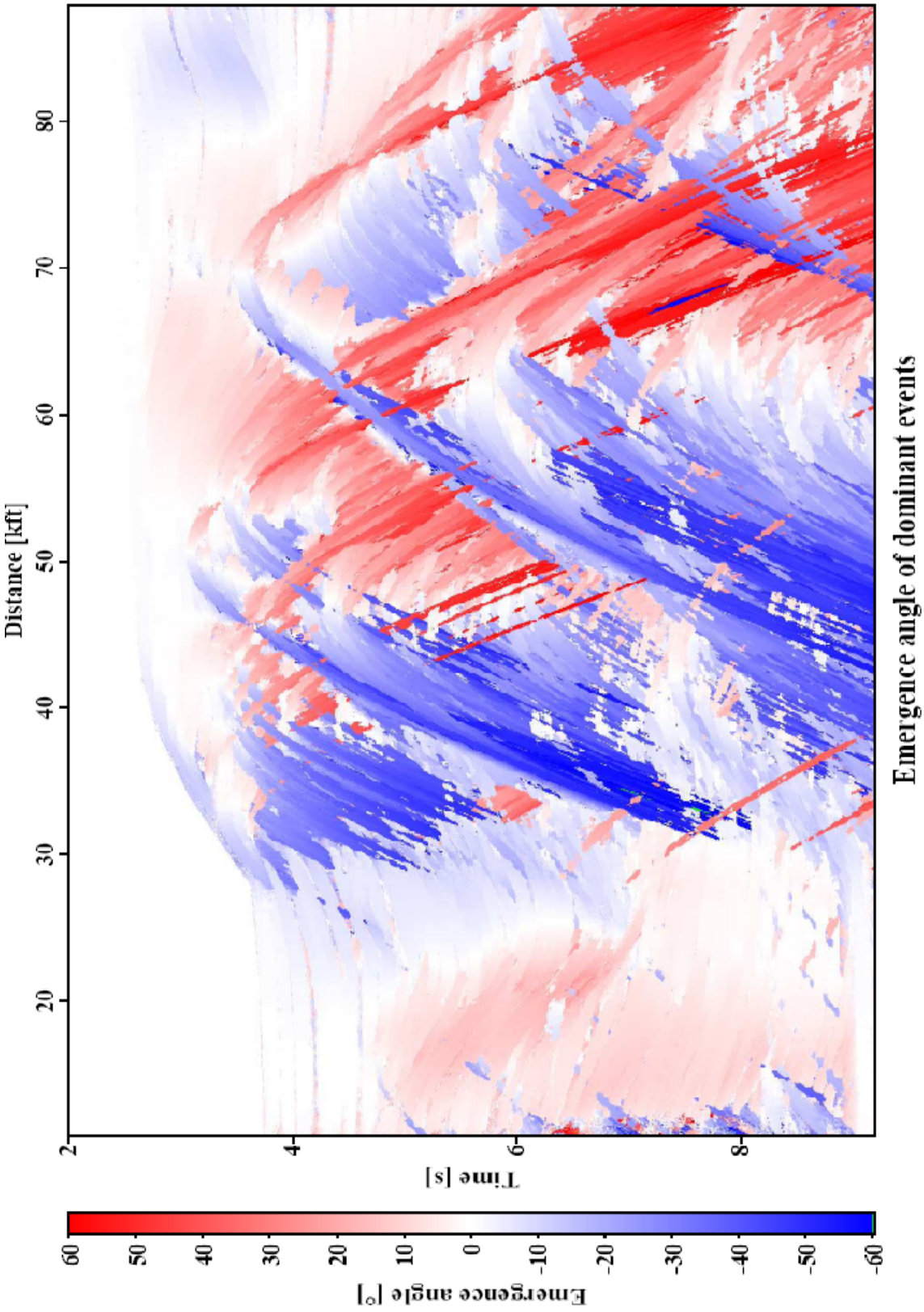

Figure 5.6: Emergence angle section for the dominant events. The emergence angle is directly related to the slopes of the events (after Mann, 2002).

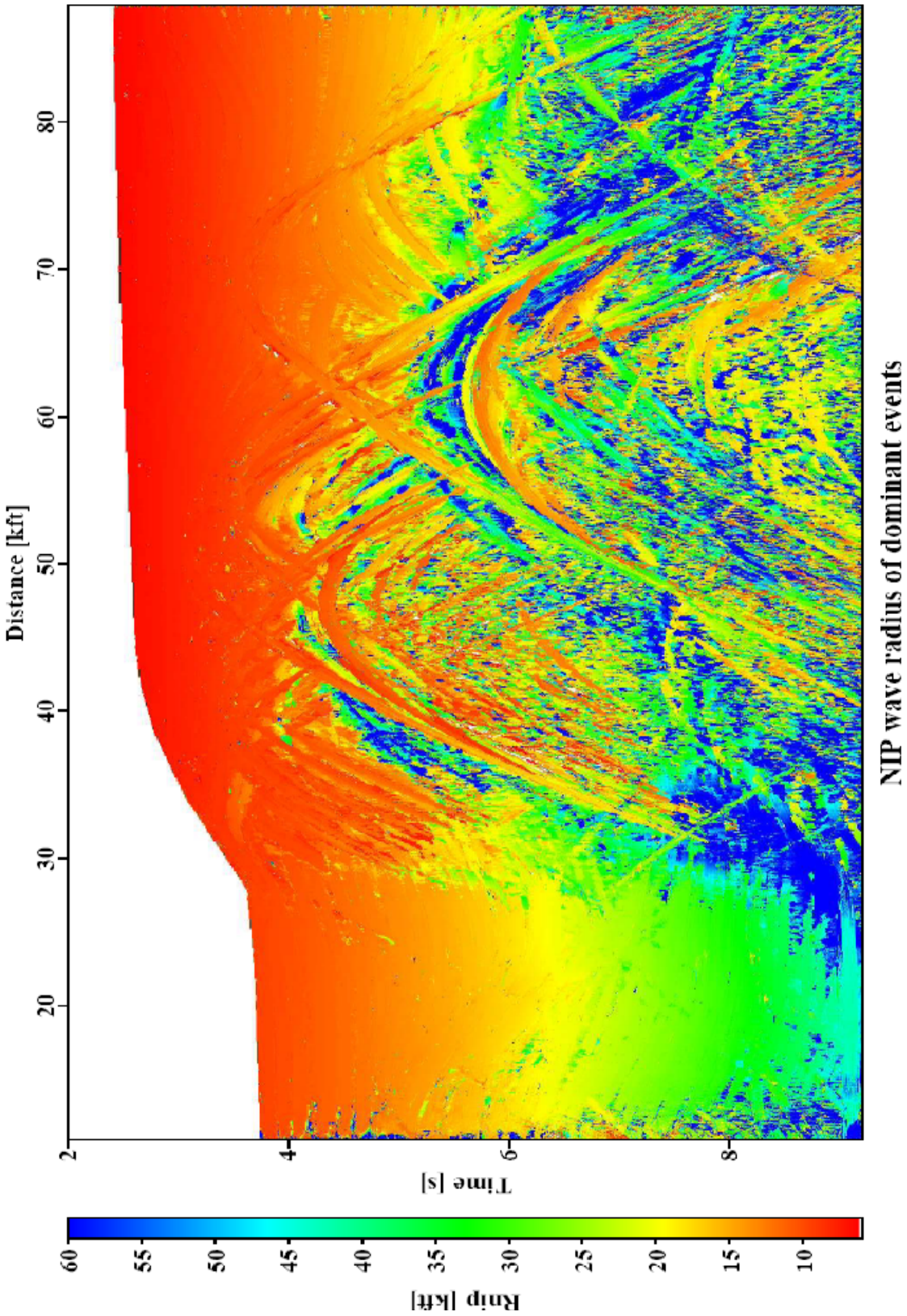

Figure 5.7: Section with the radius of curvature of the NIP wavefront for the dominant events (after Mann, 2002).

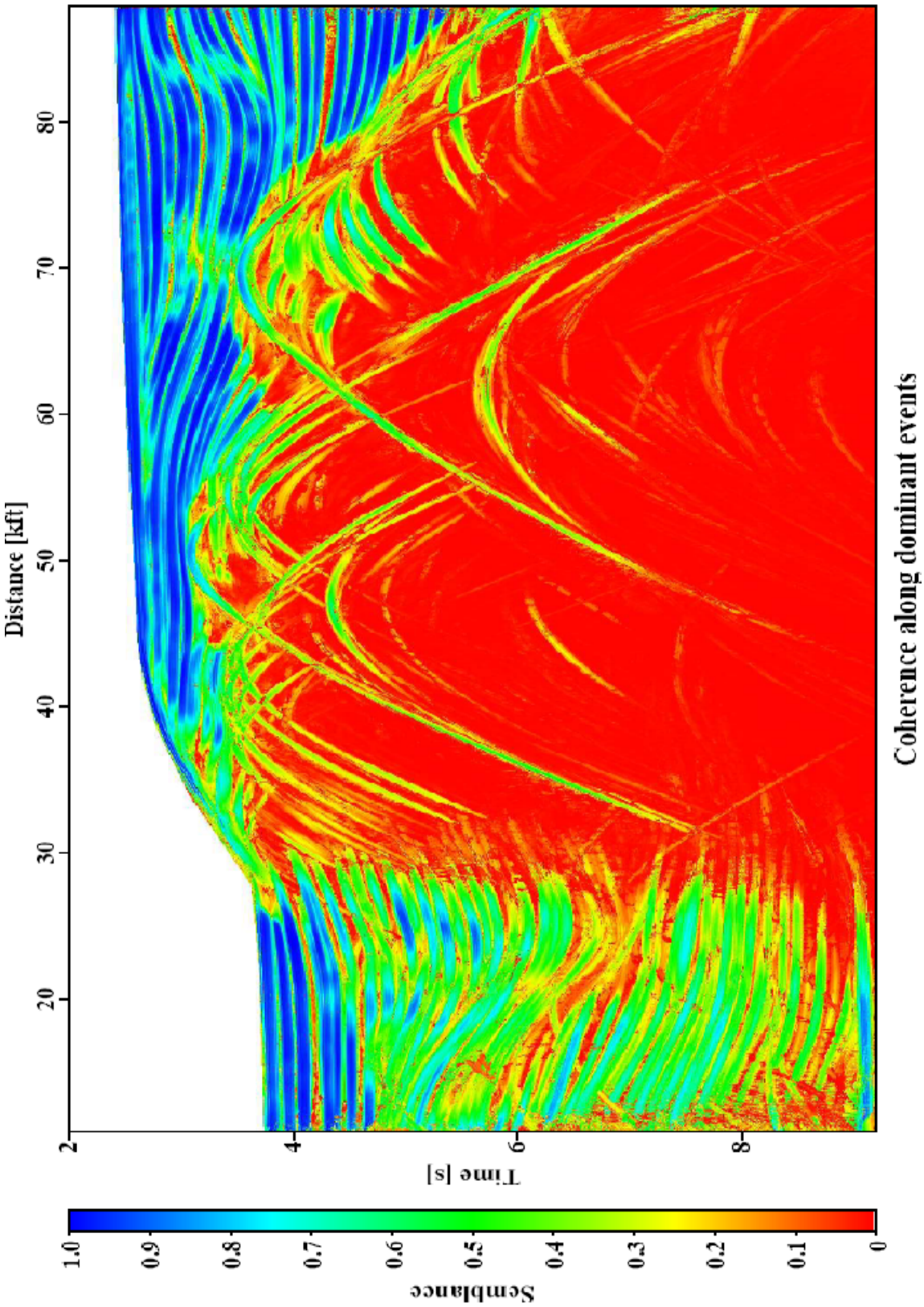

Figure 5.8: Coherence section for the dominant events associated with the CRS-stacked section (after Mann, 2002)

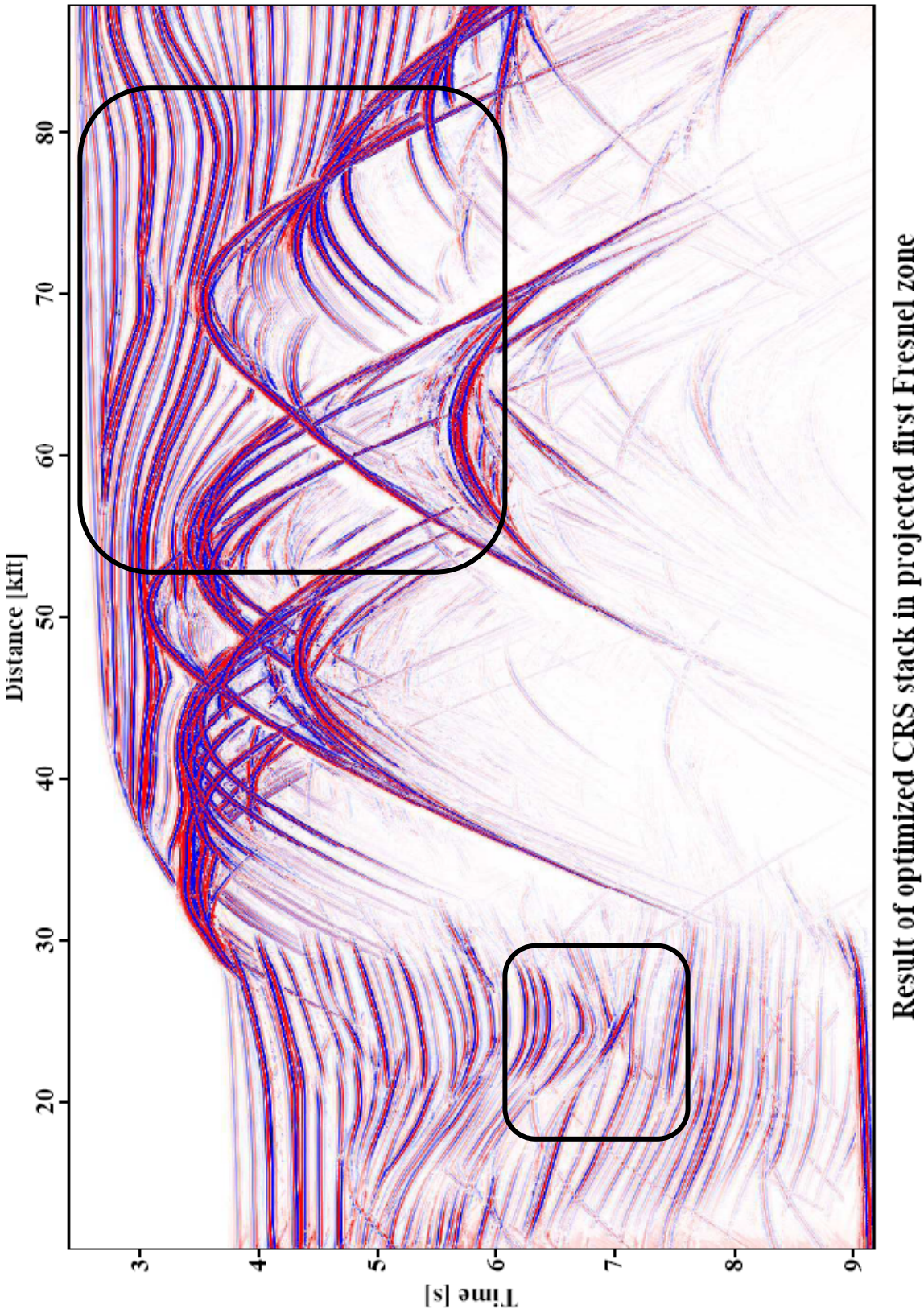

Figure 5.9: Result of the optimized CRS stack restricted to the projected first Fresnel zone (after Mann, 2002).

reflectors are well imaged. The diffraction curves which originate from the top salt as well as the bow-tie are well simulated. Nevertheless these results suffer from some inherent problems discussed before. The subsections are shown by square in Figure 5.9 will use to zoom in to the different stacking approach.

As mentioned above, the benefits of handling the problem of conflicting dip become evident after the migration, hence I have computed the poststack depth migration of the stacked result obtained from extended search strategy shown in Figure 5.10. As can be seen the faults and diffractors are only partly focused. Spurious events in the stacked section, e. g. associated with a change of the number of contributions from sample to sample, cause various artifacts showing up as isochrones in the migrated section. The result based on the CRS stack with only one dip (not displayed) differs from the multi-dip CRS-stacked section in two respects: on the one hand, due to the lacking contributions at conflicting dip locations, the diffractors and faults appear even less focused and with lower amplitudes. On the other hand, the stacked section contains less spurious events such that there are fewer artifacts in the migrated section. In both cases, the results of poststack migration are unsatisfactory. The synclines in the top salt are incomplete and accompanied by coherent artifacts at slightly larger depths. As discussed by Mann (2002), the CRS stack has most likely also parameterized and stacked events associated with prismatic waves which lead to additional events in the stacked section.

5.1.2 Data-driven CDS results for the Sigsbee 2A data

For the next comparison I revisited the data-driven CDS stack result by Soleimani (2009). Due to performance reasons the left and the right part of data have been processed separately. Later on, these two parts were merged to form a unique section. In addition, the lower right part of the stack section has not been processed as there are not considerable events and to reduce the computation time. The result of the data-driven CDS stack approach is shown in Figure 5.11. Compared to the result of the CRS stack shown in Figure 5.9 the diffraction curves are well imaged. In the left part the diffraction curves formerly partly or fully obscured by strong reflections are now clearly imaged by data-driven CDS procedure. The parameters used for data-driven CDS stack processing and the computation times are shown in table 5.4.

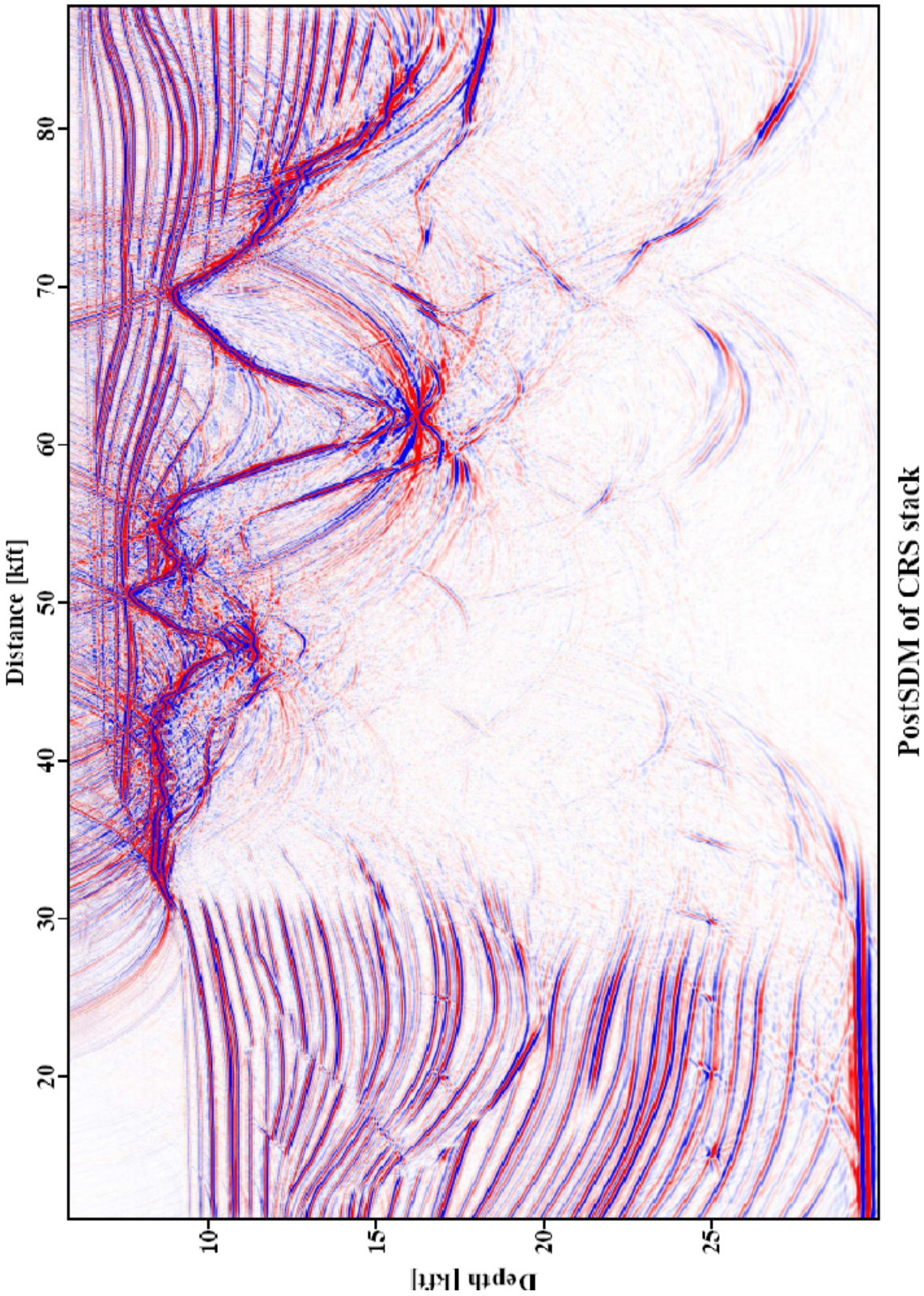

Figure 5.10: Poststack Kirchhoff depth migration result for the CRS stack result published by Mann (2002). Faults and diffractors are only partly focused; many isochrones caused by spurious events can be seen.

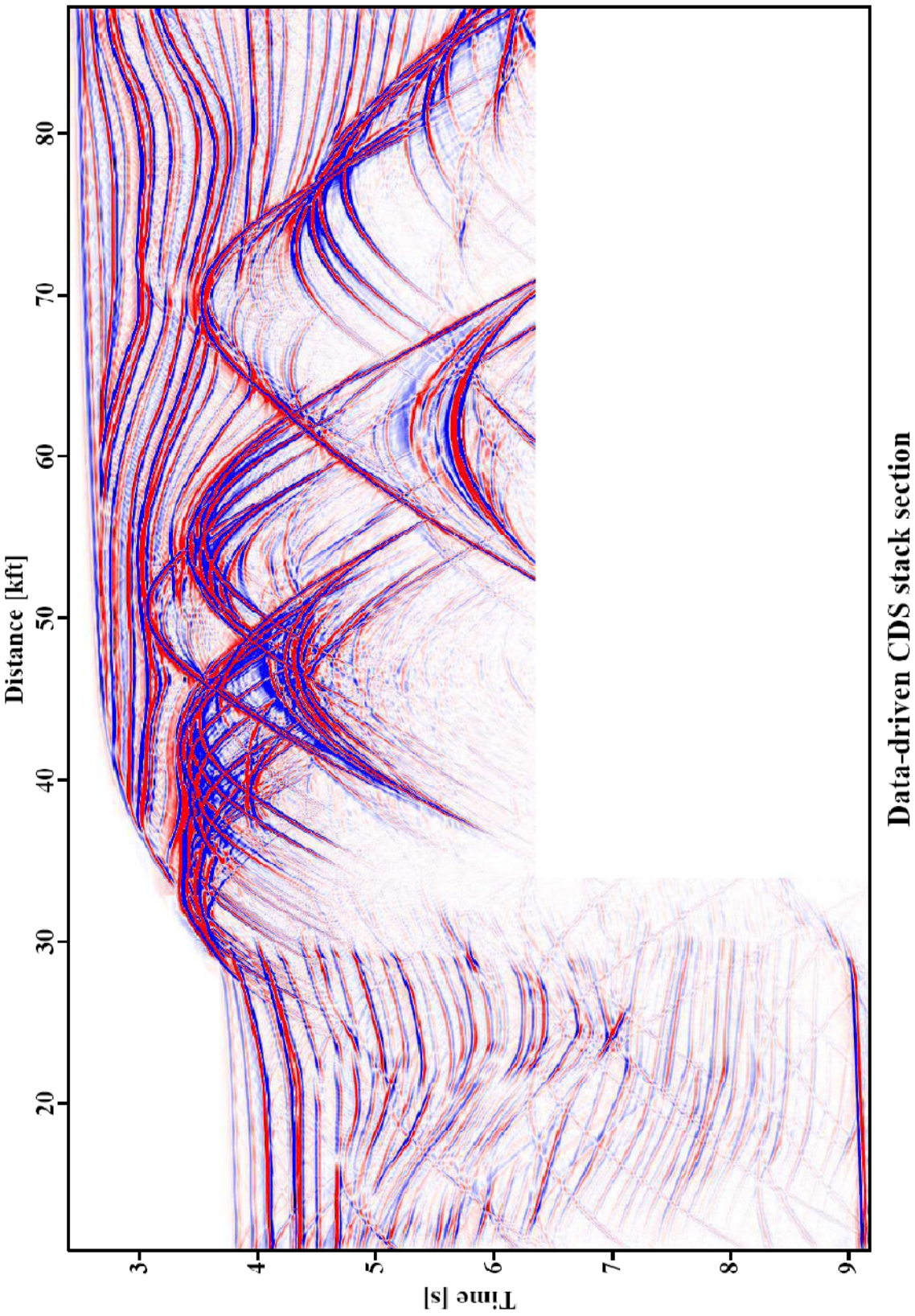

Figure 5.11: Stacked section obtained with the data-driven CDS approach (after Soleimani, 2009).

Context	Processing parameter	Setting
General parameters	Dominant frequency	20 Hz
	Coherence measure	Semblance
	Data used for coherence analysis	Original traces
	Temporal width of coherence band	56 ms
Velocity and constrains	Near surface velocity	4920 ft/s
	Tested stacking velocities	4500…20000 ft/s
Target zone	Simulated ZO traveltimes for left part	2…9s
	Simulated ZO traveltimes for top part	2…6.2
	Simulated temporal sampling interval	8ms
	Number of simulated ZO traces	2053
	Spacing of simulated ZO traces	37.5 ft
Aperture and taper	Minimum ZO aperture in left part	1700 ft @ 2 s
	Maximum ZO aperture in left part	10000 ft @ 9 s
	Minimum ZO aperture in top part	1700 ft @ 2 s
	Maximum ZO aperture in top part	10000 ft @ 6 s
	Minimum CMP aperture in left part	6000 ft @ 2.3 s
	Maximum CMP aperture in left part	25000 ft @ 9 s
	Minimum CMP aperture in top part	6000 ft @ 2.3 s
	Maximum CMP aperture in top part	25000 ft @ 6 s
	Relative taper size	30%
Data-driven CDS parameter	Tested emergence angle	±40°
	Initial emergence angle increment	1°
	CS search moveout sampling rate	2ms
	Processing time for left part	365.203 hours
	Processing time for top part	229.376 hours
Hardware	CPU	Intel, Pentium 4, 2.6GHz
	RAM	1GB
	Compiler	GNU 4.1.2
	OS	SuSE Linux 10.2

Table 5.4: Processing parameters used for the ZO simulation of the Sigsbee 2A data set by means of data-driven CDS stack method (after Soleimani, 2009).

The corresponding poststack migrated section displayed in Figure 5.12 shows well focused diffractors and faults and much less artifacts caused by spurious events compared to the CRS-based migrated result in Figure 5.10. In the CRS-based result, the synclines in the top of salt are still not properly imaged, as the data-driven CDS stack picks up prismatic waves as well. However, as mentioned in Table 5.4 the total computation time for the stacking processing is 600 hour or close to 25 days which is far too long.

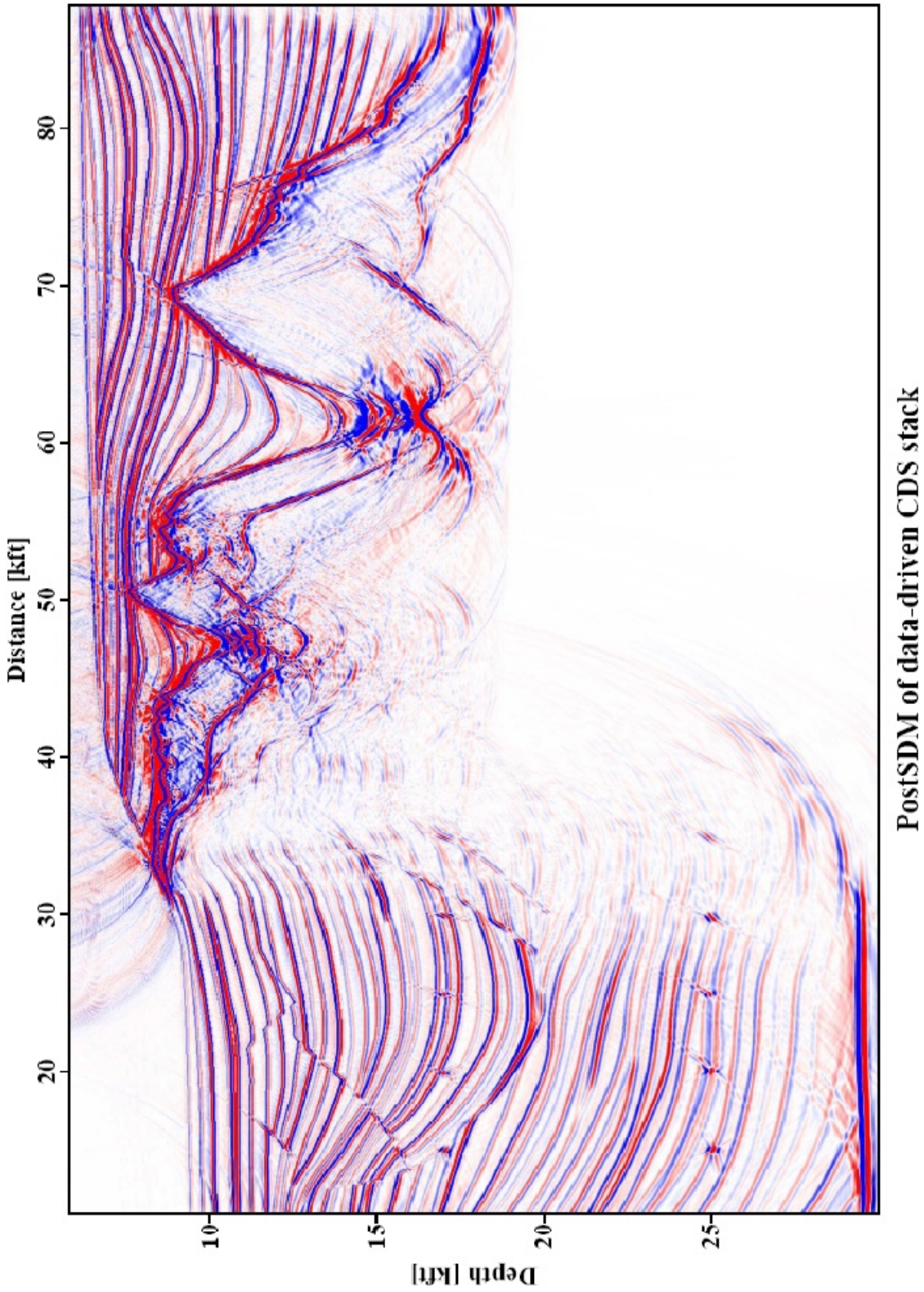

Figure 5.12: Poststack Kirchhoff depth migration result for the data-driven CDS result published by Soleimani (2009). Faults and diffractors are well focused, there are only few isochrones caused by spurious events.

5.1.3 Model-based CDS stack results for the Sigsbee 2A data

As I want to focus on the stacking procedure rather than on the generation of the macro-velocity model by means of an inversion, I used the migration velocity model shown in Figure 5.13 distributed with the data as basis for the macro-velocity model.

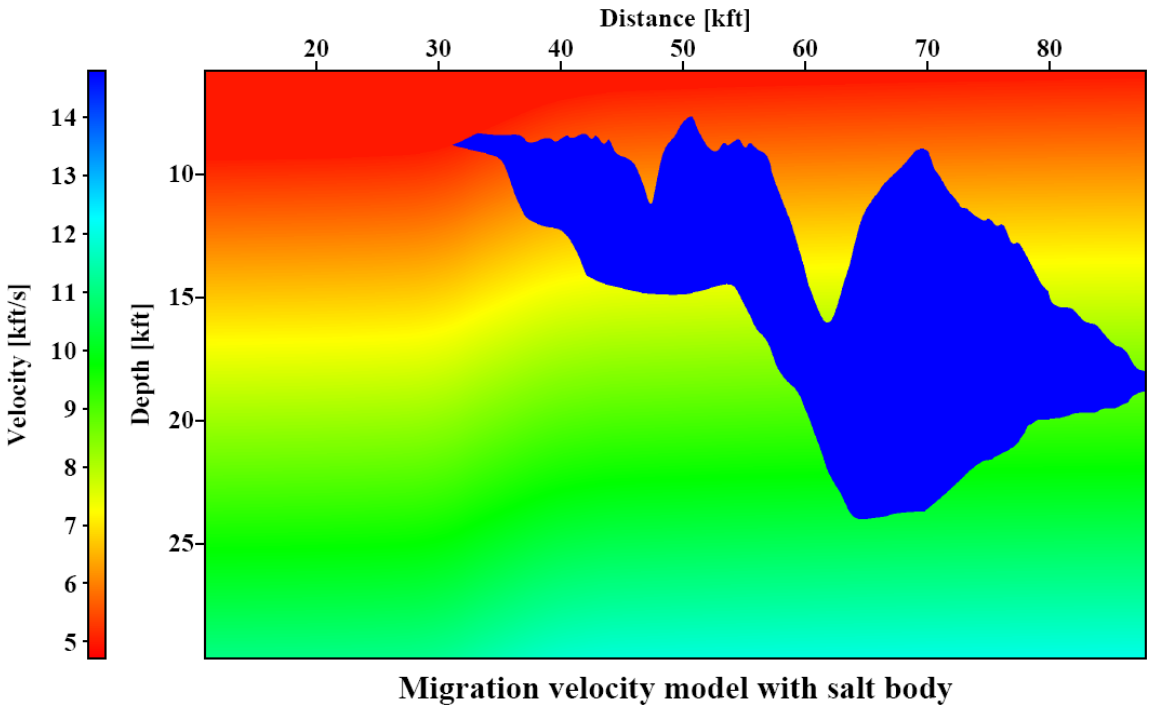

Figure 5.13: The migration velocity model used as basis for the macro-velocity model (Pfaffenholz, 2001).

Due to the homogeneous water layer, the assumption of a virtually constant near-surface velocity in Equations (3.11) and (3.16) is fully satisfied. The migration velocity model consists of the water column, the salt body, and a smooth background velocity, namely a constant vertical gradient. To obtain the macro model for ray tracing, I first restored the seafloor at those locations where the salt body is in direct contact with the water column and then replaced the salt body by the background gradient. Finally, I smoothed the slowness in the velocity model five times with the auto-convolution of a rectangular box of 525 × 525 ft^2 to get rid of the sharp velocity contrast at the seafloor without impairing the kinematics of the model. In addition, I padded the model in lateral direction to allow for rays close to the margin of the model, see Figure 5.14.

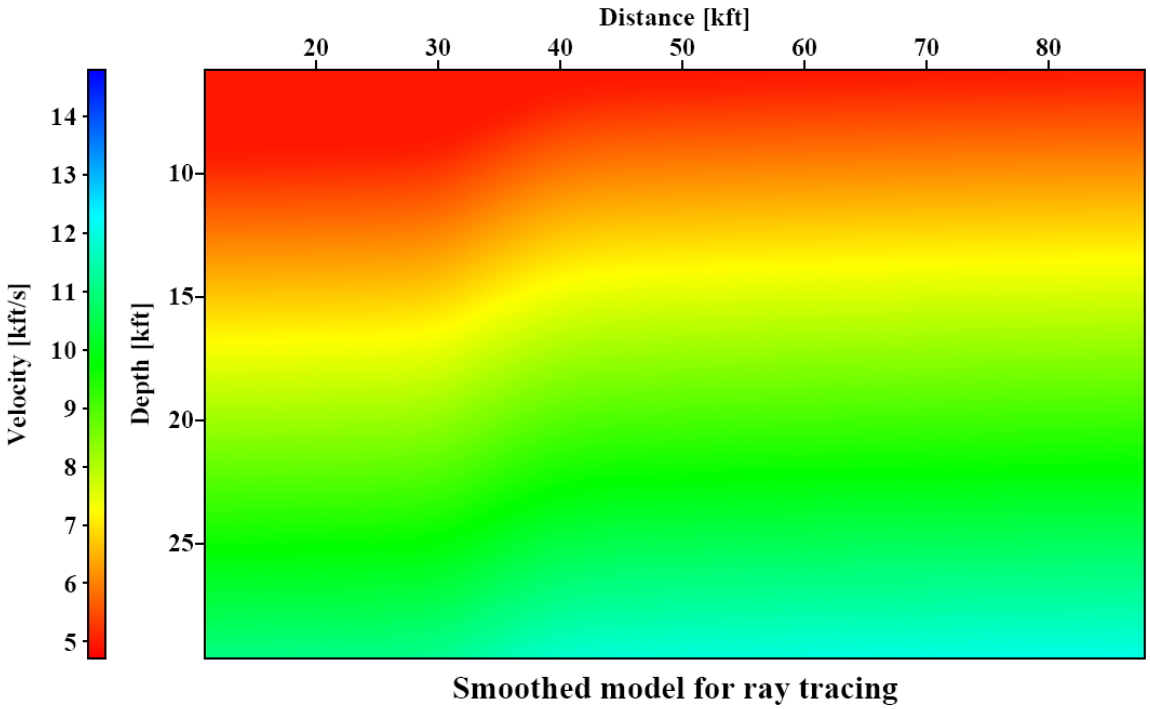

Figure 5.14: The smoothed macro-velocity model prepared for ray tracing.

The kinematic and dynamic ray tracing has been performed for each CMP bin, i. e., with a lateral spacing of 37.5 ft and a temporal step length of 8*ms*. I divide these steps into finer steps by a step factor of 10. Ray tracing is performed on this fine temporal grid whereas the data is only stored on the coarse grid. I did not allow turning rays, although this is supported by the implementation. Rays have been shot for an angle range of ±50°@2° spacing. For the actual stacking process, the stacking parameter R_{CDS} is linearly interpolated in between the rays on a grid with 1° spacing. The midpoint aperture has a constant half-width of 300ft centered around the approximate CRP trajectory, the offset aperture ranges from 6000ft at 2.3s to 25000ft at 11s ZO traveltime. Semblance has been calculated within a time window of 56ms. The parameters used for the model-based CDS stack processing and the computation times are given in table 5.5. The stacked section shown in Figure 5.15 is very similar to the corresponding result obtained with its data-driven counterpart presented by Soleimani (2009) (Figure 5.11). The latter contains some spurious events which do not show up in the model-based results, but the main difference is the computational cost which is now more than two

Context	Processing parameter	Setting
General parameter	Dominant frequency	20 Hz
	Coherence measure	Semblance
	Data used for coherence analysis	Original traces
	Temporal width of coherence band	56 ms
Target zone	Number of target traces	2053
	Number of samples per target trace	850
	Temporal target sampling	8ms
	Time offset in target traces	2.4s
	First CDP number in target zone	25
	Last CDP number in target zone	2077
Aperture and taper	Constant ZO aperture	600 ft
	Minimum CMP aperture	6000 ft @ 2.3 s
	Maximum CMP aperture	25000 ft @ 11 s
	Relative taper size	30%
Model-Based CDS parameter	Time stepping factor for ray tracing	10
	Time stepping for ray tracing	0.8ms
	First model trace corresponds to CDP	25
	Last model trace corresponds to CDP	2077
	Lateral padding to the left	30 grid points
	Lateral padding to the right	30 grid points
	Maximum emergence angle for search	50
	Minimum emergence angle for search	-50
	Emergence angle Increment for ray tracing	2°
	Emergence angle Increment for stacking	1°
	Turning rays	Disallow
	Lateral velocity model spacing	37.5ft
	Vertical velocity model spacing	25ft
	Number of lateral velocity samples	2114
	Number of vertical velocity samples	1201
	Processing time	6.8961hours
Hardware	CPU	Pentium 4, 2.6GHz
	RAM	1GB
	Compiler	GNU 4.1.2
	OS	SuSE Linux 10.2

Table 5.5: Processing parameters used for the ZO simulation of the Sigsbee 2A data set by means of model-based CDS stack method.

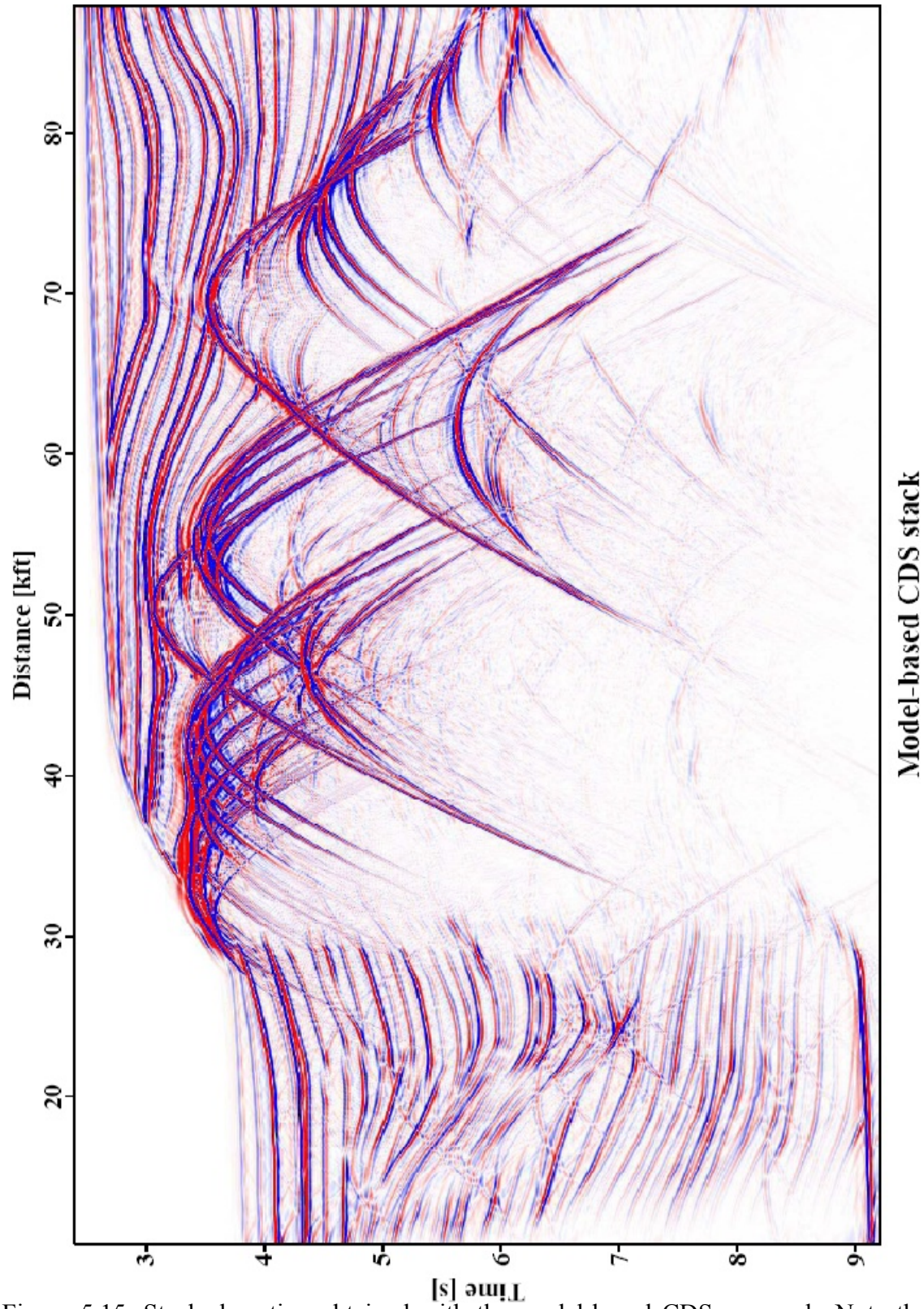

Figure 5.15: Stacked section obtained with the model-based CDS approach. Note the various diffraction patterns caused by true diffractors, wedges, and model discretization.

orders of magnitude lower for this data set (not including the fact that the data-driven result excludes the subsalt region for performance reasons). Of course, with the inherent second-order approximation of the CRS and CDS approaches, I cannot expect any reasonable result for the subsalt region. That is why I have removed the salt body in the macro-velocity model.

To considering the ability of model-based CDS stack to handle conflicting dip situations, the subsequent migration is applied using the macro-velocity model depicted in Figure 5.14. Figure 5.16 shows the result of a Kirchhoff poststack depth migration obtained for the model-based stack section shown in Figure 5.15. All faults and diffractors are well focused; everything left of and above the salt is well imaged. Note that the effect of prismatic waves above the salt body hardly occurs in the model-based result shown in Figure 5.16 since the normal rays have been explicitly forward-modeled; the events from prismatic waves are attenuated by destructive interference.

As a final reference, I also applied a Kirchhoff prestack depth migration to the prestack data using the same macro-velocity model. The offset range and the muting of the migrated images gather were chosen such that they match the corresponding parameters used during the CDS stack as closely as possible. Figure 5.17 shows the stack of about 80 offset bins with a width of 300 ft each after depth-dependent muting. The prismatic waves are again imaged wrongly, but cancel out during the stack. This section is very similar to the poststack migration of the model-based CDS-stacked results in Figure 5.16. Note that (of course, except for the subsalt part) the prestack migration has been performed with an optimum, i. e., kinematically perfectly correct velocity model. For less accurate models as usually achievable for real data, the prestack depth migration result will suffer much more from the model inaccuracy than the model-based CDS stack and the subsequent poststack migration.

As mentioned above, I can perform coherence analysis along the individual forward-calculated stacking operators in the prestack data with little additional effort. In this way, I can obtain coherence and attribute sections resembling some of the corresponding sections known from the CRS stack approach: I simply keep track of the operator yielding the highest coherence measure for an individual ZO sample. As an example, the

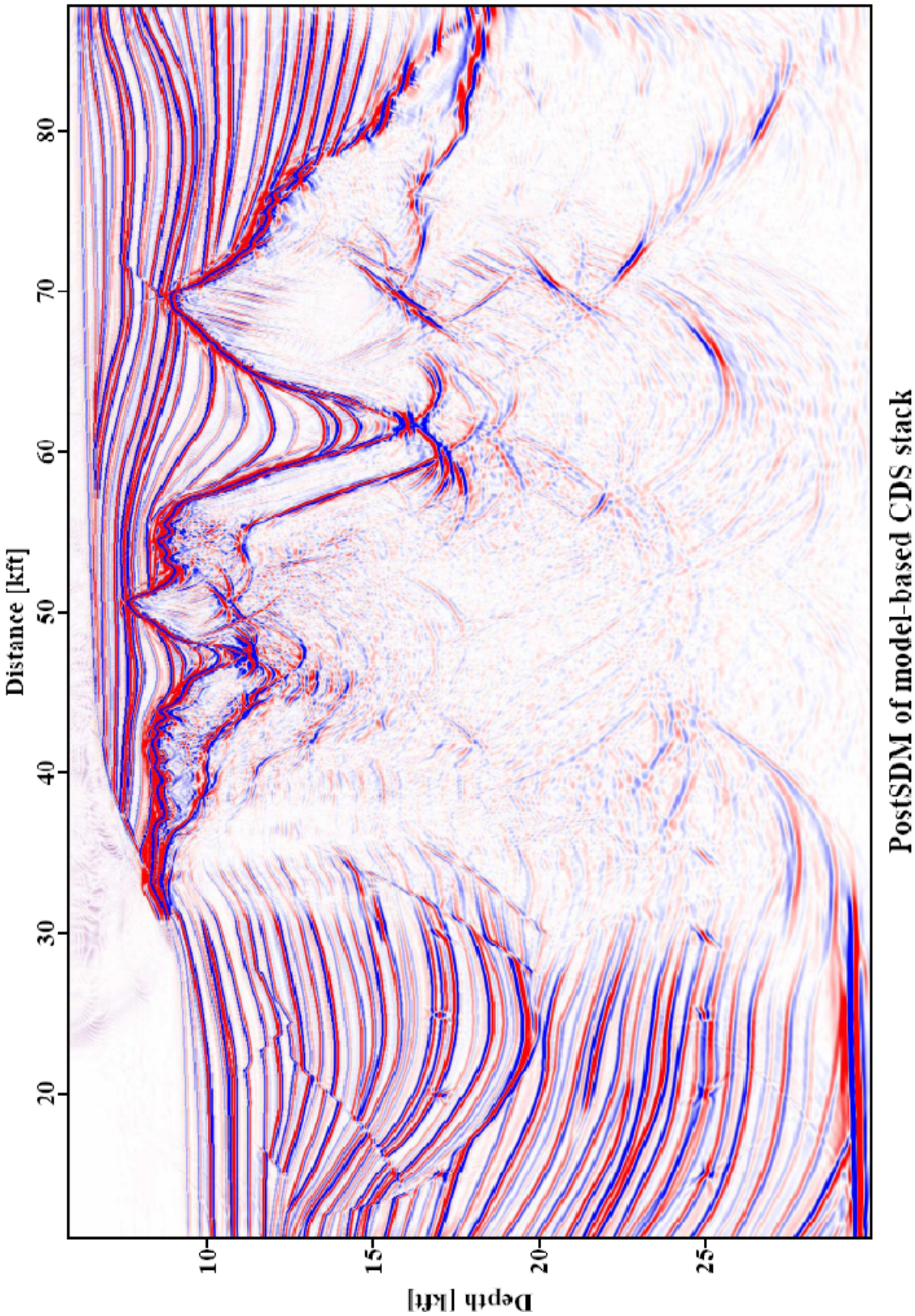

Figure 5.16: Poststack Kirchhoff depth migration result for the model-based CDS-stacked section shown in Figure 5.15. Faults and diffractors are clearly focused.

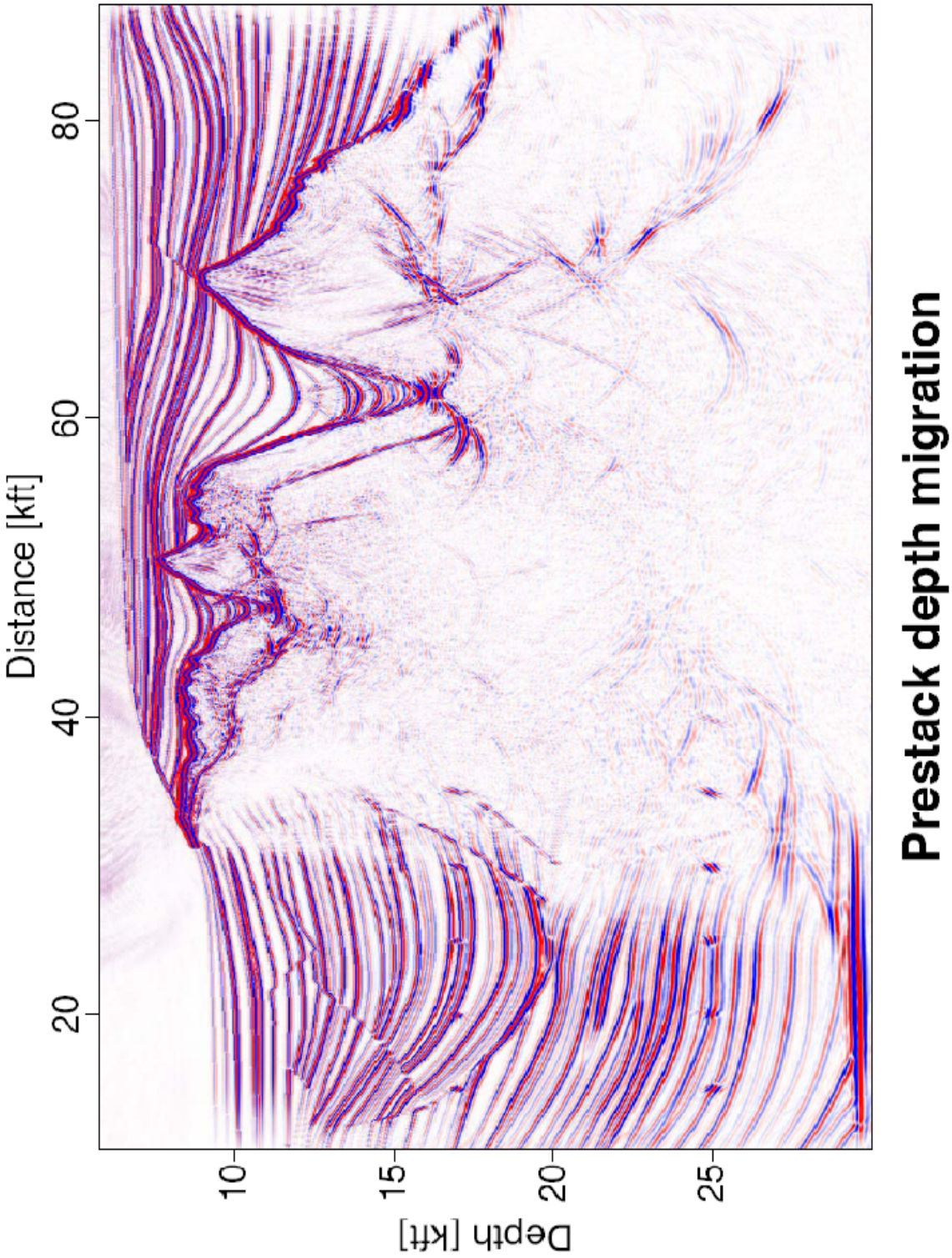

Figure 5.17: Prestack Kirchhoff depth migration result with high similarity to the poststack result shown in Figure 5.16. To allow for a fair comparison, the used offset range coincides with the one used for the CDS stack and the image gathers have been muted such that they mimic the time-dependent CDS stacking aperture in offset direction.

section with the highest coherence values encountered for each individual ZO sample is depicted Figure 5.18. It allows to identify the reflection events and to evaluate the local fit between CDS operator and event. As this section only shows the coherence for the most prominent events, less prominent events show up as local lowering of the coherence of the more prominent events they intersect. This behavior can, e. g., be seen along the diffraction events caused by the two horizontal rows of diffractors in the model.

Together with the coherence along the most prominent operator, the corresponding stacking parameters α and R_{CDS} can be stored for each ZO sample as well. Due to the model-based calculation of R_{CDS}, these sections look much smoother, see Figures 5.19 and 5.20, and more consistent than their CRS-based counterparts, almost without any outliers, see Figures 5.6 and 5.7.

At first glance, this appears to be useful for all applications using α and $R_{CDS} \equiv R_{NIP}$. One of them is inversion, either layer-based inversion (Majer, 2000; Majer et al., 2000), NIP wave inversion with a smooth model, or a combination of both (Müller, 2005, 2007). However, for inversion the attributes of the model-based CDS stack are obviously of no use, because they are forward calculated. Inverting for them will, thus, at best reproduce the macro-velocity model already employed for stacking.

In contrast, another application of these two attributes, i.e., R_{CDS} and α, clearly benefits from their more stable and contiguous character: the attribute-based time migration introduced as a by-product of the CRS stack (Mann et al., 2000; Mann, 2002). This application is based on a point-to-point remapping of the stacked amplitude from the stationary point for ZO, i. e., the ZO image location, to the estimated apex of the time migration operator. Evidently, the latter estimation directly benefits from the higher stability of the attributes. In addition, this point-to-point migration can be performed separately for each emergence angle (not only for the most prominent one), such that the entire process turns into an operator-to-point migration much more similar to conventional poststack time migration. Under such fortunate conditions, even this very simple approach yields striking results: Figure 5.21 shows the result of this model-based time migration using the forward-modeled attributes. Although there are various artifacts in this section, the sedimentary part looks quite reasonable. Note that CRS-based

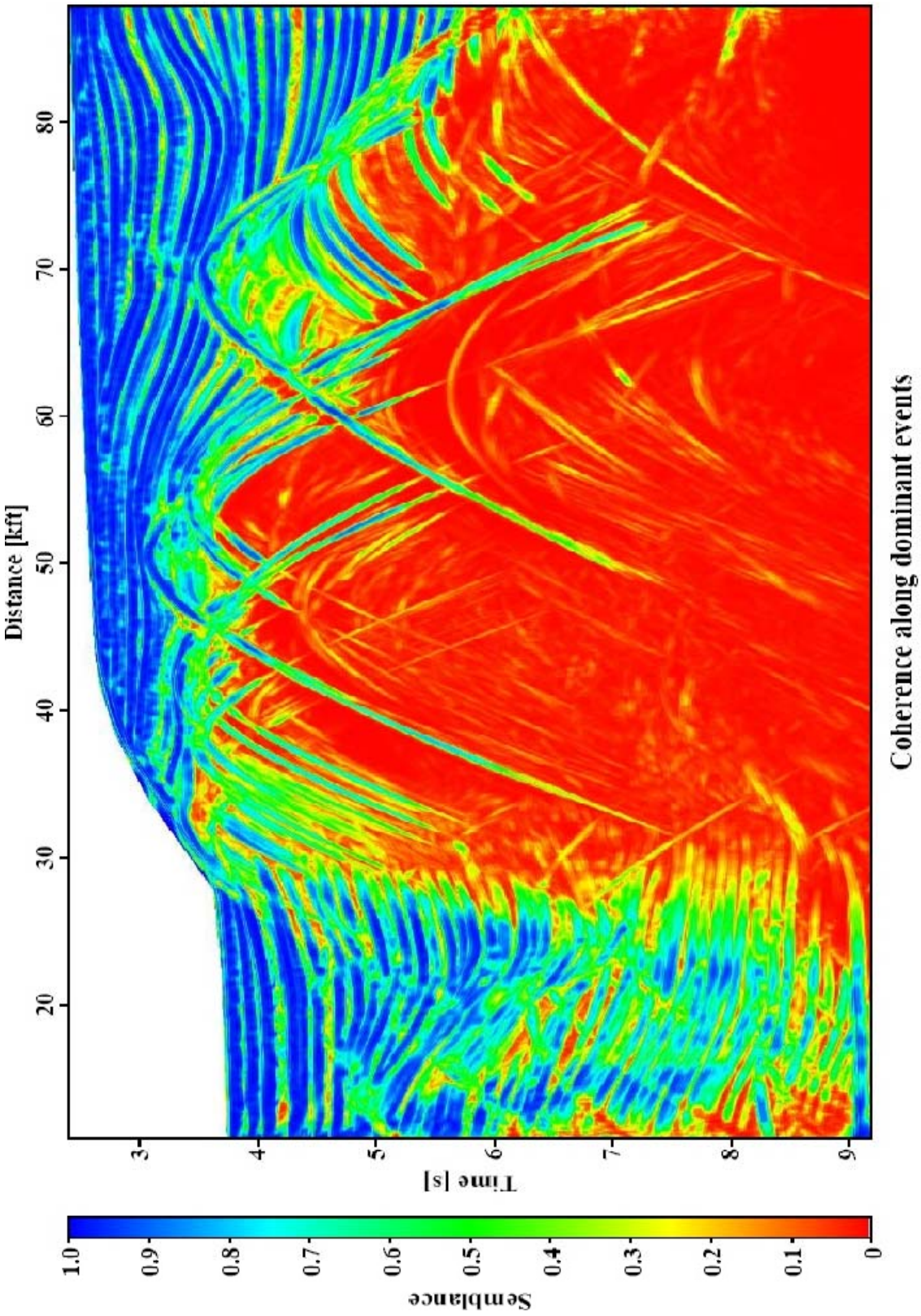

Figure 5.18: Section of the maximum encountered semblance corresponding to the stack section shown in Figure 5.15.

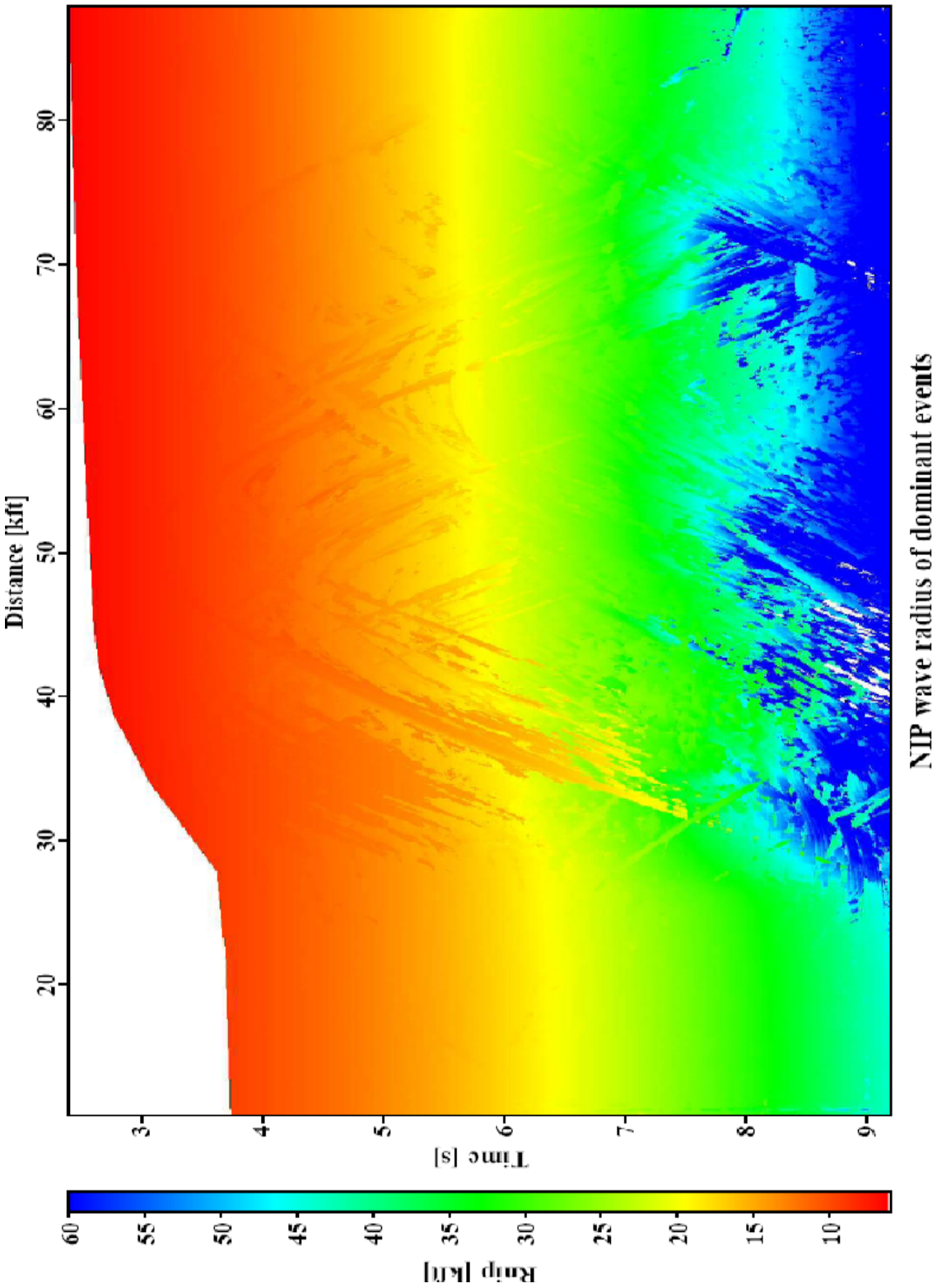

Figure 5.19: Section with the radius of curvature of the NIP wavefront ($R_{NIP} \equiv R_{CDS}$) for the dominant events associated with model-based CDS stacked section shown in Figure 5.15.

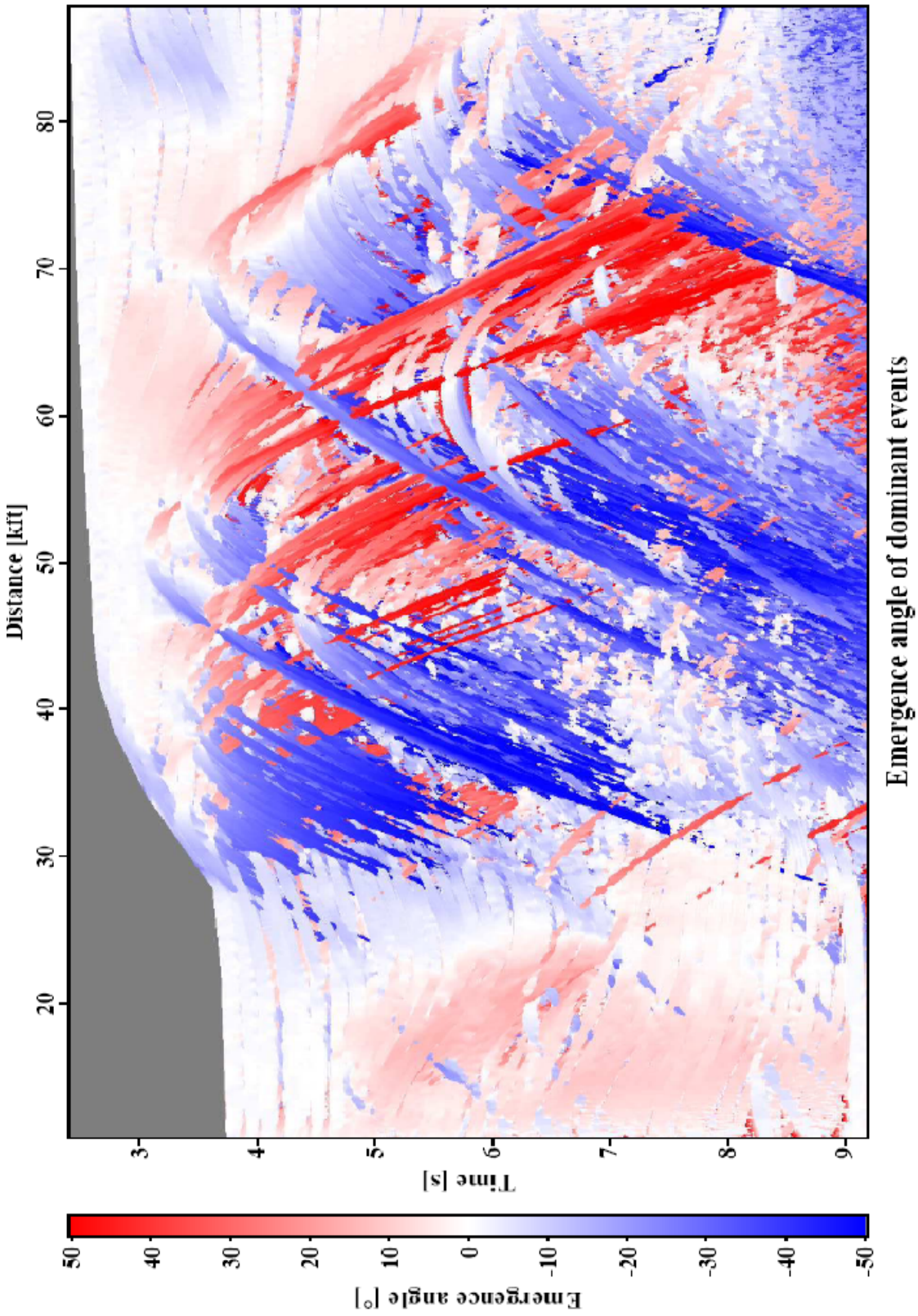

Figure 5.20: Emergence angle section for the dominant events associated with the model-based CDS stacked section shown in Figure 5.15.

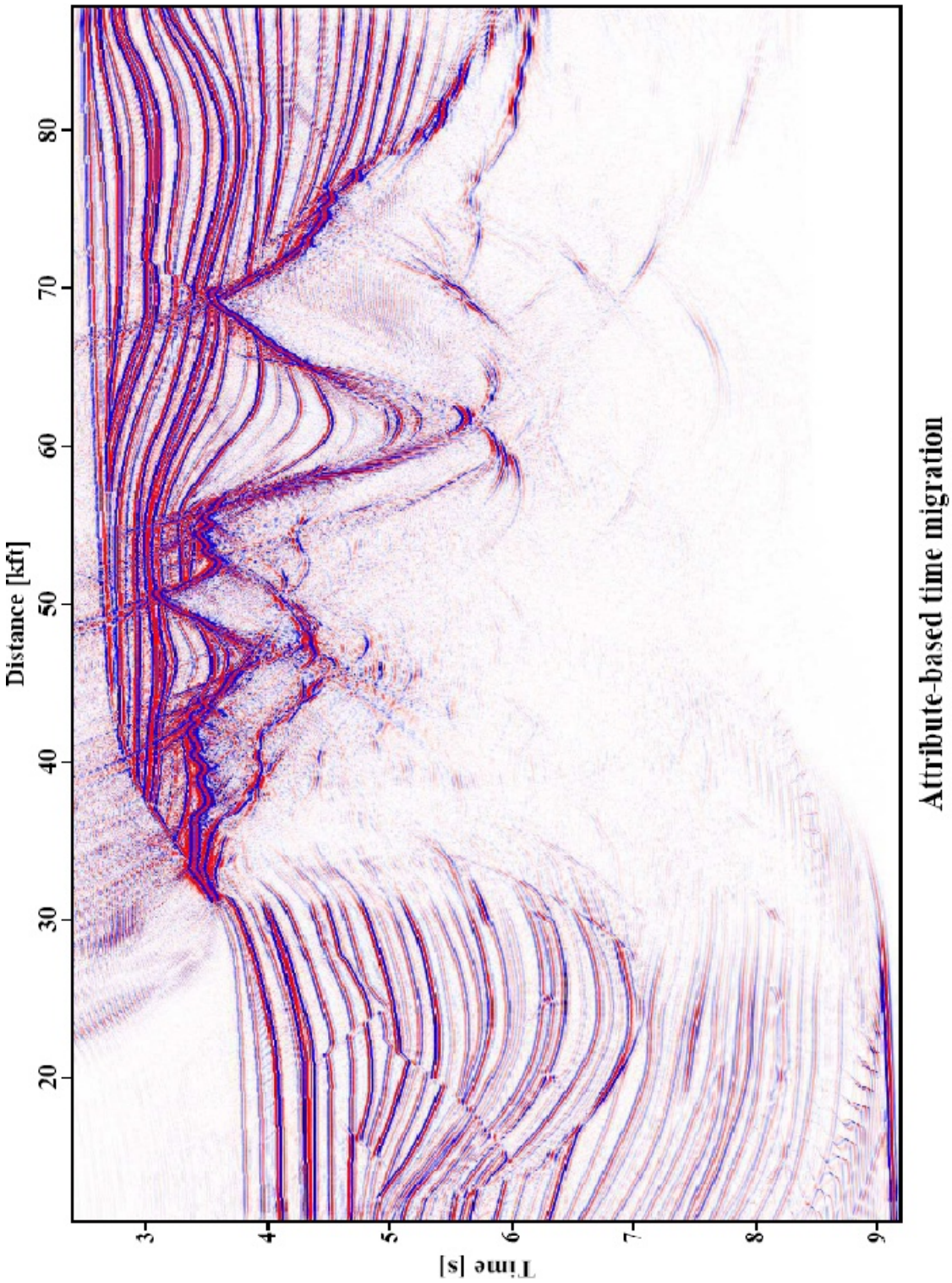

Figure 5.21: Attribute-based time migration result obtained as a by-product of the model-based CDS stack. Compared to the CRS-based counterpart (Figure 5.22), more stable attributes and the quasi-continuous range of contributing emergence angles render this very simple approach feasible for the sedimentary regions.

counterpart shown in Figure 5.22 strongly suffers from high frequency noise and huge gaps in the events due to missing or unstable attributes, especially close to the top of the salt. Finally, I would like to mention that the data-driven CDS approach is not suited for this kind of migration, as it does not yield the required parameter R_{NIP}.

In Figure 5.23 I compared the subsets at the left hand side of the stack section of different methods. As shown in Figure 5.23b the diffractor curves are well image while they are covered by the strong reflectors in Figure 5.23a. The result in Figure 5.23c is very similar to the result in Figure 5.23b, obviously the difference is the computation cost. In Figure 5.24 the subsections at the top of the stacked sections are shown. In Figure 5.24b the continuity of the events are preserved. The result in Figure 5.24c is very similar to the result in Figure 5.24b. Finally I zoom in to the migrated section at the left hand side and top of the salt. In Figure 5.25 the subsections at the left hand side of the migrated sections are shown. As can be observed in Figure 5.25b the faults are well imaged and the diffractors are well focused compare to the result in Figure 5.25a. Figure 5.25c shows the same result and in some cased the diffractors are better focused compare to the result in Figure 5.25b. Although, the main difference, as mentioned before, is the computation cost. In Figure 5.26 shows the subsections at the top of the salt. Figure 5.26b shows less artifices compare to the result in Figure 5.26a. In Figure 5.26c all artifices disappear and the syncline are well image compare to the results in Figure 5.26a and Figure 5.26b.

5.2. Real data example

The 2-D seismic land data used for the first application of the newly implemented model-based CDS stack was acquired in 2003 in the Upper Rhine Graben in EW-direction at about 49°11'N, 8°11'E near the city of Landau, Rheinland-Pfalz, Germany which is about 28*km* NW of Karlsruhe. This data set was acquired by *Deutsche Montan Technologie (DMT) GmbH* along two almost parallel lines having a separation of ≈ 2.5*km* and a length of ≈12*km*. The acquisition was performed for *HotRock EWK Offenbach/Pfalz GmbH* with the intention to obtain a structural image of the subsurface relevant for a projected geothermal power plant. The latter was intended to be based on two boreholes, reaching a depth of ≈2.5*km*, where a strongly fractured horizon of hot-

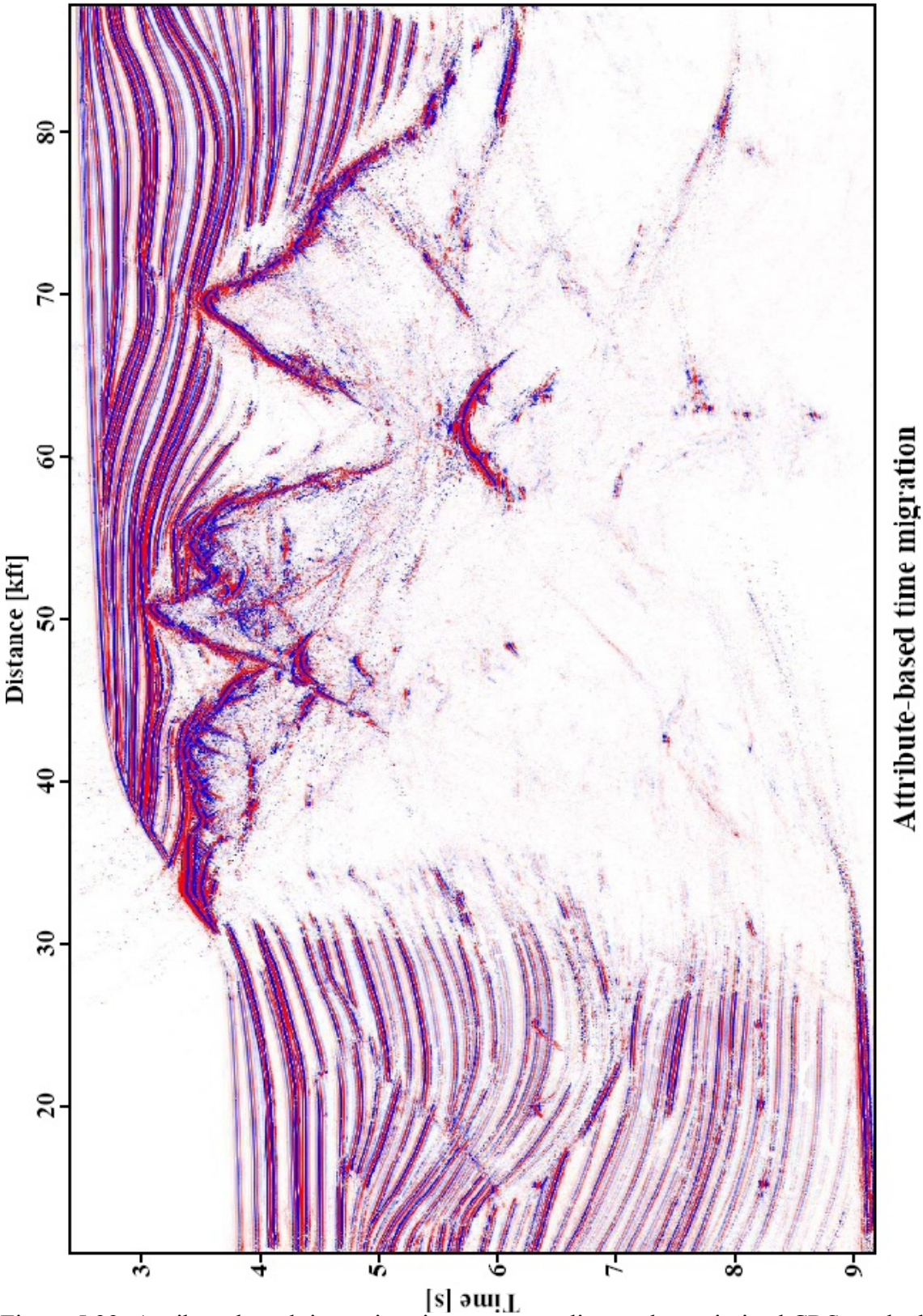

Figure 5.22: Attribute-based time migration corresponding to the optimized CRS stacked section shown in Figure 5.9 (after Mann, 2002).

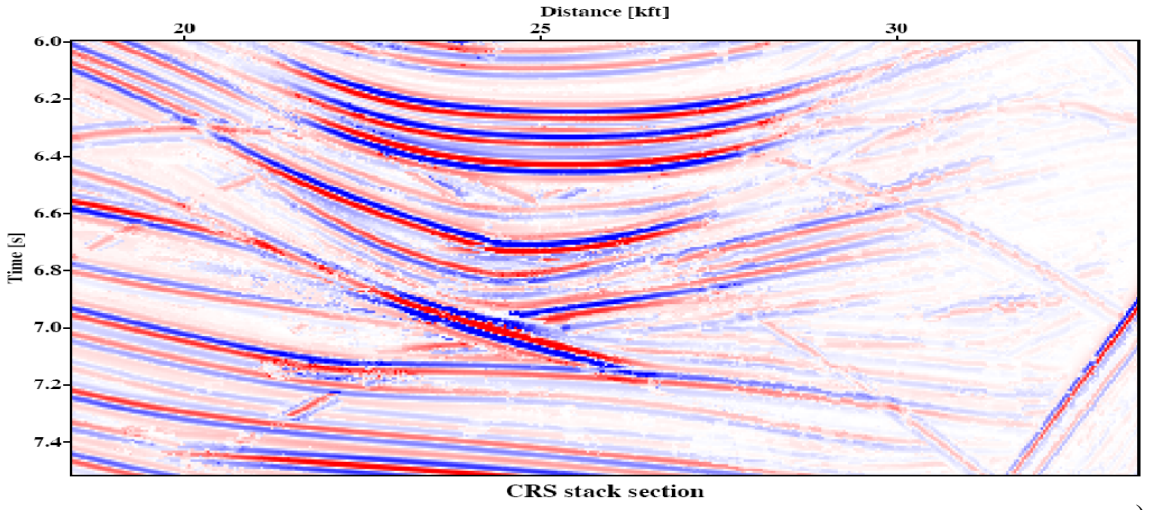

a)

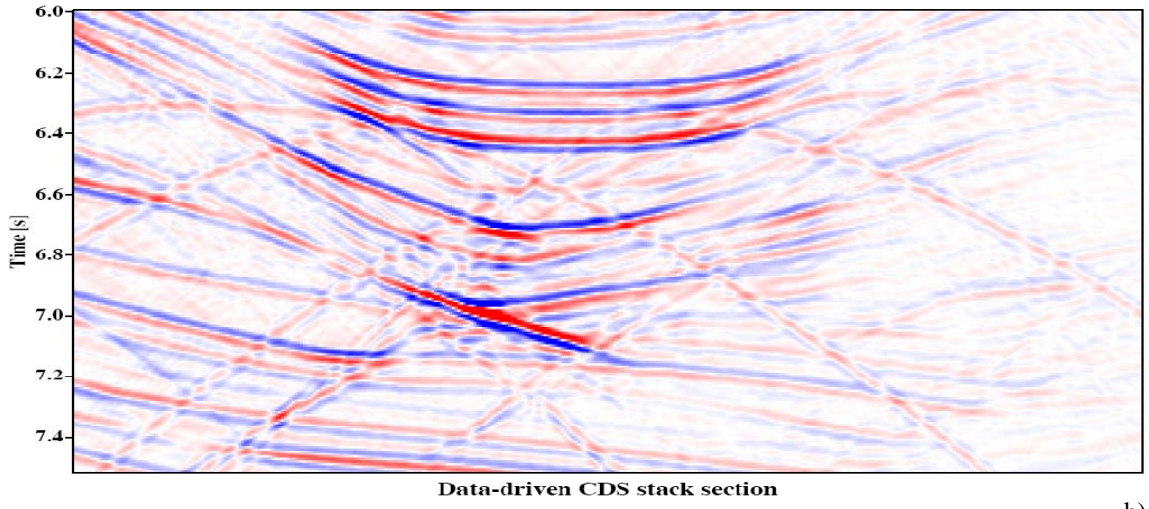

b)

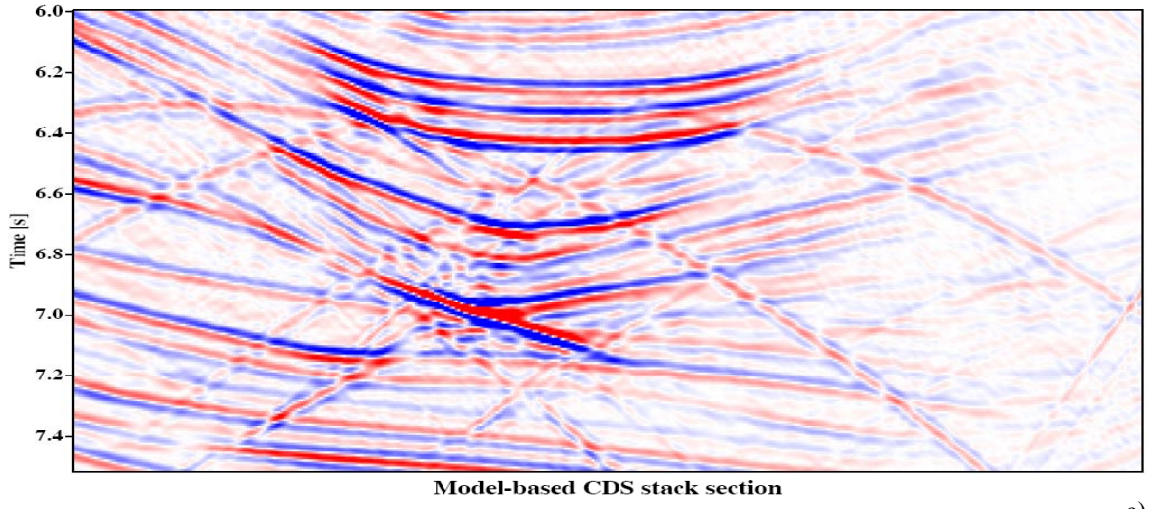

c)

Figure 5.23: Sigsbee 2A data set, a) Subset of CRS stack section b) Subset of data-driven CDS stack section c) Subset of model-based CDS stack section.

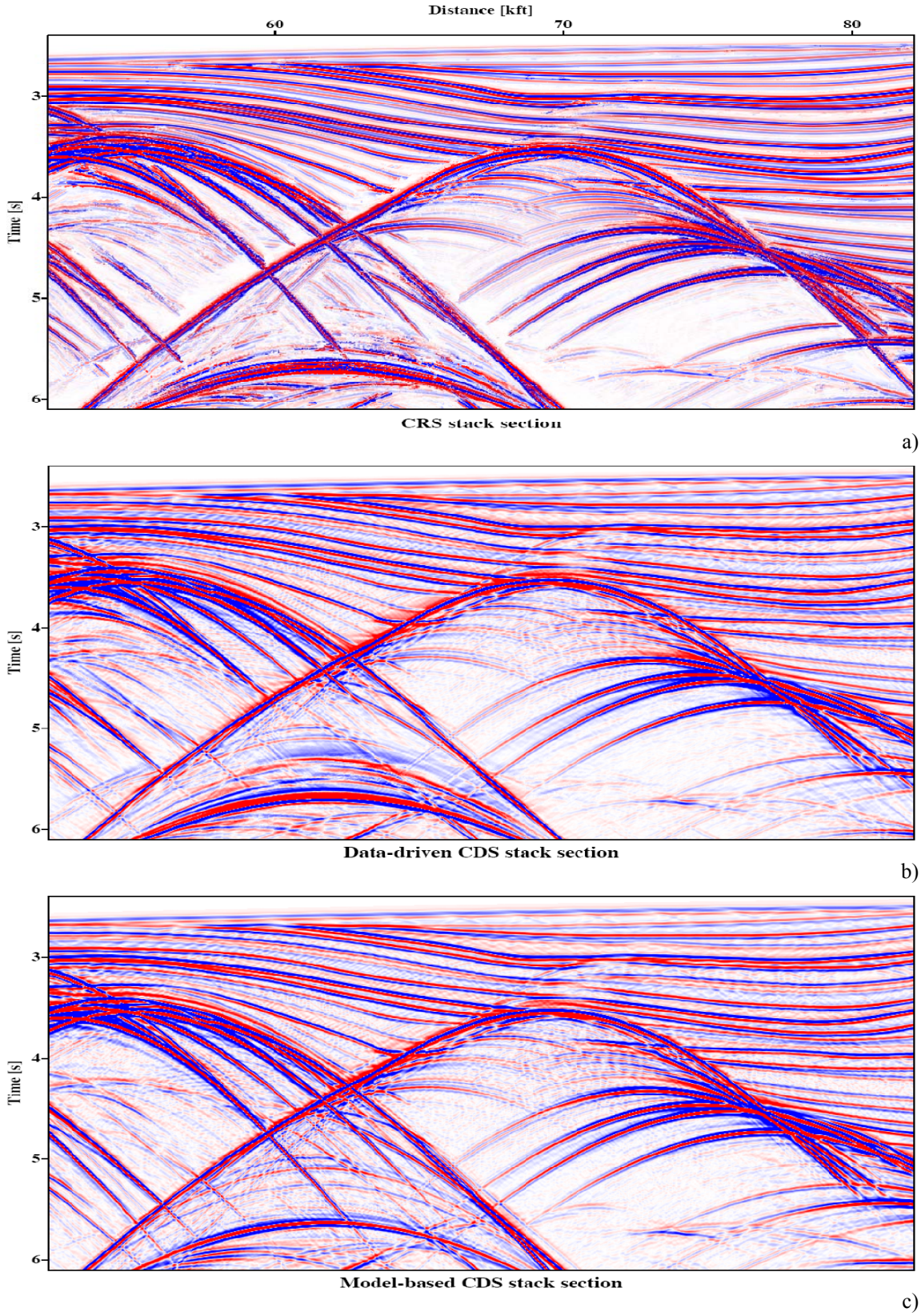

Figure 5.24: Sigsbee 2A, a) Subset of CRS section b) Subset of data-driven CDS stack section c) Subset of model-based CDS stack section.

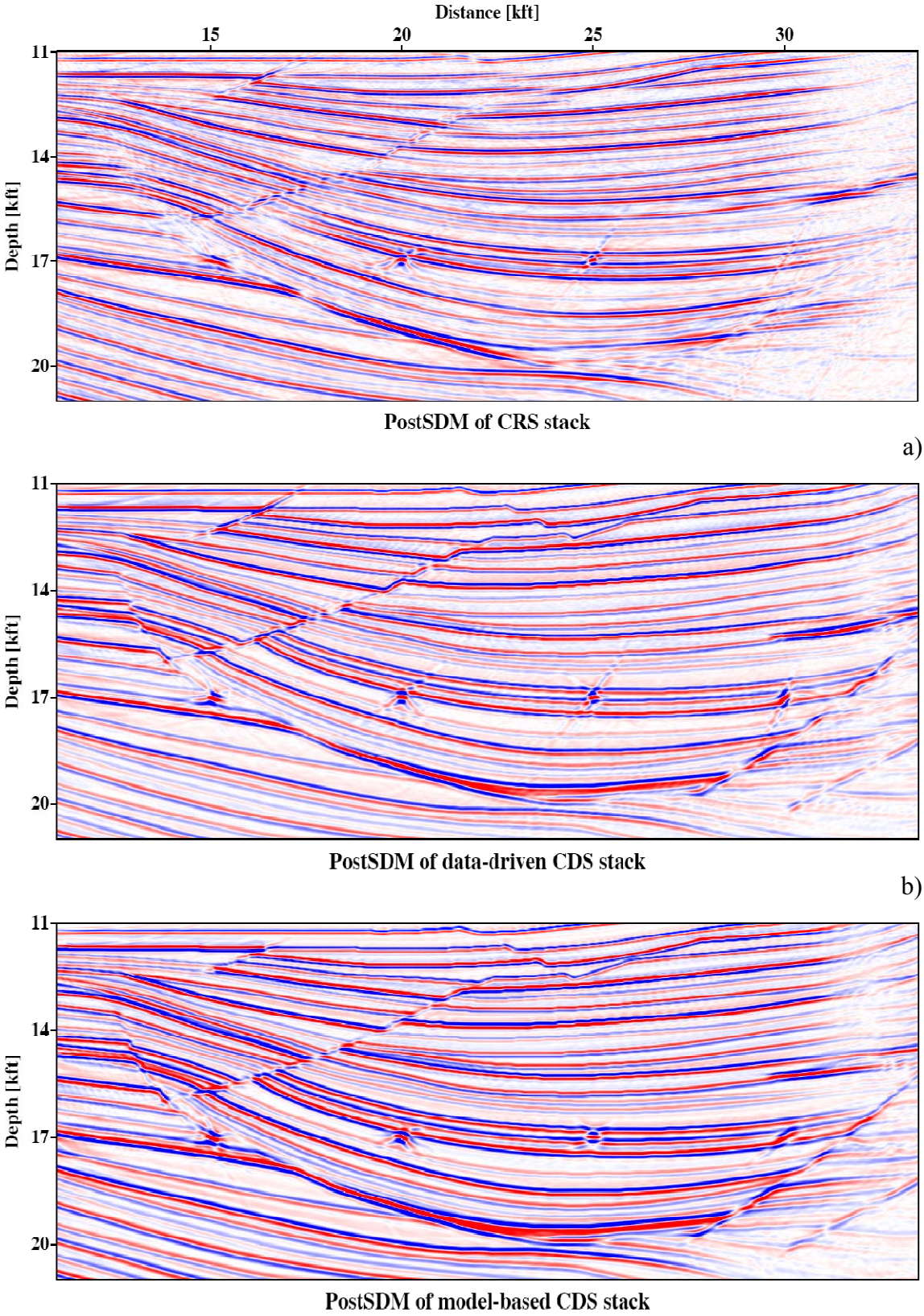

Figure 5.25: Sigsbee 2A, a) PostSDM of the CRS stack result. b) PostSDM of the data-driven CDS stack result c) PostSDM of model-based CDS stack result.

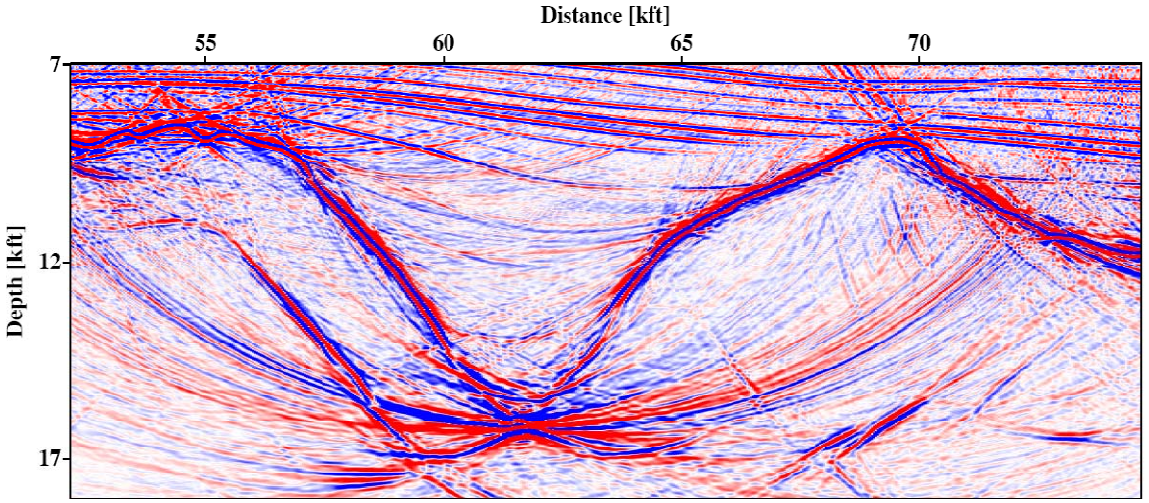

a)

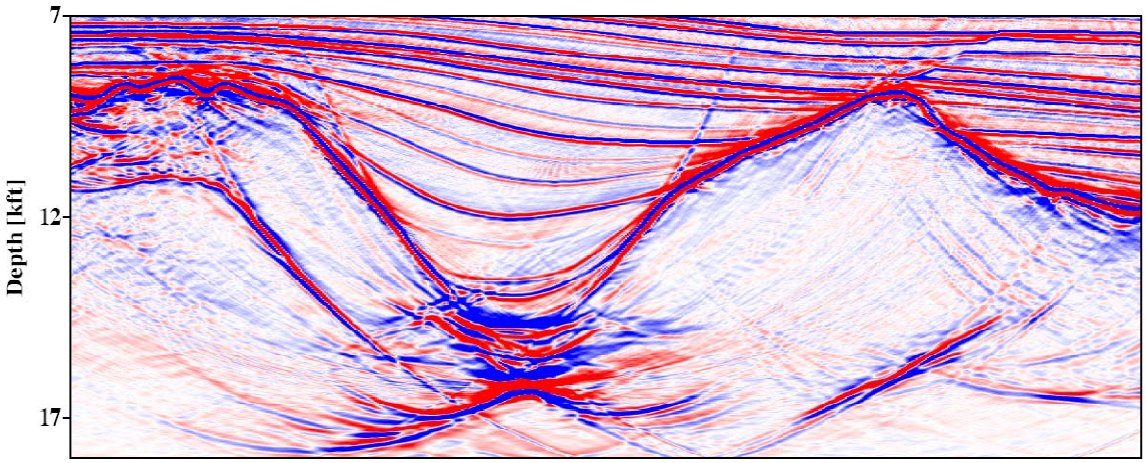

b)

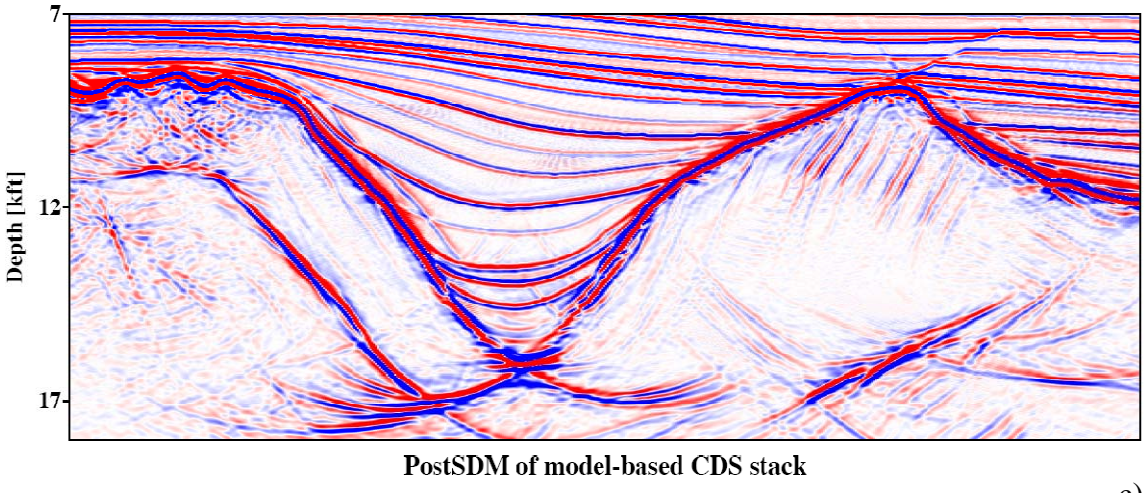

c)

Figure 5.26: Sigsbee 2A, a) PostSDM of CRS stack b) PostSDM of the data-driven CDS stack c) PostSDM of the model-based CDS stack.

water-saturated lacustrine limestone is located. The Upper Muschelkalk (middle member of the German Trias, consists of a sequence of limestone and dolostone) contains 80 m of limestones (shelly, nodular, and some oolitic) and dolomites with thin marls and mudstones, being at a depth of about 2.5*km* at the project location. The carbonate rocks are broken up and fractured by major fault zones in the Rhine Graben rift system. The regularly orientated vertical open fractures are the basis of the exploitation concept adopted to allow high flow rates.

As the achievable production rate depends mainly on the degree of fracturing of the target horizon and the number of faults reached by the boreholes, a detailed knowledge of the subsurface structure is essential. The acquisition parameter of the data are compiled in Table 5.6. For further details on source signals and preprocessing, I refer to Soleimani (2009).

A sequence of CRS stack and NIP-wave inversion has been applied to the data to obtain the smooth macro-velocity model shown in Figure 5.27. This CRS-based imaging

Shot and receiver geometry	
Number of shots	240
Shot interval	50m
Number of receivers	250
Receiver interval	50m

Midpoint and offset geometry	
Number of CMP bins	427
Maximum CMP fold	47
CMP bin interval	25m
Offset range	4000m

Recording parameters	
Recording time	4s
Sampling interval	2ms

Frequency content	
From…to	12 to 100 Hz
Duration	10s

Table 5.6: Acquisition parameters of the prestack for real data (Soleimani, 2009).

workflow has been extensively discussed by Mann et al. (2003) and Hertweck et al. (2004). During the model-based CDS stack, kinematic and dynamic ray tracing is performed in this model on a coarse emergence angle grid ranging from -30° to 30° in steps of 2°. Due to the chosen parameterization of the kinematic ray tracing system, the

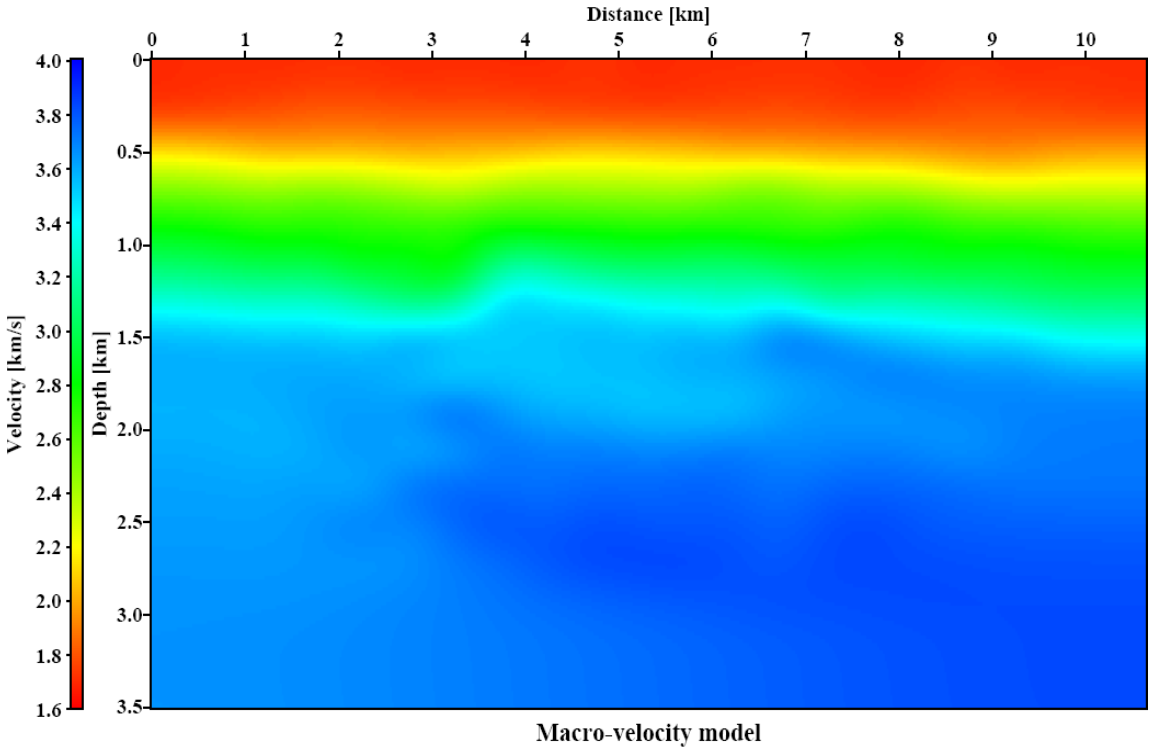

Figure 5.27: The macro-velocity model used for ray tracing obtained by CRS-based imaging workflow (Hertweck et al., 2004)

stacking parameters R_{CDS} are directly available on the temporal target grid without any need for interpolation along the rays. For the stack and the semblance calculation, I used a finer emergence angle incrementing of 1° with stacking parameters linearly interpolated in between neighboring rays on the coarse grid. I have compiled the parameters which have been used for processing in Table 5.7.

The Figure 5.28 shows the final result of the CRS stack. the stack confined to the first projected Fresnel zone after local three-parameter optimization and event-consistent smoothing (Hertweck et al., 2005) of the CRS attributes. The reflection events show up with a high signal-to-noise ratio and high continuity. However, many events are truncated and only appear in fragments where they intersect more dominant events. Evidently, this will lead to artifacts in a subsequent poststack migration. Especially faults will be poorly imaged, as the corresponding edges of diffractions are largely missing in the stacked section. In the data-driven CDS-stacked section shown in Figure 5.29, these conflicting dip situations are fully resolved and the interference of intersecting events is properly simulated and many new steep events show up. The

processing time for the data-driven CDS stack method is about 140 hours or close to six days with same hardware mentioned in Table 5.5.

Context		Processing parameter	Setting
General parameter		Dominant frequency	30 Hz
		Coherence measure	Semblance
		Data used for coherence analysis	Original traces
		Temporal width of coherence band	56 ms
Target zone		Number of target traces	391
		Number of samples per target trace	1450
		Temporal target sampling	2ms
		Time offset in target traces	0.1s
		First CDP number in target zone	420
		Last CDP number in target zone	810
Aperture and taper		Constant ZO aperture	200 m
		Minimum CMP aperture	200m @ 0.2s
		Maximum CMP aperture	2000 m @ 2s
		Relative taper size	30%
Model-Based CDS parameter		Time stepping factor for ray tracing	5
		Time stepping for ray tracing	0.4ms
		First model trace corresponds to CDP	402
		Last model trace corresponds to CDP	828
		Lateral padding to the left	30 grid points
		Lateral padding to the right	5 grid points
		Maximum emergence angle for search	30°
		Minimum emergence angle for search	-30°
		Emergence angle increment for ray tracing	2°
		Emergence angle increment for stacking	1°
		Turning rays	Disallowed
		Lateral velocity model spacing	20m
		Vertical velocity model spacing	20m
		Number of lateral velocity samples	569
		Number of vertical velocity samples	180
		Processing time	32.15 minute
Hardware		CPU	Pentium 4, 2.6GHz
		RAM	1GB
		Compiler	GNU 4.1.2
		OS	SuSE Linux 10.2

Table 5.7: Processing parameters used for the ZO simulation of the real data set by means of model-based CDS stack method.

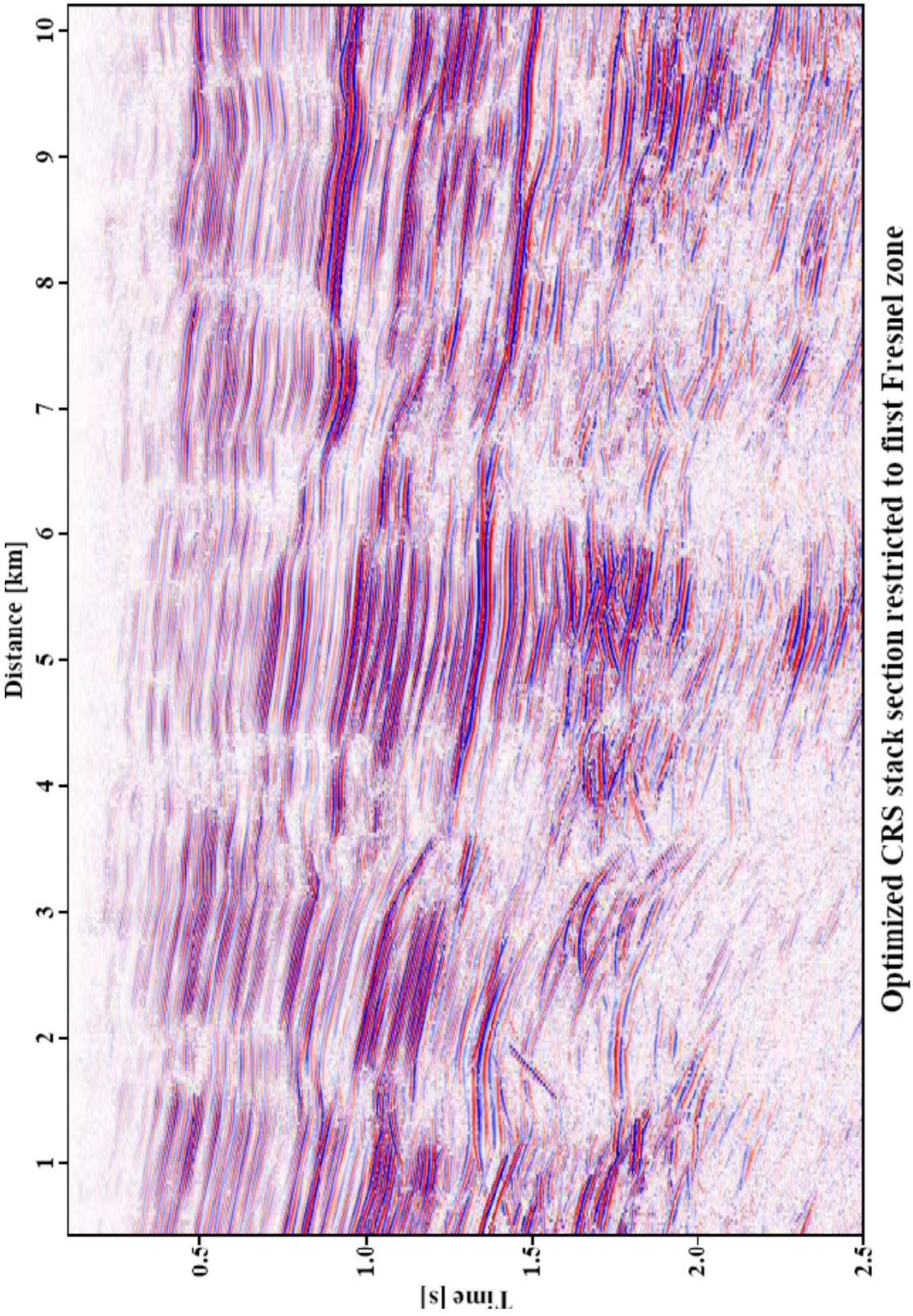

Figure 5.28: CRS-stacked section restricted to the projected first Fresnel zone (after Soleimani, 2009)

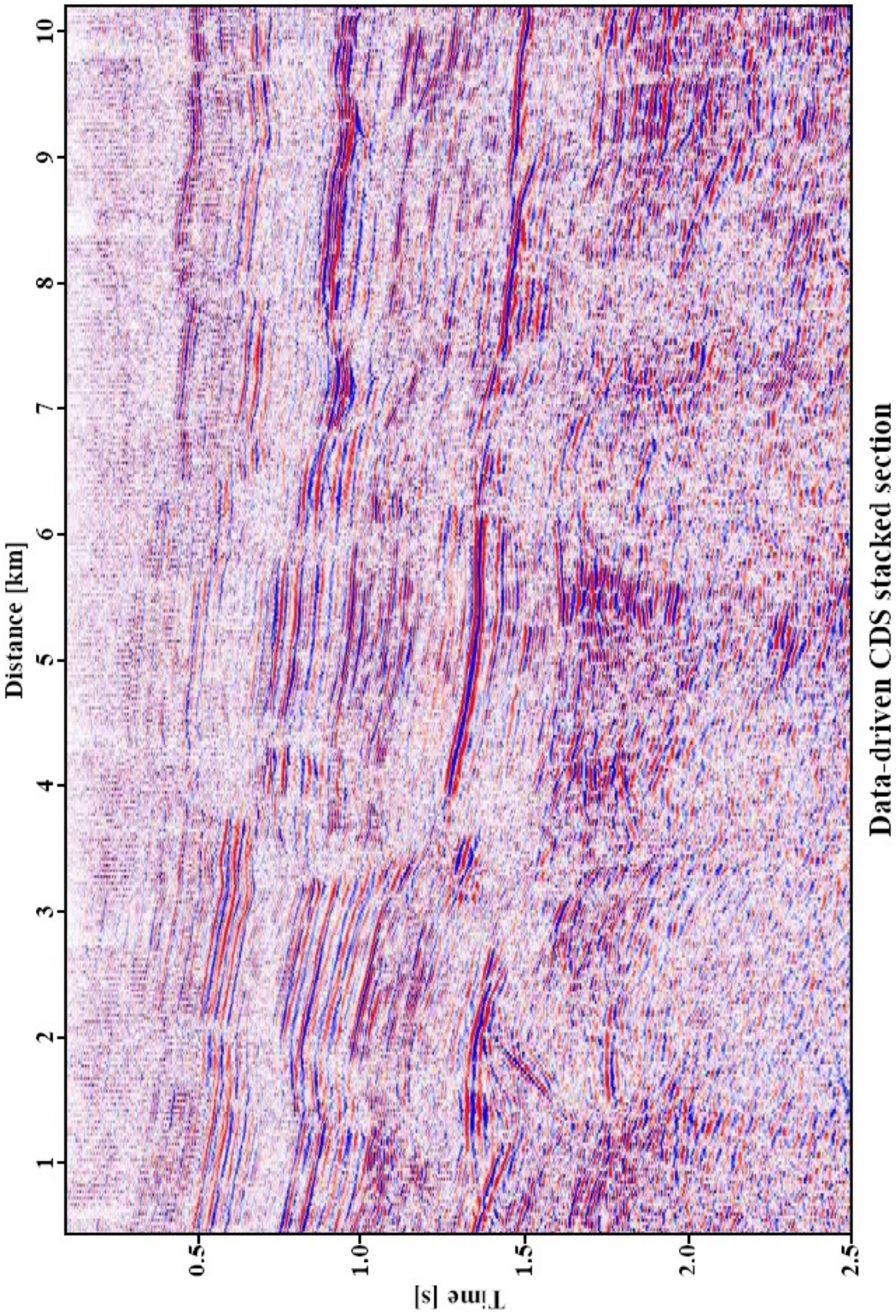

Figure 5.29: Result of the data-driven CDS-stack (after Soleimani, 2009).

Finally, Figure 5.30 shows the result obtained with the model-based CDS stack approach. For this section, all contributions for all considered emergence angles are simply superimposed, without any weighting or thresholding based on coherence. There are even some more steep and/or strongly curved events in the lower part compared to its data-driven counterpart. However, the strong continuous reflection events in the CRS stack result appear much weaker here. I will discuss the probable reason for this effect below. In any case, the model-based CDS approach is significantly faster than its data-driven counterpart. Depending on the chosen parameters for the attribute search, the model-based approach is one to two orders of magnitude faster, although I additionally calculate semblance along the operators which is not required for this simple, unweighted and unthresholded kind of stack.

As mentioned above, the semblance can be calculated along each CDS operator in addition to the stack value. In this way, it is possible to keep track of the stacking parameters of the operator yielding the highest semblance value and to generate attribute sections i.e., for α and R_{NIP}. In Figure 5.31 the R_{CDS} section can be compared with the optimized and smoothed NIP wave radius section obtained from the CRS stack shown in Figure 5.32. Following the notation introduced in the preceding chapter, the latter represents $R_{NIP,data}$, whereas the CDS result represents $R_{NIP,mod}$. At locations where the CRS attributes are determined in a stable manner, these two attributes should only differ by the aperture-dependent spread length bias. Indeed, both sections are very similar to each other, especially for the well-determined part up to about 1.8s. This result demonstrates that our forward-modeling in the CDS stack, the NIP-wave inversion, and the CRS stack itself are consistent with each other. Thus, I can be quite confident that the forward-modeling in the CDS approach is working properly.

Figure 5.33 shows the optimized and smoothed emergence angle section. Compared to the emergence angle section obtained by the model-based CDS stack approach shown in Figure 5.34, although difficult to be seen, along some of the events both section almost coincide, indicating that the same events have been parameterized at the corresponding ZO locations.

Generally, the model-based CDS stack has for many ZO locations encountered the highest coherence for steep and/or strongly curved events which appear only as a few fragments in the CRS result. Mainly, it can be expect that the CDS traveltime operator

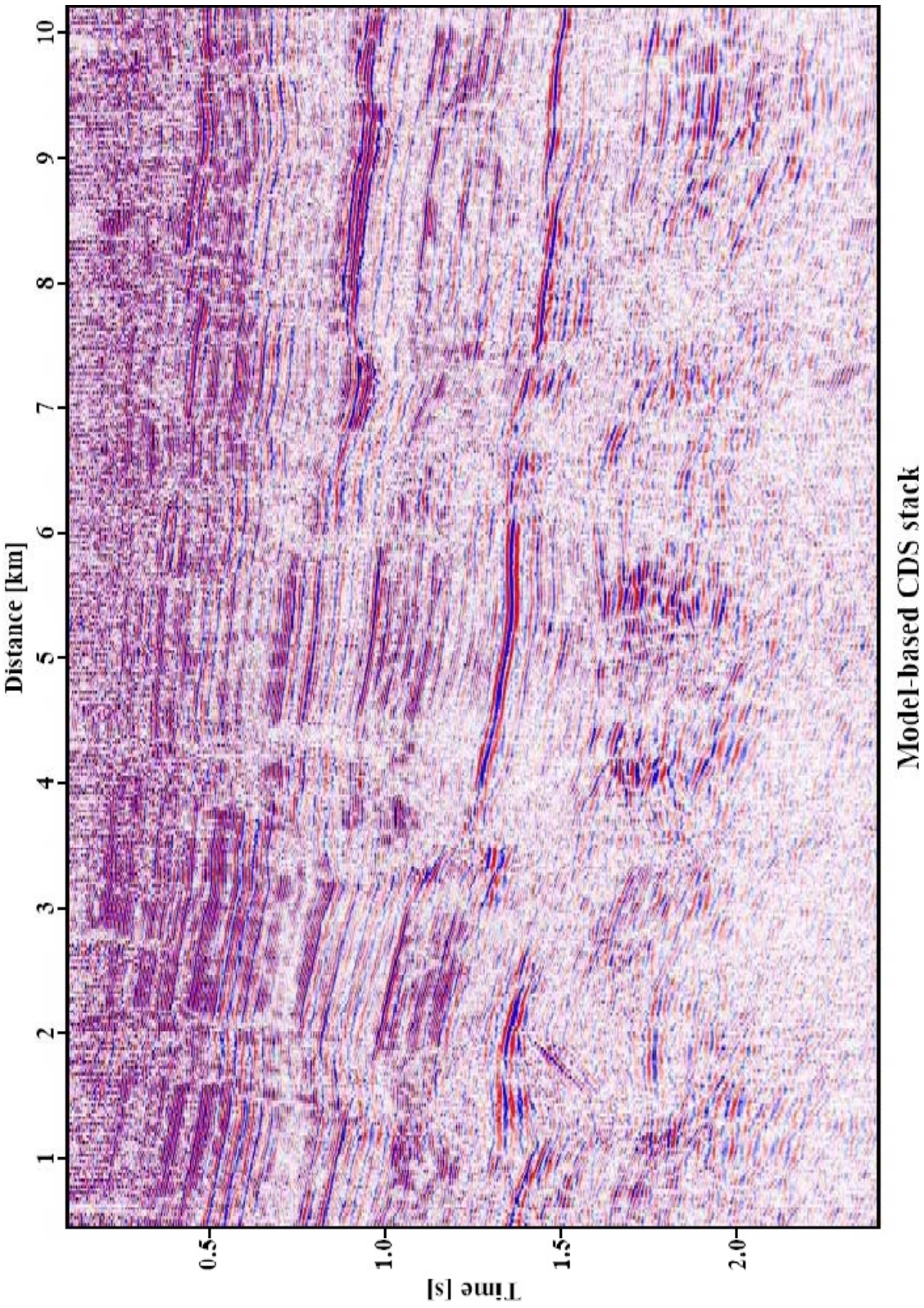

Figure 5.30: The result of model-based CDS stack approach generated in a significantly smaller computation time.

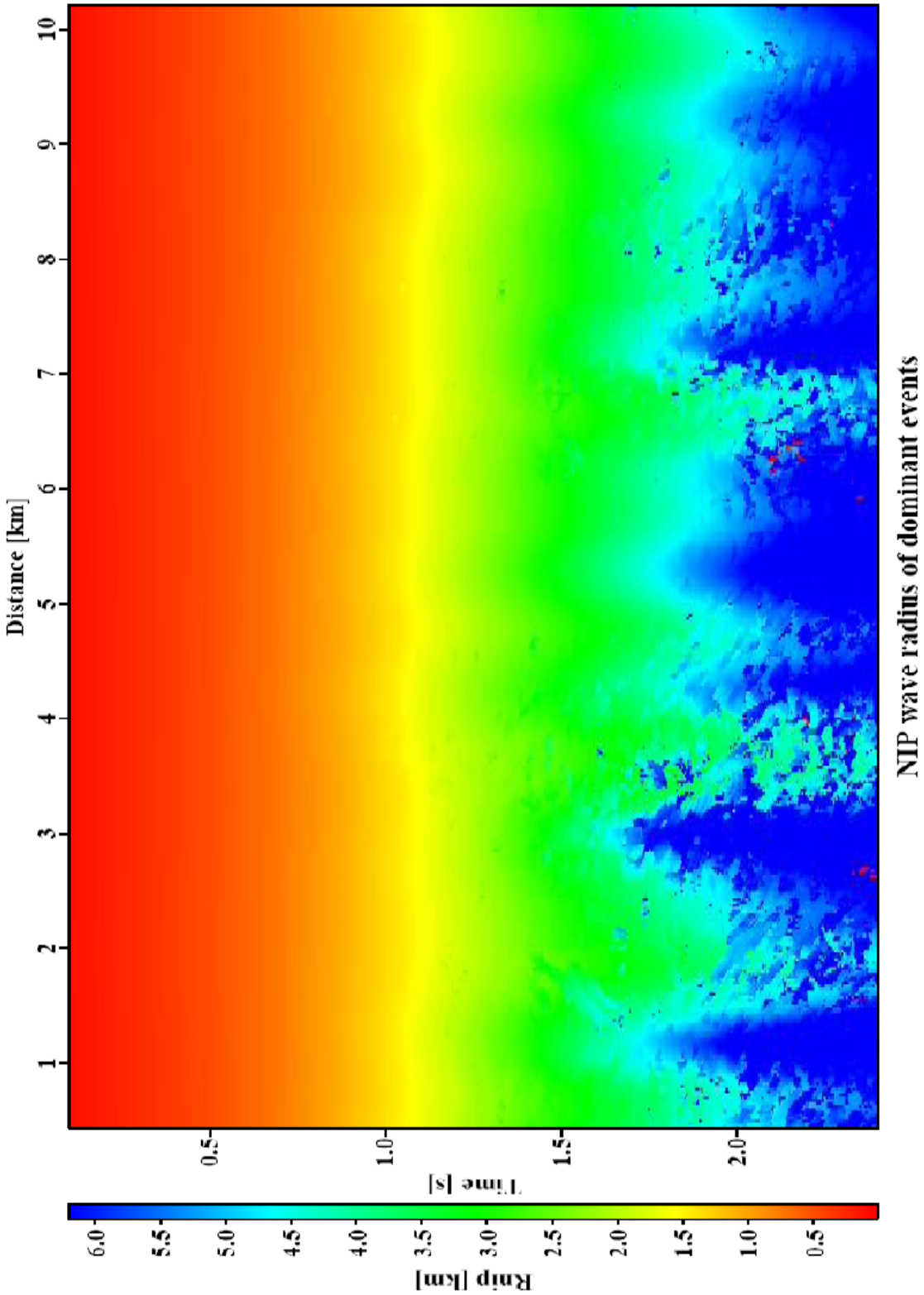

Figure 5.31: Section with radius of curvature of the NIP wavefront ($R_{NIP} \equiv R_{CDS}$) for the dominant events associated with model-based CDS stacked section shown in Figure 5.30.

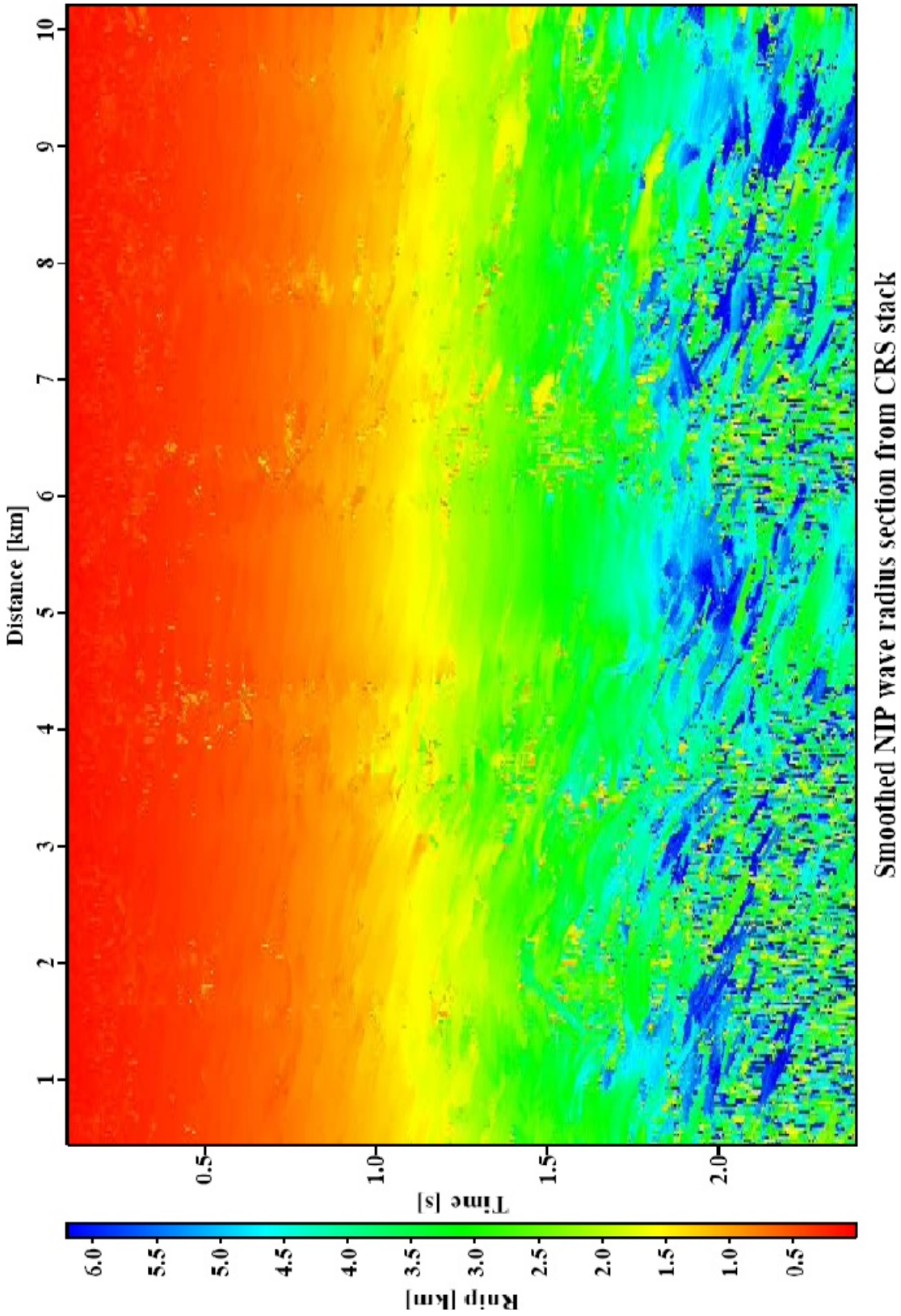

Figure 5.32: CRS-based NIP wave radius section after event consisting smoothing.

will better fit to the diffraction events. This has been observed for the data-driven CDS approach and seems to be even more pronounced in the model-based approach. Figures 5.35 and 5.36 depict the maximum coherence values encountered along the CRS operators and CDS operators, respectively. Note the different scales used in these figures. The CRS-based result shows very distinct reflection events with high coherence, but almost no indication of detected diffraction events. The vertical strips with relatively low coherence are associated with faults where lots of edge diffraction events complicate the wavefield. In contrast, the CDS-based result shows a completely different behavior: the overall semblance level is far lower and I mainly see diffraction events. These also show upon within the strips which are associated with low semblance values in the CRS result. The aperture definition used for CRS stack has been optimized to allow for a sufficiently stable determination of the normal wave radius of curvature R_N, which requires a sufficiently large aperture in midpoint direction. The CDS stacking operator has one degree of freedom less and is, therefore, less accurate for reflection events. This applies in particular for concave reflection events in which the signs of R_N and R_{NIP} usually differ. Nevertheless, the data-driven CDS stack adapts to the reflection event as closely as possible and yields an operator which still fits reflection events reasonably. As mentioned, R_{CDS} is a weighted average of the two wavefront radii in this case. However, for the model-based CDS approach, the situation is completely different. The forward-modelled radius of curvature does not at all depend on the reflector curvature or its time domain counterpart R_N, such that the corresponding operator very poorly approximates the reflection event for a larger midpoint displacement, whereas the fit in the vicinity of the central CMP gather should be very good. The smaller the ZO traveltime, the larger the relative difference between the two radii R_N and R_{NIP}, i. e., the fit in midpoint direction gets even worse. In contrast, for diffraction events, $R_N \approx R_{NIP}$, thus they are well imaged even within a large midpoint aperture and/or for small ZO times. For this reason I used a smaller midpoint aperture than it has been applied in the CRS stack method (Mann, 2002) along the common-reflection-point (CRP) trajectory discussed by Höcht et al. (1999), see Section 4.4.

For the sake of comparison, I finally applied the poststack Kirchhoff migration to the results of the different stacking methods. The migrated result for the CRS-stacked section is shown in Figure 5.37. As can be observed, the continuity of the reflection

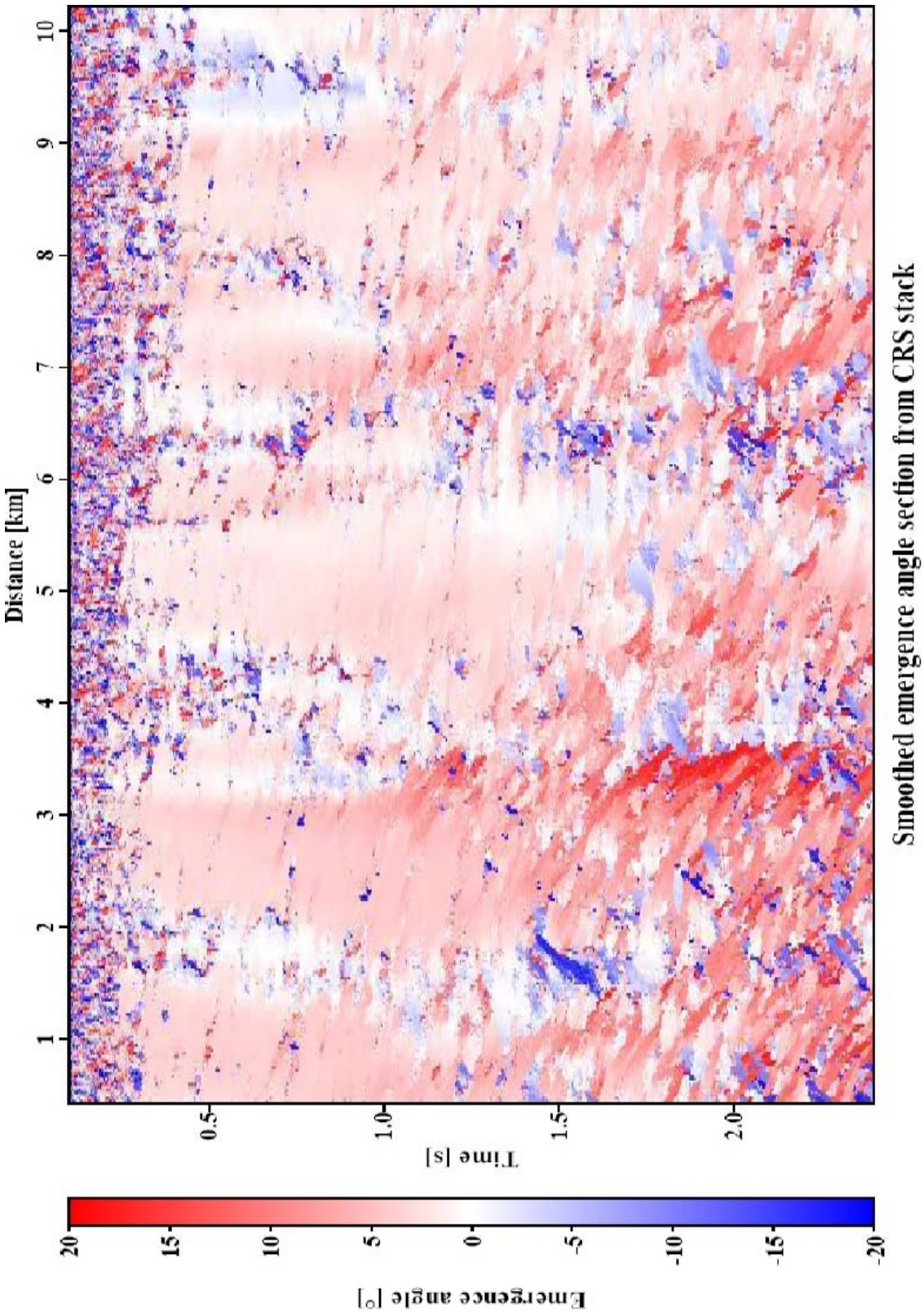

Figure 5.33: CRS-based emergence angle section after event consisting smoothing for the dominant events.

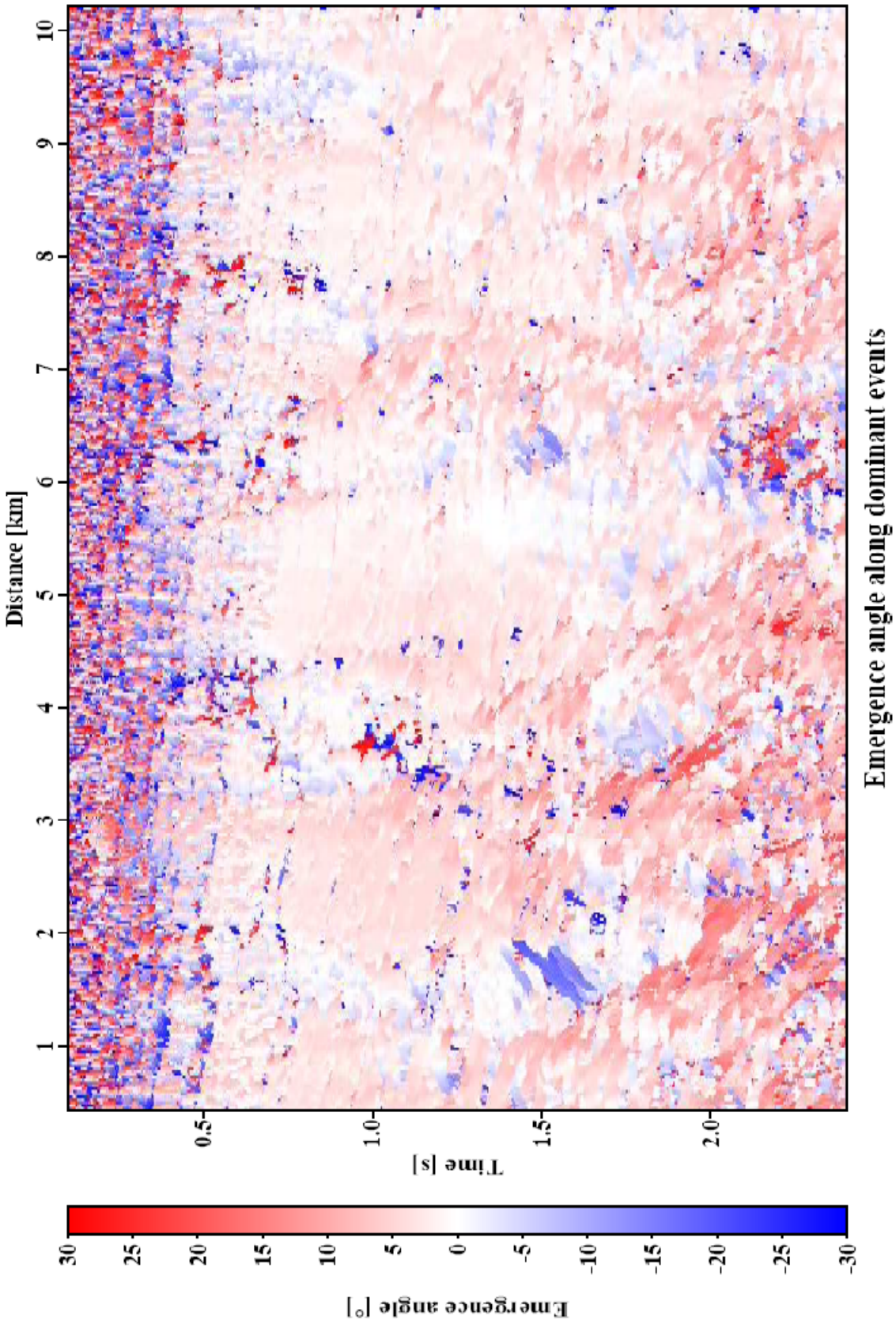

Figure 5.34: Model-based CDS emergence angle section for the dominant events.

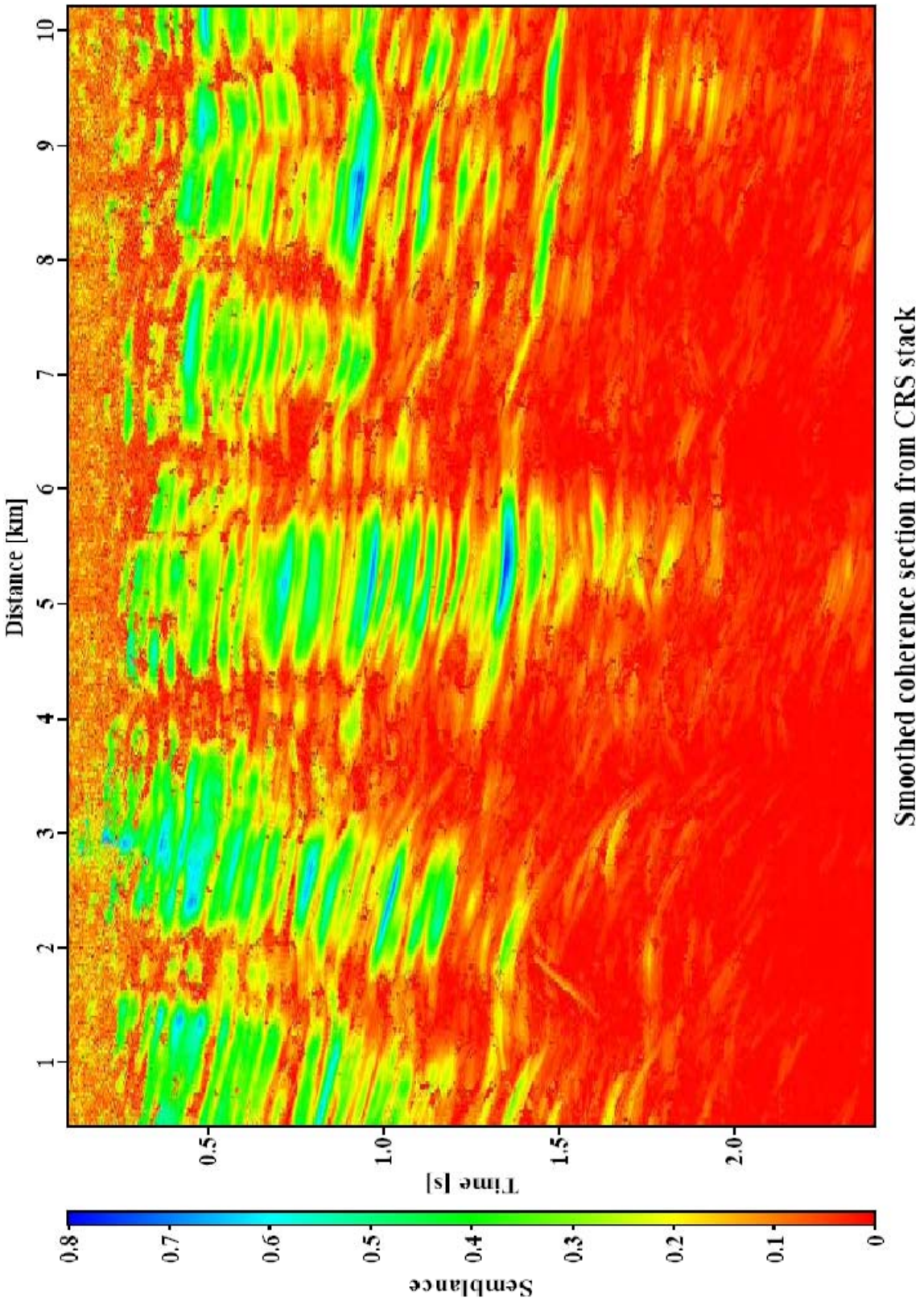

Figure 5.35: Coherence section after event consisting smoothing corresponding to the CRS- stacked section shown in Figure 5.28.

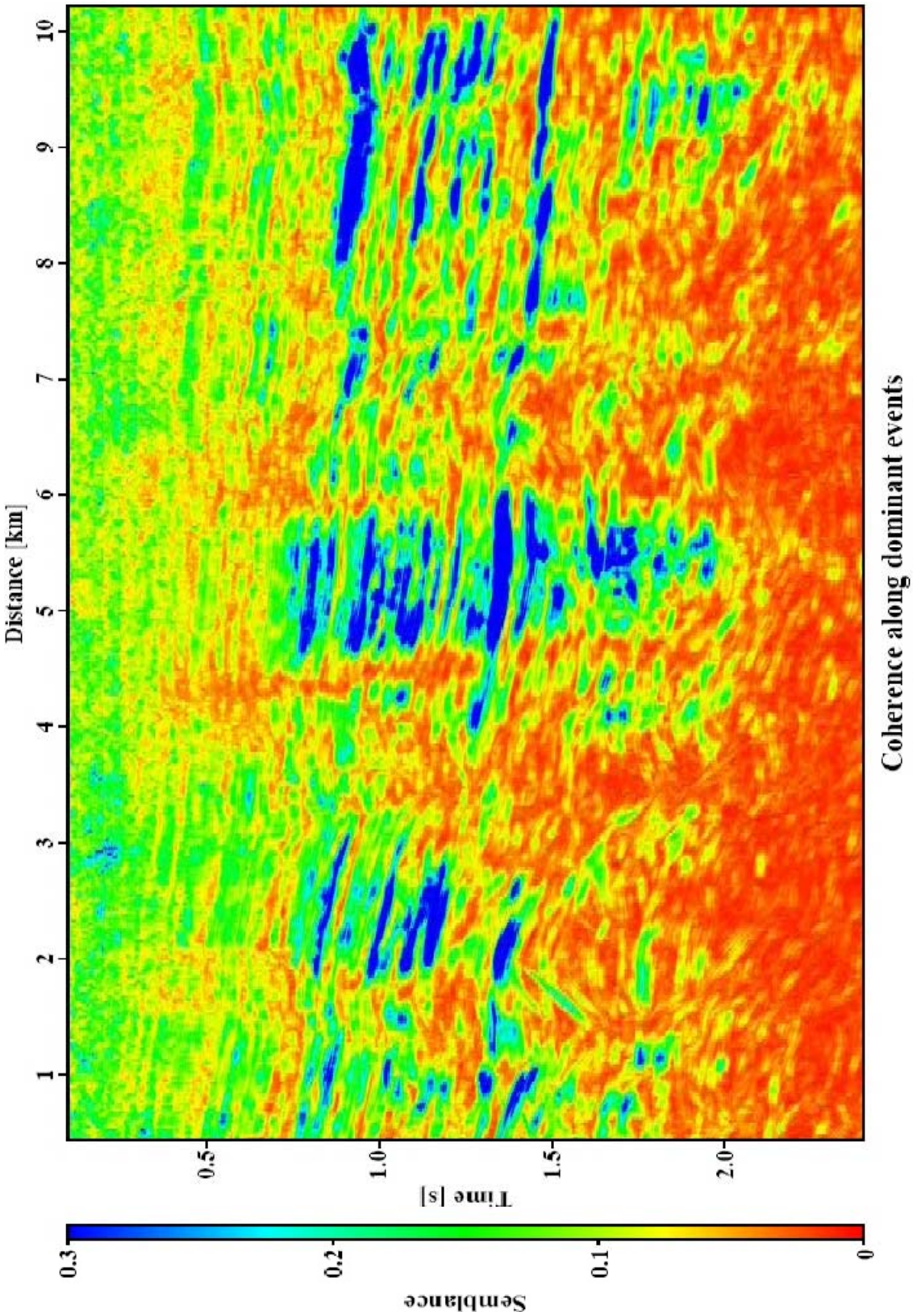

Figure 5.36: Coherence along dominant events corresponding to the model-based CDS stacked section shown in Figure 5.30.

events is only partly preserved and the localization of the faults failed. These faults which obviously generate the conflicting dip situations are located along separate reflectors in depth from 1.5*km* to 2*km* which extend along whole section. These reflectors are fragmented at some locations. These locations are not image in CRS-based migration results into full extent. Figure 5.38 shows the migration result of the data-driven CDS-stack section. As can be seen, the problem of conflicting dip situations has been solved at many locations and the continuity of the reflection events is preserved to full extent. The poststack migration of the model-based CDS-stacked result is illustrated in Figure 5.39. This section is very similar to the result of data-driven migrated section. At some locations it seems that model-based migrated result is better than its data-driven counterpart. Apart from that, the main problem of the data-driven CDS stack method is that it is too time consuming. The differences between the sections become more evident when I extract some subsections to compare how the problem of conflicting dips has been solved. Figure 5.40 shows subsections of the three different migration results. The smoothness of the reflectors is clearly observed in the CRS-based migrated result. The big fault in Figure 5.40a is not well imaged while this fault shows up well in Figure 5.40b. The migration results in figure 5.40b and 5.40c are almost the same. However, the minor faults at the right hand side of the big fault in Figure 5.40c are better imaged. Again, the main difference between the results in Figure 5.40c and 5.40b are the required computation costs.

As a final reference I applied prestack Kirchhoff depth migration to this data set as shown in Figure 5.41. This section is very similar to the poststack migration of the model-based CDS-stacked section in Figure 5.39. Some differences between these two sections are along the faults. For example, in a depth of 1.5*km* and at distance 3.2*km* prestack migration fails to image the faults, whereas the poststack migration imaged these minor faults well. In principle, the main advantage of the newly introduced method is that for the poststack depth migration obtained from the model-based CDS stack procedure, a smooth macro-velocity model of minor accuracy is sufficient. If there is no difference between the result of prestack migration and the results of the new method there is no need for a costly, more accurate velocity model building and updating for prestack migration.

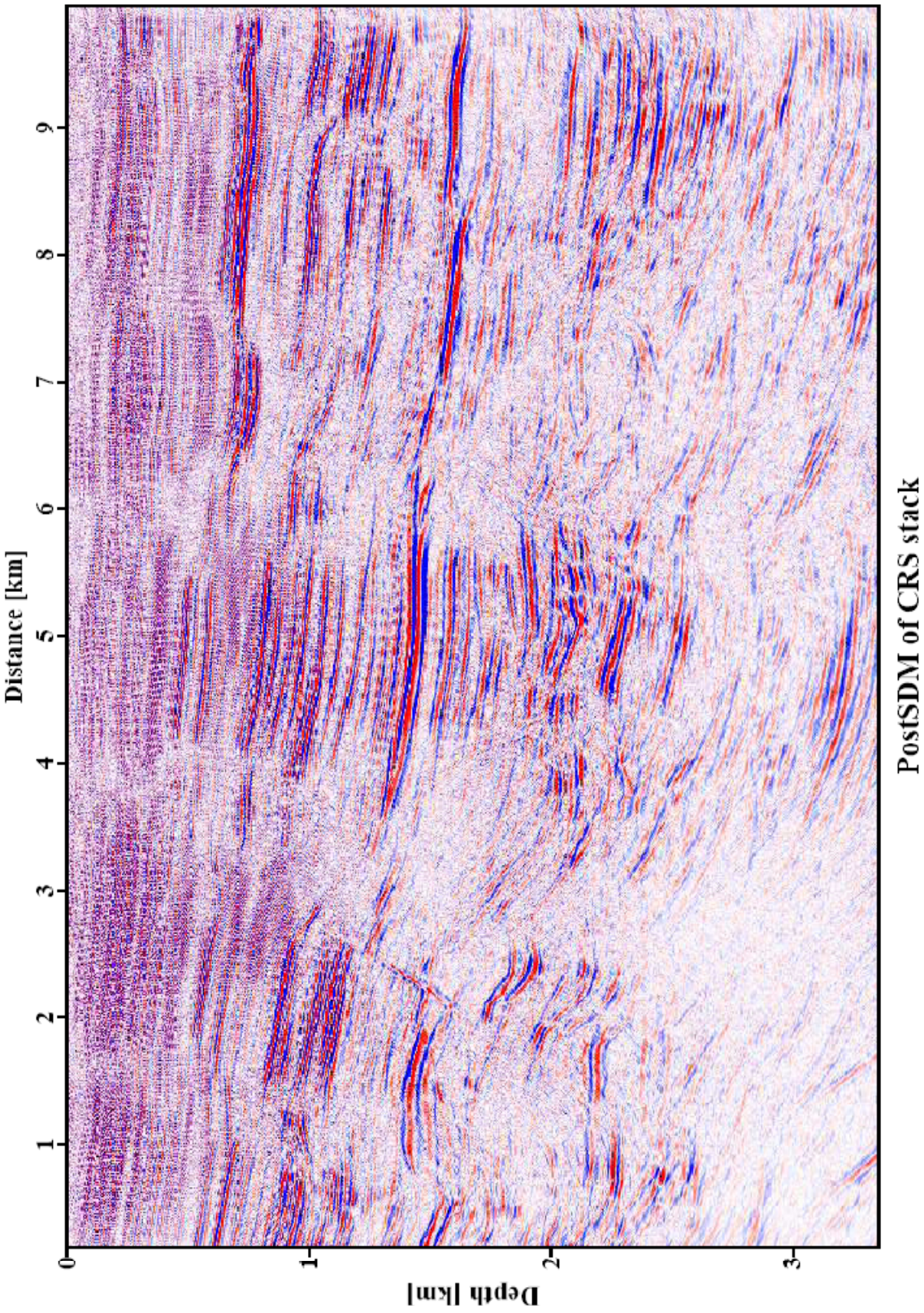

Figure 5.37: Kirchhoff poststack depth migration result for the CRS stacked section shown in Figure 5.28.

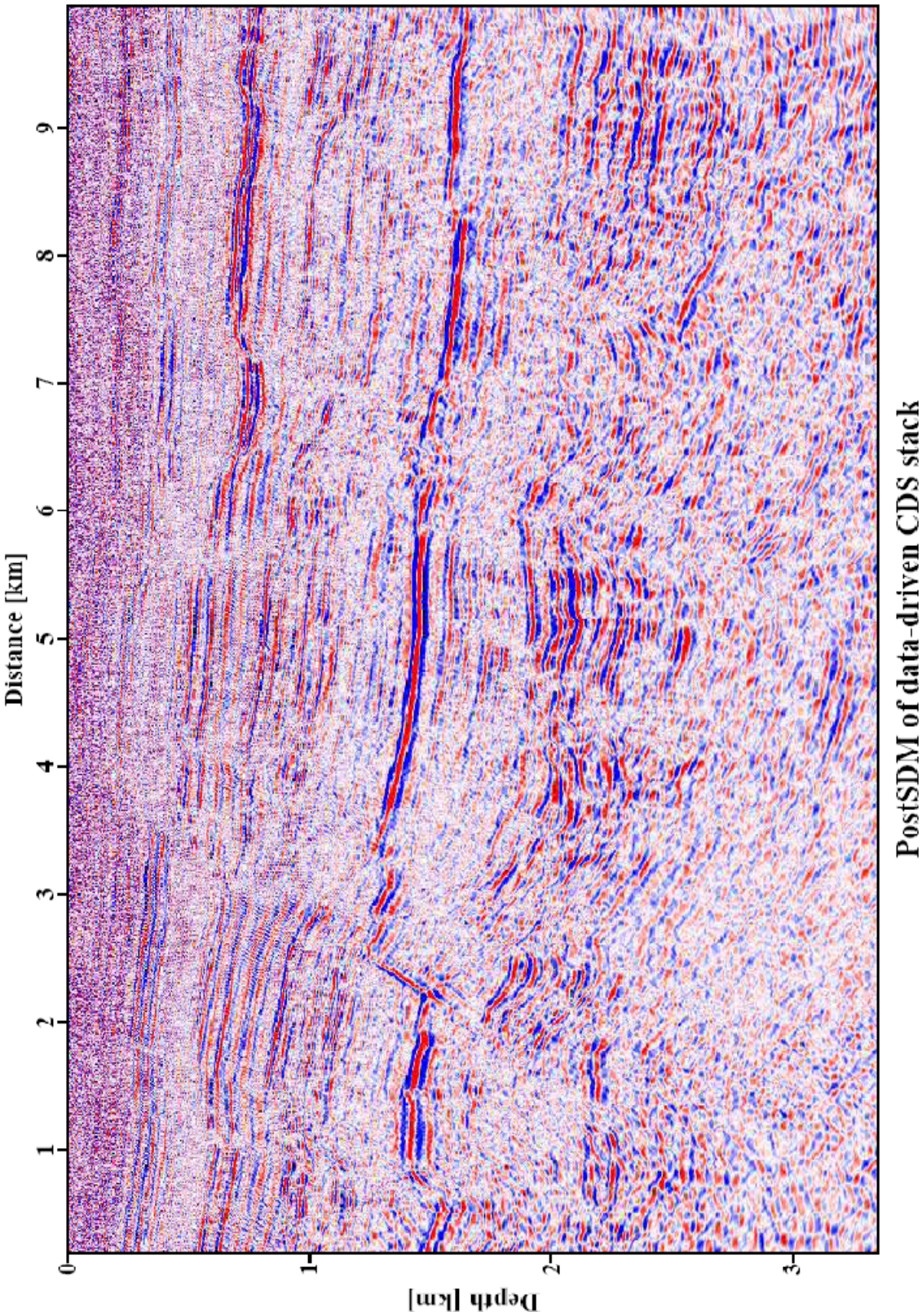

Figure 5.38: Kirchhoff poststack depth migration result for the data-driven CDS stacked section shown in Figure 5.29.

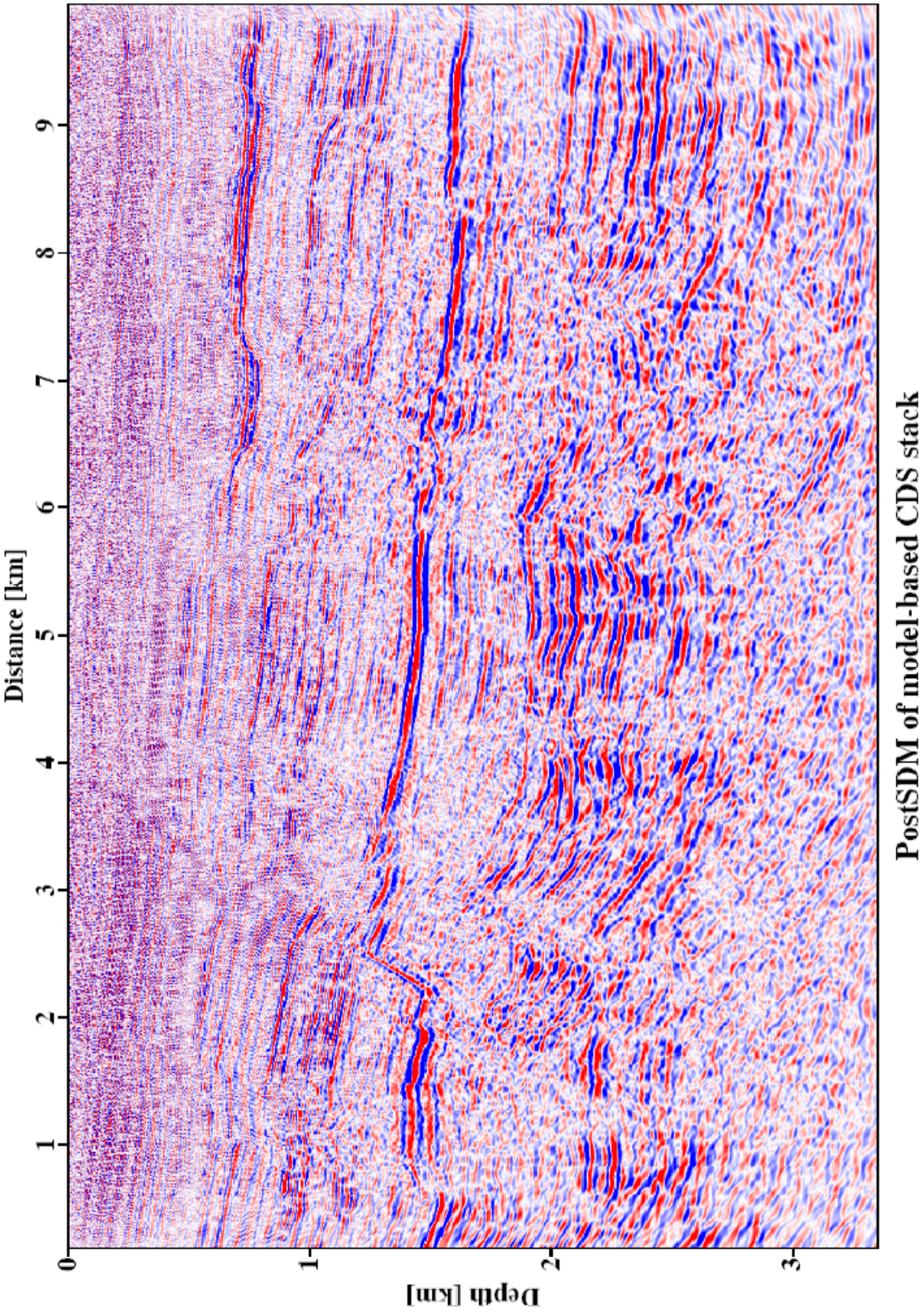

Figure 5.39: Kirchhoff poststack depth migration result for the model-based CDS stacked section shown in Figure 5.30.

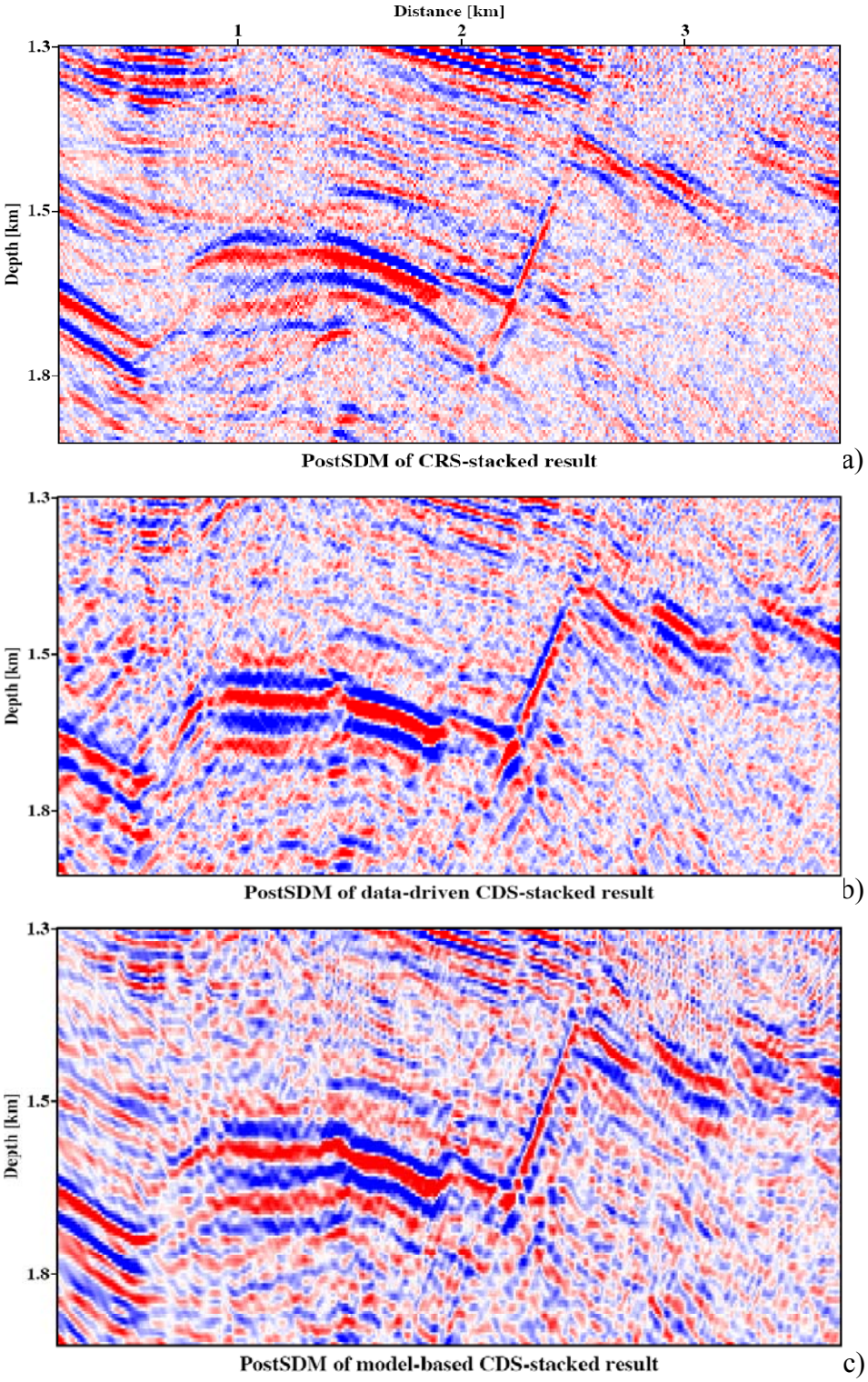

Figure 5.40: Three subsections from the migration results of the different stack sections. a) The CRS stack migrated subsection b) Data-driven CDS stack migrated subsection and c) Model-based CDS stack migrated subsection.

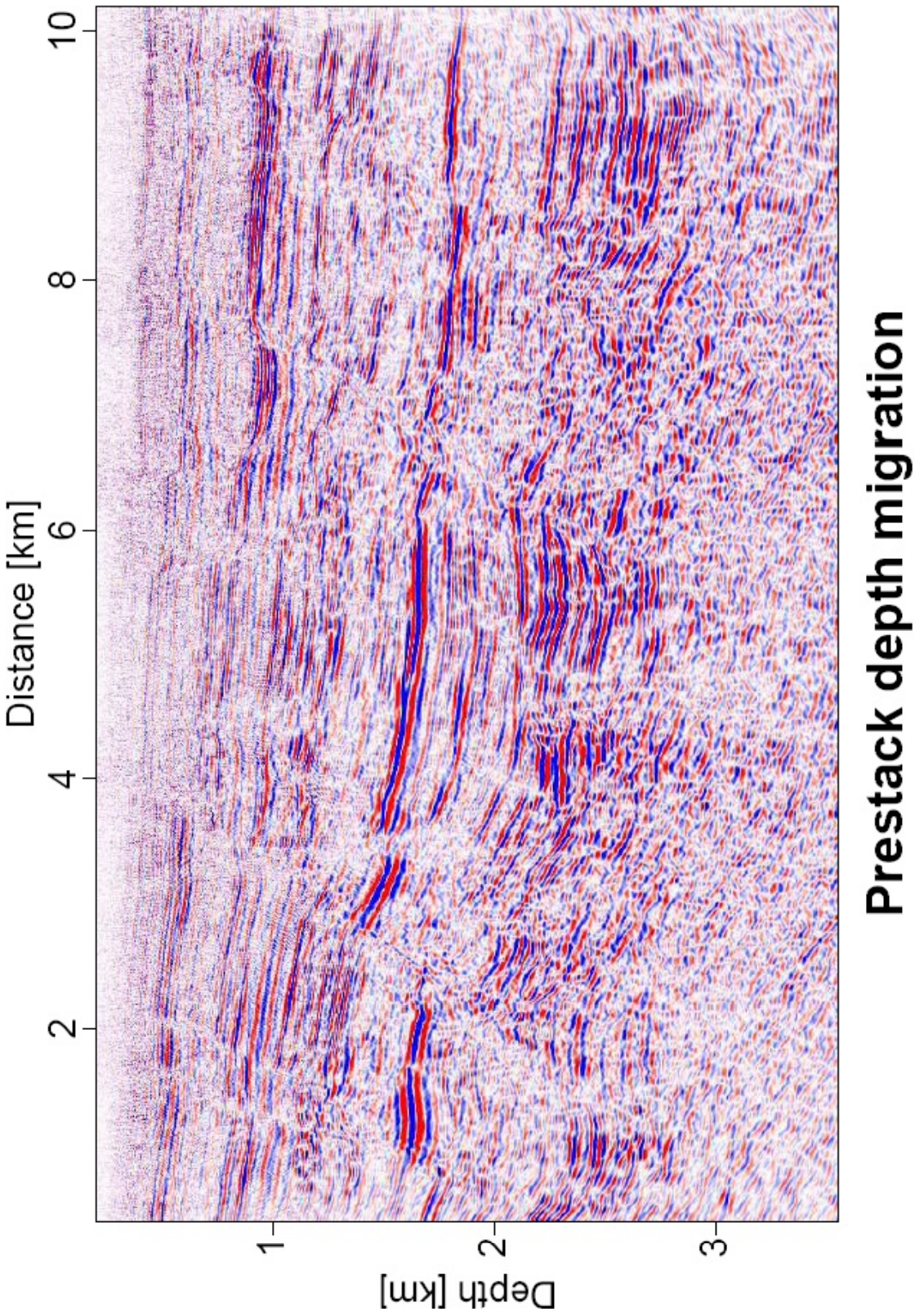

Figure 5.41: Prestack Kirchhoff depth migration result with high similarity to the poststack result shown in Figure 5.39.

Chapter 6

Conclusion and outlook

Stacking has been used in seismic data processing for a long time. The work on stacking techniques continues to improve the stacks by trying to take more of the subsurface complexity into account. In recent years, a new method called common-reflection-surface (CRS) stack has been introduced (Hubral et al. 1998; Müller, 1998). The CRS stack method considers far more traces than those present in an individual CMP gather. Hence, the results show a significant increase in signal-to-noise ratio as compared to a conventional stack. Müller(1999) introduced a pragmatic search strategy to determine the stacking parameters of the CRS operator. The pragmatic search strategy only considers the most dominant event for stack. For this reason the pragmatic search strategy fails to address the conflicting dip situations. To consider the conflicting dip situations, Mann (2002) proposed an extended search strategy that considers more than one event contributing to the simulation of a ZO sample. This extended search strategy solved the problem of confliction dips to some extent. However, the lack of a reliable criterion to identify the number of conflicting dips causes a variation of the number of contributions to neighboring samples which, in turn, cause artifacts in subsequent processing steps. Soleimani (2009) introduced a method termed common-diffraction-surface (CDS) stack by merging the concept of dip-moveout (DMO) correction and the CRS stack procedure. Although this method addresses conflicting dip situations to full extent, it is very time consuming due to the extensive coherence analysis required to determine all stacking parameters for all CDS operators.

In this thesis, I have introduced a new model-based approach to the CDS stack method. This method is intended to fully resolve the conflicting dip problem occurring in complex data and, thus, to allow to simulate a complete stacked section containing all mutually interfering reflection and/or diffraction events. The method makes use the principles of ray theory to forward calculate the parameters of CDS

operator directly in a velocity model. The required macro-velocity model can be generated with any inversion method, including the sequential application of CRS stack and normal-incidence-point (NIP) wave tomography. For the Sigsbee 2A data presented here, I used a simplified version of the migration velocity model distributed with the data, whereas for the real data set I revisited the macro-velocity generated by NIP-wave tomography (Hertweck et al., 2004).

In fact the model-based CDS stack is tailored to optimize the stacked section for a subsequent poststack depth migration. This is relevant for situations in which the generation of velocity models sufficiently accurate for prestack depth migration is difficult or even impossible. For both data, synthetic and real data, I demonstrated that the model-based CDS stack allows to generate a poststack-migrated section very similar to the corresponding prestack migration result. The latter process usually requires a more accurate macro-velocity model. The new approach yields even better results than the data-driven approach in a significantly shorter computation time. For the real data set, the sequence CRS stack/NIP-wave tomography/prestack-migration works almost perfectly. The combination of complex structures due to faults embedded in an almost 1-D background velocity trend is indeed ideal for this processing sequence. Therefore, the sequence model-based CDS stack/poststack-migration has not shown a very distinct advantage for these data. In order to reveal the ability of the model-based CDS approach I propose to apply this new approach to more complex data where model building for prestack depth migration is more difficult.

As in model-based CDS stack procedure the coherence values are stored during the process, it is possible to use these values as threshold criteria to accept or reject a CDS operator for the stack. This is expected to increases the signal-to-noise ratio of the simulated ZO section. In addition, by applying the coherence as a weigh factor for the individual contributions to the stack may further optimize the stack results.

The model-based CDS stack can be integrated into the CRS imaging workflow in situations where the result of NIP-wave tomography might not be sufficiently accurate to perform a prestack depth migration: as schematically shown in Figure 6.1, prestack migration might be replaced by a sequence of model-based CDS stack and poststack migration. In this way, it is possible to overcome to the former deficiencies of the CRS stack section which lead to gaps and artifacts in the poststack migration result.

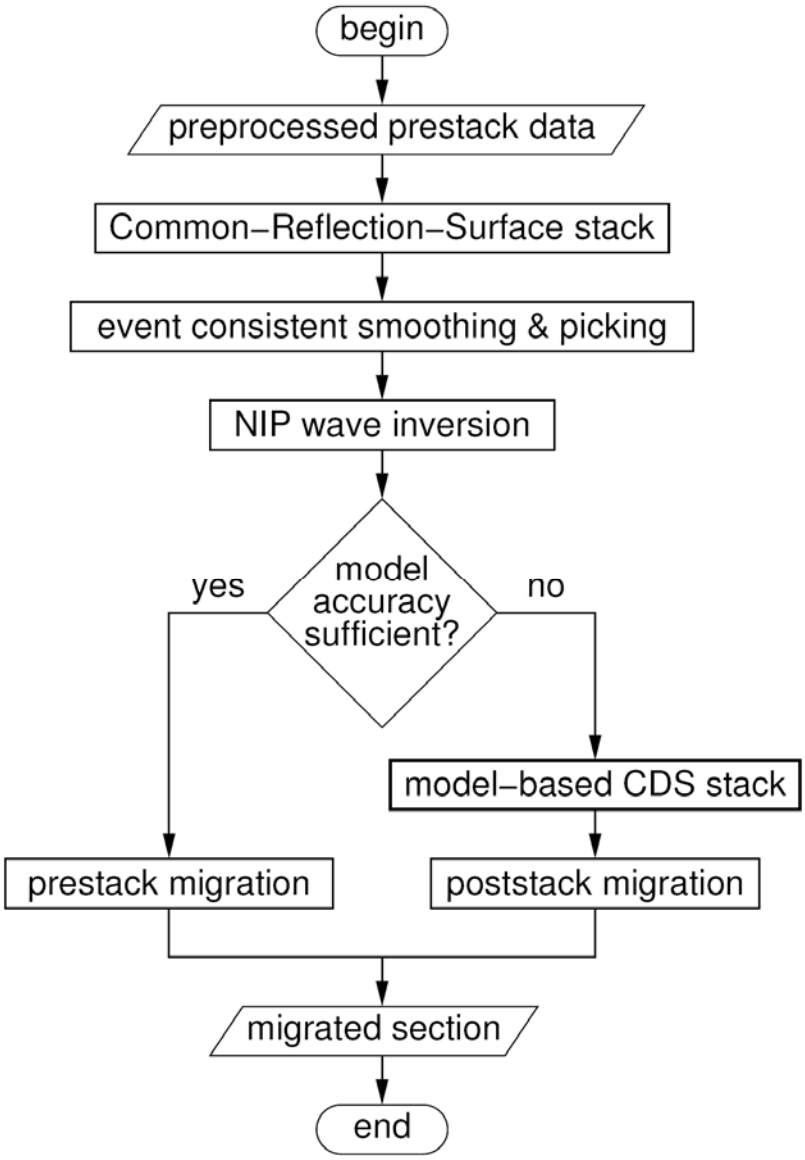

Figure 6.1: Processing flowchart with an alternative to prestack migration using the model-based CDS stack plus poststack depth migration.

Appendix A

Explanations

Here a brief summary of technical terms in geophysics, especially in reflection seismic have been gathered.

- **Common-depth-point (CDP):**
  In multichannel reflection profiling, the unique point on an individual reflector from which seismic reflection information is recorded in traces at different offsets. A set of traces containing information of one CDP is called a CDP gather. For horizontal reflectors, a CDP gather and a CMP gather are identical, but the reader should notice that for dipping reflectors the identity is no longer valid.

- **Common-midpoint (CMP):**
  A shot-receiver configuration where shots and receivers have different offsets but always the same midpoint position between them. A set of traces containing information for one CMP is called a CMP gather.

- **Common-offset (CO):**
  A shot-receiver configuration where the shot and the receiver have a constant offset. A seismic CO gather can be obtained when the whole configuration moves along the seismic profile it is a side-by-side display of traces which have the same offset.

- **Common-receiver (CR):**
  Another shot-receiver configuration which is in contrast to common-shot (CS). The shot moves along the seismic profile while the receiver always remains at the same position. All traces recorded for one specified receiver form a CR gather.

- **Common-shot (CS):**
  The most frequently used shot-receiver configuration in practical field recording. The receiver moves along the seismic profile while the shot always remains at the same position. All traces recorded for one specified shot form a CS gather.

- **Common reflection surface (CRS) stack:**
  Based on three-parametric traveltime expansion formulas, the CRS stack provides a velocity model independent stacking procedure. As a result, one obtains an enhanced simulated zero offset section (compared to standard imaging processes like CMP/stack or NMO/DMO/stack procedures), and several wavefield attributes which may be used for further calculations.

- **Diffraction:**
  Scattered seismic energy which emanates from an abrupt discontinuity of rock type, particularly common where faults cut reflecting interfaces.

- **Dip:**
  The angle which a reflector or refractor makes with the horizontal.

- **Exploding reflector:**
  A theoretical experiment which produces a seismic zero offset (ZO) section. Think of a reflector within the subsoil. If this reflector suddenly explodes, waves will travel up to the earth's surface where they are observed. If all model velocities are halved according to their true values, the recorded section will be a ZO section with true two-way traveltimes.

- **Gather:**
  A display of the input data to a stacking process rearranged that all the seismic traces corresponding to some criterion are displayed side-by-side.

- **Geometrical spreading:**
  The amplitude of a moving wave emanating from a point source changes with time and position due to the fact that the wavefront diverges or converges, in other words, the energy of the wavefield spreads over a continuously changing area. In a homogeneous medium, energy density decays proportional to, where is the radius of the wavefront produced by a point source. The wave amplitude is proportional to the square root of energy density, i.e. the amplitude decays as. For non-homogeneous media, e.g. layered structures, the effect is more difficult to describe but can be calculated by dynamic ray tracing.

- **Homogeneity:**
  Uniformity of a physical property throughout a material; opposite of inhomogeneity.

- **Imaging:**
  Any seismic process that transforms one seismic reflector image into another, including not only data transformation between time and depth domain but also transformations within the same domain. The most widely investigated imaging process is seismic migration. The dynamic as well as the kinematic aspects have to be treated correctly, i.e. imaging implies the term true-amplitude.

- **Inhomogeneity:**
  Lack of a spatial uniformity of a physical property, also called heterogeneity; opposite of homogeneity.

- **Isotropy:**
  Having the same physical properties regardless of the direction in which they are measured; opposite of anisotropy.

- **Macro-model:**
  Model of the subsoil containing only large scale features (with respect to the seismic wavelength). The most frequently used term is "macro-velocity model". This model is needed for the migration processes and must be estimated in advance.

- **Migration, pre-stack migration, post-stack migration:**
  Migration is a method of reconstructing a seismic time section so that dipping reflection events are repositioned to lie beneath their true surface locations and at corrected vertical two-way traveltimes (time migration). If the output is in the depth domain, the process is called depth migration. Usually, the geophysicist distinguishes between migration before (pre-stack migration) and after (post-stack migration) a stacking process.

- **Migration to zero offset (MZO):**
  The term "migration to zero offset" defines a process which produces a zero offset (ZO) section out of a common-offset (CO) section. For homogeneous media, MZO can be seen as a sum of normal moveout (NMO) and dip moveout (DMO) correction processes.

- **Moveout, Normal moveout (NMO), Dip moveout (DMO):**
  Generally, moveout is the difference between the two-way traveltimes of reflected energy detected at two receiver offset distances in a CMP gather. Normal moveout is the difference in two-way traveltime between the reflection event at an offset position x($t = t_x$) and a zero offset ($t = t_0$), such that ($\Delta t_{NMO} = t_x - t_0 \approx x^2/2v_{RMS}^2 t_0$), where v_{RMS} is the root-mean-square velocity of the media above the reflector. This assumes that the reflection events have a hyperbolic shape in the CMP gather. In case of a planar dipping reflector, dip moveout is the difference between the moveout up-dip and down-dip, proportional to the angle of dip θ such that, ($\Delta t_{DMO} = 2x \sin\theta / v_{RMS}$)where x is the offset distance from the midpoint (half-offset). The result of a moveout-corrected CMP gather is a simulated ZO section.
- **Multiple:**

  Seismic energy which has been reflected more than once.

- **Multiple coverage:**
  Seismic arrangement whereby the same portion of the subsurface is involved in several records. The redundancy of measurements permits various types of noise to be attenuated in processing.

- **Noise:**
  Noise is a signal that conveys no useful information. If the useful signal comprises data that are being recorded, random (white) noise can be reduced by summing the recorded signals. Incoherent noise is effectively damped out and the coherent signal is enhanced, thus improving the signal-to-noise ratio. The definition of noise depends on the problem because "one man's noise is another man's signal.

- **Normal incidence:**
  A wavefront striking an interface broadside that the angle between the wavefront and the interface is zero. In ray theory, normal incidence requires a ray to be perpendicular to an interface at the intersection point.

- **Offset:**
  The distance between a receiver position (or the center of a receiver group) and the shot position.

- **Primary reflection:**
  Seismic energy which has been reflected only once and hence is not a multiple.

- **Profile:**
  A seismic profile is a line (2D experiments) or an array (3D experiments) at the surface where data is acquired by several measurements.

- **Ray theory:**
  A special theory to describe the propagation of a wavefield within the earth. Ray theory is based on a high-frequency approximation of the elastodynamic equation and is liable to certain restrictions. Details can be found in chapter 2.

- **Ray tracing:**
  Determining the arrival times (kinematic ray tracing) and amplitudes (dynamic ray tracing of seismic body waves at detector locations by following ray paths which obey Snell's law through a model for which the velocity distribution is known.

- **Receiver:**
  A device used to detect the arrival of seismic waves by transforming the ground motion (geophone; land seismic) or the pressure fluctuations (hydrophone; marine seismic) into an electrical voltage.

- **Reflection:**
  The energy or wave from a shot or other seismic sources which has been reflected (returned) from a reflector or series of contrasts within the earth.

- **Reflector:**
  A contrast in acoustic impedance which gives rise to a seismic reflection

- **Shot:**
  A source of seismic shock waves that are produced for experimental purposes, e.g. by a hammer, an explosion, an airgun, or a water gun. Guns in marine seismic use high pressure air to produce a pressure wave.

- **Signal-to-noise ratio (SNR):**
  The energy of desired events divided by all remaining energy (noise) at that time.

- **Stacking:**
  The summing of traces from a variety of seismic records to increase the signal-to-noise ratio and enhance coherent signals into a composite record. The most frequently used stacking process is the CMP stack. To obtain a CMP stacked section (which in fact is nothing else than a simulated ZO section), all traces, which correspond to the same common-midpoint but which originate from different seismic profiles and different offsets, are summed up. This technique reduces not only the amplitude of incoherent noise, but also multiples with their different normal moveout.

- **Trace:**
  A recorded seismic dataset for one channel (receiver).

- **Zero offset (ZO):**
  Theoretical shot-receiver configuration where a receiver position coincides with the shot position. This configuration cannot be used in field recording, i.e. it must be calculated from other shot-receiver configurations, e.g. by migration to zero offset (MZO) or common-midpoint (CMP) stacking. A seismic ZO section with traces corresponds to (theoretical) experiments.

Appendix B
Used hardware and software

All the results of CDS (both data-driven and model-based) stack shown in this thesis were processed on PC with 2.6 GHz Intel Pentium 4 processor, 1GB RAM, and the operating system SuSE Linux 10.2. The model-based CDS stack implementation is entirely written in C++ (Stroustrup, 1997) and requires the standard libraries as well as the Standard Template Library (STL).The code was compiled with the GNU project C++ compiler version 4.1.2.

Additional data processing and most of the data visualization, on screen as well as in PostScript format, was performed with various utilities of the Seismic Un*x package (Cohen and Stockwell, 2000). Further information about Seismic Un*x can be found in Stockwell (1997) and Stockwell (1999).

The Green's function tables for both real and Sigsbee 2A data were computed by means of the Madagascar package(see http:www.reproducibility.org). The post-stack depth migrations based on this GFT were performed with Uni3D, a true-amplitude migration and demigration software developed at the Geophysical Institute, University of Karlsruhe.

I wrote the kinematic and the dynamic ray tracing codes in MATLAB 2009b (www.mathworks.com) in advance then converted these codes to the C++ language. Some of the figures are also generated in MATLAB 2009b. The thesis itself is written in Microsoft Office 2007.

Appendix C
Example of output of the program

```
             *****  crsstack  *****

by Juergen Mann, Baerbel Traub, Alex Gerst, and Hashem shahsavani
       Juergen.Mann@gpi.uni-karlsruhe.de

Seconds | Info/Warning/Error Messages
---------------------------------------------------------------------


      0 | I: *** GENERAL PARAMETERS ***

      0 | I: Execution mode: model-based CDS stack, exit.
      0 | I: Maximum emergence angle for search: 30
      0 | I: Minimum emergence angle for search: -30
      0 | I: Increment of emergence angle: 1
      0 | I: Opening input file ../Test/suedfilt.su...
      0 | I: Expecting 28351 traces with 2500 samples.
      0 | I: Reading trace headers from file ../Test/suedfilt.su...
      0 | I: Fitting 2D profile to data geometry...
      0 | I: Number of linear regression iterations: 1
      0 | I: *** GEOMETRY OF INPUT DATA SET ***
      0 | I: 2D profile normal unit vector: (0, 1).
      0 | I: 2D profile relative reference point: (0, 0)
      0 | I: Minimum of 1D CMP coordinate: 0
      0 | I: Maximum of 1D CMP coordinate: 10647.5
      0 | I: Minimum distance between CMPs and profile: 0
      0 | I: Maximum angular deviation: 0
      0 | I: Minimum offset: 0
      0 | I: Maximum offset: 4001
      0 | I: *** TRACE DISCRIMINATION PARAMETERS ***
      0 | I: Maximum distance between CMP and profile: 3.40282e+38
      0 | I: Maximum angular deviation: 90
      0 | I: Maximum of angular deviation * offset: 3.40282e+38
      0 | I: Smallest offset to consider: 0
      0 | I: Largest offset to consider: 3.40282e+38
      0 | I: Building linked CDP no./offset list...
      0 | I: Skipped 0 of 28351 traces.
      0 | I: Geometry mapped to 427 CDP bins.
      0 | I: *** GEOMETRY OF TARGET ZONE ***
      0 | I: Number of target traces: 391
      0 | I: Number of samples per target trace: 1450
      0 | I: Temporal target sampling: 0.002
      0 | I: Time offset in target traces: 0.1
      0 | I: First CDP number in target zone: 420
      0 | I: Last CDP number in target zone: 810
      0 | I: Number of CDPs to be skipped between target traces: 0
      0 | I: *** APERTURE PARAMETERS ***
      0 | I: Smallest aperture in ZO section: 1000
```

```
      0 | I: Largest aperture in ZO section: 1000
      0 | I: Mean frequency of wavelet: 30
      0 | I: Average model velocity: 3000
      0 | I: Smallest aperture in CMP gather: 200
      0 | I: Traveltime related to this aperture: 0.2
      0 | I: Largest aperture in CMP gather: 2000
      0 | I: Traveltime related to this aperture: 2
      0 | I: Relative taper size: 0.3
      0 | I: *** MODEL-BASED CDS STACK PARAMETERS ***
      0 | I: Time stepping factor for ray tracing: 5
      0 | I: First model trace corresponds to CDP: 402
      0 | I: Last model trace corresponds to CDP: 828
      0 | I: Lateral padding to the left 30 grid points.
      0 | I: Lateral padding to the right 5 grid points.
      0 | I: Velocity model file: paddedmodel.su
      0 | I: Disallowing turning rays.
      0 | I: Parameter parsing completed.
      0 | I: Launching model-based CDS stack...
      0 | I: Allocating regular target zone for pseudo time
migration...
      0 | I: Opening input file paddedmodel.su...
      0 | I: Expecting 533 traces with 180 samples.
      0 | I: Reading trace headers from paddedmodel.su...
      0 | I: Lateral velocity model spacing: 20.0141
      0 | I: (Padded) number of lateral velocity samples: 569
      0 | I: Vertical velocity model spacing: 20
      0 | I: Number of vertical velocity samples: 180
      0 | I: Relative coordinate of first model trace: -600.423
      0 | I: Closing input file paddedmodel.su...
      0 | I: Opening output file no_turn_30.MbCDSstack...
      0 | I: Opening output file no_turn_30.MbCDStraces...
      0 | I: Opening output file no_turn_30.MbCDSnoOper...
      0 | I: Opening output file no_turn_30.MbCDSmaxCoh...
      0 | I: Opening output file no_turn_30.MbCDSmaxRnip...
      0 | I: Opening output file no_turn_30.MbCDSmaxAngle...
      0 | I: Stacking trace no. 1 of 391. Traces in core: 1807
     36 | I: Stacking trace no. 11 of 391. Traces in core: 2206
     79 | I: Stacking trace no. 21 of 391. Traces in core: 2581
    126 | I: Stacking trace no. 31 of 391. Traces in core: 2893
    176 | I: Stacking trace no. 41 of 391. Traces in core: 3088
    229 | I: Stacking trace no. 51 of 391. Traces in core: 3210
    284 | I: Stacking trace no. 61 of 391. Traces in core: 3200
    339 | I: Stacking trace no. 71 of 391. Traces in core: 3162
    395 | I: Stacking trace no. 81 of 391. Traces in core: 3164
    451 | I: Stacking trace no. 91 of 391. Traces in core: 3183
    506 | I: Stacking trace no. 101 of 391. Traces in core: 3180
    560 | I: Stacking trace no. 111 of 391. Traces in core: 3174
    613 | I: Stacking trace no. 121 of 391. Traces in core: 3175
    667 | I: Stacking trace no. 131 of 391. Traces in core: 3187
    720 | I: Stacking trace no. 141 of 391. Traces in core: 3214
    773 | I: Stacking trace no. 151 of 391. Traces in core: 3224
    826 | I: Stacking trace no. 161 of 391. Traces in core: 3233
    879 | I: Stacking trace no. 171 of 391. Traces in core: 3239
    932 | I: Stacking trace no. 181 of 391. Traces in core: 3230
    986 | I: Stacking trace no. 191 of 391. Traces in core: 3224
   1039 | I: Stacking trace no. 201 of 391. Traces in core: 3220
   1092 | I: Stacking trace no. 211 of 391. Traces in core: 3201
   1144 | I: Stacking trace no. 221 of 391. Traces in core: 3184
   1196 | I: Stacking trace no. 231 of 391. Traces in core: 3174
   1248 | I: Stacking trace no. 241 of 391. Traces in core: 3159
   1302 | I: Stacking trace no. 251 of 391. Traces in core: 3151
```

```
   1355 | I: Stacking trace no. 261 of 391. Traces in core: 3155
   1408 | I: Stacking trace no. 271 of 391. Traces in core: 3164
   1461 | I: Stacking trace no. 281 of 391. Traces in core: 3161
   1514 | I: Stacking trace no. 291 of 391. Traces in core: 3166
   1565 | I: Stacking trace no. 301 of 391. Traces in core: 3163
   1616 | I: Stacking trace no. 311 of 391. Traces in core: 3159
   1666 | I: Stacking trace no. 321 of 391. Traces in core: 3170
   1715 | I: Stacking trace no. 331 of 391. Traces in core: 3126
   1762 | I: Stacking trace no. 341 of 391. Traces in core: 3039
   1805 | I: Stacking trace no. 351 of 391. Traces in core: 2880
   1845 | I: Stacking trace no. 361 of 391. Traces in core: 2615
   1879 | I: Stacking trace no. 371 of 391. Traces in core: 2279
   1907 | I: Stacking trace no. 381 of 391. Traces in core: 1885
   1927 | I: Stacking trace no. 391 of 391. Traces in core: 1476
   1928 | I: Closing output file no_turn_30.MbCDSstack...
   1928 | I: Closing output file no_turn_30.MbCDStraces...
   1928 | I: Closing output file no_turn_30.MbCDSnoOper...
   1928 | I: Closing output file no_turn_30.MbCDSmaxCoh...
   1928 | I: Closing output file no_turn_30.MbCDSmaxRnip...
   1928 | I: Closing output file no_turn_30.MbCDSmaxAngle...
   1928 | I: Number of samples lost during migration: 3000145
   1928 | I: Model-based CDS stack completed.
   1928 | I: Opening output file no_turn_30.MbCDSPTM...
   1928 | I: Writing output file no_turn_30.MbCDSPTM...
   1928 | I: Closing output file no_turn_30.MbCDSPTM...
   1929 | I: Closing input file ../Test/suedfilt.su...
Process terminated after 32.15 minutes (user plus system time)
```

References

Aki, R., Richards, P. (1980). Quantitative Seismology: Theory and methods, volume 1. Freeman and Company, New York.

Ben-Menahem, A. and Beydoun, W. B. (1985a). Range of validity of seismic ray and beam methods in general inhomogeneous media . I. general theory. Geophys. J. R. astr. Soc., 82:207-234.

Ben-Menahem, A. and Beydoun, W. B. (1985b). Range of validity of seismic ray and beam methods in general inhomogeneous media . II. a canonical problem. Geophys. J. R. astr. Soc., 82:235-262.

Beydoun, W. B., and Keho, T. H. (1987). The paraxial ray method. Geophysics, 52(12):1639-1653.

Bleistein, N. (1984). Mathematical Methods for Wave Phenomena. Academic Press Inc., New York.

Bortfeld, R. (1989). Geometrical ray theory: Rays and traveltimes in seismic systems (second-order approximations of the traveltimes). Geophysics, 54(3):342-349.

Butcher, J., C. (1993). Numerical methods for ordinary differential equations. The University of Auckland, New Zealand.

Červený, V. (1972). Seismic Rays and Ray Intensities in Inhomogeneous Isotropic media. Geophys. J. R. astr. Soc. 29:1-13.

Červený, V. (1981a). Dynamic ray tracing in 2D media. Stanford Exploration Projects, 28:21-30.

Červený, V. (1981b). Determination of second derivatives of travel-time field by dynamic ray tracing. Stanford Exploration Projects, 28:31-38.

Červený, V. (1981c). Ray tracing in a vicinity of a central ray. Stanford Exploration Projects, 28:39-48.

Červený, V. and Hron, F. (1980). The ray series method and dynamic ray-tracing system for threedimensional inhomogeneous media. Bull. Seis. Soc. Am., 70:47-77.

Červený, V. (2001). Seismic Ray Theory: Cambridge University Press.

Červený, V., Klimes, L., and Pšenčík, I. (1984). Paraxial ray approximation in the computation of seismic wavefields in inhomogeneous media. Geophys. J. R. astr. Soc., 79:89-104.

Červený, V., Pšenčík, I. (1979). Ray amplitudes of body waves in laterally inhomogeneous media. Geophys. J. R. astr. Soc., 57:91-106.

Cohen, J. K. and Stockwell, J. J. W. (2000). CWP/SU: Seismic Unix Release 34: a free package for seismic research and processing. Center for Wave Phenomena, Colorado School of Mines.

Deregowski, S. M. (1986). What is DMO? First Break, 4(7):7-24.

Deregowski, S., M., Rocca, F. (1981). Geomatriacal optics and wave theory of constant offset section in layered media. Geophys. Prosp., 29(3):374-406.

Duveneck, E. (2004a). 3D tomographic velocity model estimation with kinematic wavefield attributes. Geophys. Prosp., 52(6):535-545.

Duveneck, E. (2004b). Velocity model estimation with data-derived wavefront attributes. Geophysics, 69(1):265-274.

Duveneck, E. (2004c). Tomographic determination of seismic velocity models with kinematic wavefield attributes. Logos Verlag, Berlin.

Garabito, G., Cruz, J. C., Hubral, P., and Costa, J. (2001a). Common reflection surface stack: A new parameter search strategy by global optimization. In Expanded abstracts, 71st Ann. Internat. Mtg., pages 2009–2012. Soc. Expl. Geophys.

Garabito, G., Cruz, J. C. R., Hubral, P., and Costa, J. (2001b). Common reflection surface stack: a new parameter search strategy by global optimization. In Ann. Report, volume 4, pages 35–48. Wave Inversion Technology Consortium.

Gelchinsky, B., Berkovitch, A., and Keydar, S. (1999a). Multifocusing homeomorphic imaging -Part 1. Basic concepts and formulas. J. Appl. Geophys., 42(3,4):229-242.

Gelchinsky, B., Berkovitch, A., and Keydar, S. (1999b). Multifocusing homeomorphic imaging -Part 2. Multifold data set and multifocusing. J. Appl. Geophys., 42(3,4):243-260.

Hale, D. (1991). Dip Moveout Processing. Soc. Expl. Geophys., Tulsa.

Heilmann, Z., Mann, J., Duveneck, E., and Hertweck, T. (2004). CRS-stack-based seismic reflection imaging – a real data example. In Extended abstracts, 66th Conf. Eur. Assn. Geosci. Eng. Session P211.

Hertweck, T., Jäger, C., Mann, J., Duveneck, E., and Heilmann, Z. (2004). A seismic reflection imaging workflow based on the Common-Reflection-Surface (CRS) stack: theoretical background and case study. In Expanded Abstracts, 74th Ann. Internat. Mtg. Soc. Expl. Geophys. Session SP 4.3.

Hertweck, T., Mann, J., and Klüver, T. (2005). Event-consistent smoothing in the context of the CRS stack method. J. Seis. Expl., 14(2-3):197-215.

Hertweck., T. (2000). Practical aspects of the unified approach to seismic imaging. Master's thesis, University of Karlsruhe.

Hertweck, T., Schleicher, J., and Mann, J. (2007). Data-stacking beyond CMP. The Leading Edge, 26(7):818–827.

Herzberger, M. (1958). Modern Geometrical Optics. Interscience, New York.

Hille, E. (1997). Ordinary differential equations in the complex domain, New York, Dover Publications.

Höcht, G., de Bazelaire, E., Majer, P., and Hubral, P. (1999). Seismics and optics: hyperbolae and curvatures. J. Appl. Geoph., 42(3,4):261-281.

Hubral, P. (1983). Computing true amplitude reflections in a laterally inhomogeneous earth. Geophysics, 48(8):1051-1062.

Hubral, P., and Krey, T. (1980). Interval velocities from seismic reflection time measurements: Soc. of Expl. Geophys.

Hubral, P., Höcht, G., Jäger, R. (1998). An introduction to the common-reflection-surface stack. 60th Conf. Eur. Assn. Geosci. Eng.

Hubral, P., Schleicher, J., and Tygel, M. (1992). Three-dimensional paraxial ray properties, Part I: Basic relations. J. Seis. Expl., 1:265-279.

Hubral, P., Tygel, M., and Schleicher, J. (1995). Geometrical-spreading and ray-caustic decomposition of elementary seismic waves. Geophysics, 60(4):1195-1202.

Jäger, R. (1999). The Common Reflection Surface stack - theory and application. Master's thesis, University of Karlsruhe.

Jäger, R., Mann, J., Höcht, G., and Hubral, P. (2001). Common-Reflection-Surface stack: image and attributes. Geophysics, 66(1):97-109.

Kearey, P., Brooks, M., Hill, I. (2002). An introduction to geophysical exploration. Blackwell Science Ltd, Third edition.

Klüver, T. (2007). Velocity model building using analytic and model-based diffraction traveltime functions. Master's thesis, University of Karlsruhe.

Koglin, I., (2001). Picking and smoothing of seismic events and CRS attributes, application for inversion. Master's thesis, University of Karlsruhe.

Koglin, I. (2005). Estimation of residual static time shifts by means of the CRS-based residual static correction approach. Logos Verlag, Berlin.

Kravtsov, Y. A., Orlov, Y. I. (1990). Geometrical optics of inhomogeneous media. Springer Verlag, Berlin.

Landa, E., Gurevich, B., Keydar, S., and Trachtman, P. (1999). Application of multifocusing method for subsurface imaging. J. Appl. Geophys., 42(3,4):283-300.

Majer, P. (2000). Inversion of seismic parameters: determination of the 2-D iso-velocity layer model. Master's thesis, University of Karlsruhe.

Majer, P., Höcht, G., Mann, J., and Vieth, K.-U. (2000). Inversion by means of kinematic wavefield attributes. In Ann. Report, volume 3, pages 39-49. Wave Inversion Technology Consortium.

Mann, J. (1997). Derivation and implementation of the seismic image wave theory and its application to seismic reflection data. Master's thesis, University of Karlsruhe.

Mann, J. (2000). Common-reflection-surface stack (user's manual): Geophysical Institute, University of Karlsruhe, 4.1b edition.

Mann, J. (2001). Common-Reflection-Surface stack and conflicting dips. In Extended abstracts, 63rd Conf. Eur. Assn. Geosci. Eng. Session P077.

Mann, J. (2002). Extensions and applications of the Common-Reflection-Surface Stack method. Logos Verlag, Berlin.

Mann, J., Duveneck, E., Hertweck, T., and Jäger, C. (2003). A seismic reflection imaging workflow based on the Common-Reflection-Surface stack. J. Seis. Expl., 12(3):283-295.

Mann, J., Hubral, P., Traub, B., Gerst, A., and Meyer, H. (2000). Macro-model independent approximative prestack time migration. In Extended abstracts, 62th Conf. Eur. Assn. Geosci. Eng. Session B-52.

Mann, J., Jäger, R.,Müller, T., Höcht, G., Hubral, P. (1999). Common-reflection-surface stack- a real data example. J. Appl. Geoph., 42(3,4):301-318.

Mann, J., Zhang, Y. (2003). Data-driven imaging with second-order traveltime approximations-traveltime derivatives and kinematic wavefield attributes. 8th International Congress of the Brazilian Geophysical Society, Brazil.

Mayne, W. H. (1962). Common reflection point horizontal data stacking techniques. Geophysics, 27(6):927–938.

Müller, N.-A. (2007). Determination of interval velocities by inversion of kinematic 3D wavefield attributes. PhD thesis, University of Karlsruhe.

Müller, N.-A. (2006). Elimination of the spread-length bias in the Common-Reflection-Surface stack. In Expanded abstracts, 76th Ann. Internat. Mtg., P. 3006-3010. Soc. Expl. Geophys.

Müller, N.-A. (2005). 3-D inversion with kinematic wavefield attributes. In Extended abstracts, 67th Conf. Eur. Assn. Geosci. Eng. Session B040.

Müller., T. (1998). Common reflection surface stack versus NMO/stack and NMO/DMO stack . 60th Conf. Eur. Assn. Geosci. Eng.

Müller, T. (1999). The Common Reflection Surface Stack Method - Seismic imaging without explicit knowledge of the velocity model. PhD thesis, University of Karlsruhe.

Neidell, N. S. and Taner, M. T. (1971). Semblance and other coherency measures for multichannel data. Geophysics, 36(3):482-497.

Nelder, J. A., and Mead, R. (1965). A simplex method for function minimization: Computer Journal. 7:308-313.

Perroud, H., Hubral, P., Höcht, G., and de Bazelaire, E. (1997). Migrating around in circles – part III. The Leading Edge. 16(6):875-883.

Pfaffenholz, J. (2001). Sigsbee2 synthetic subsalt data set: image quality as function of migration algorithm and velocity model error. In Workshop on velocity model independent imaging for complex media, Extended abstracts. Soc. Expl. Geophys. Session W5-5.

Popov, M. M., Pšenčík, I. (1978). Computation of ray amplitudes in inhomogeneous media with curved interfaces. Studia Geoph. et Geod. 22:248-58.

Popov, M., Oliveira, S. (1997). Some limitations for the applicability of the ray method in elastodynamics. Revista Brasileira de Geofisica, 15(3):226-236.

Schleicher, J., Tygel, M., and Hubral, P. (1993). Parabolic and hyperbolic paraxial two-point traveltimes in 3D media. Geophys. Prosp., 41(4):495–514.

Soleimani, M., Mann, J., Adibi Sedeh, E., and Piruz, I. (2010). Improving the seismic image quality in semi-complex structures in North East Iran by the CDS stack method. In Extended abstracts, 72nd Conf. Eur. Assn. Geosci. Eng. Session P398.

Soleimani, M., Piruz, I., Mann, J., and Hubral, P. (2009a). Common-Reflection-Surface stack: accounting for conflicting dip situations by considering all possible dips. J. Seis. Expl., 18(3):271-288.

Soleimani, M., Piruz, I., Mann, J., and Hubral, P. (2009b). Solving the problem of conflicting dips in Common-Reflection-Surface stack. In Extended Abstracts, 1st Internat. Conf. & Exhib., Shiraz, Iran. Eur. Assn. Geosci. Eng.

Solymani., M. (2009). Common Diffraction Surface (CDS) stack; A new approach for solving the problem of conflicting dips. PhD thesis in Shahrood University of Technology, Shahrood.

Stockwell, J. J. W. (1997). Free software in education: a case study of CWP/SU: Seismic Un*x. The Leading Edge, 16(7):1045-1049.

Stockwell, J. J. W. (1999). The CWP/SU: Seismic Un*x Package. Computers and Geosciences, 25(4):415-419.

Stolt, R. H. (1978). Migration by Fourier transform. Geophysics, 43(1):23-48.

Stroustrup, B. (1997). The C++ Programming Language. Addison-Wesley, 3rd edition.

Taner, M. T., and Koehler, F. (1969). Velocity spectra. Digital computer derivation and applocations of velocity functions: Geophysics, 34(6):859-881.

Tygel, M., Müller, T., Hubral, P., and Schleicher, J. (1997). Eigenwave based multiparameter traveltime expansions. In Expanded abstracts, 67th Ann. Internat. Mtg., P. 1770–1773. Soc. Expl. Geophys.

Ursin, B. (1982). Quadratic wavefront and traveltime approximations in inhomogeneous layered media with curved interfaces: Geophysics, 47(7):1012-1021.

Vieth, K.-U. (2001). Kinematic wavefield attributes in seismic imaging. PhD thesis, University of Karlsruhe.

Yilmaz, Ö. (2001). Seismic data analysis. Soc. Expl. Geophys., Tulsa.

چکیده:

روش برانبارش بازتاب مشترک، حادثه های لرزه ای را با استفاده از یک آنالیز سرعت کلی برانبارش می نماید. روش معمول برانبارش سطح بازتاب مشترک دوبعدی، قادر است تعداد محدودی از حاثه های لرزه ای را که در یک نمونه از مقطع برانبارش شده تداخل نموده اند در نظر بگیرد. چنین پدیده ای که در اثر شرکت کردن دو یا چند حادثه در یک مقطع برانبارش شده دور افت صفر بوجود می آید، تداخل شیب می نامند. از آنجایی که معیار قابل اطمینانی به منظور مشخص کردن محل تداخل شیب ها وجود ندارد، مقطع برانبارش شده حاصل از روش فوق الذکر ممکن است در مراحل بعدی، یعنی کوچ، باعث ایجاد حوادثی مصنوعی گردد. این امر هنگام انجام کوچ قبل از برانبارش دشوار تر می گردد. زیرا برای انجام کوچ قبل از برانبارش، مدل سرعت لایه های زیر سطحی با دقت بالا مورد نیاز است. در چنین شرایطی ممکن است که ما به داده های حاصل از کوچ بعد از برانباش اعتماد کنیم.

علاوه بر روش فوق الذکر که تعداد محدودی از شیب ها را در نظر می گیرد، روشی که تعداد تقریبا پیوسته ای از شیب ها را در نظر می گیرد با ساده سازی روش برانبارش بازتاب مشترک معرفی شده است. این روش، روش برانبارش سطح پراش مشترک نامیده می شود. این نام به خاطر رابطه ای است این روش با حوادث مربوط به پراش ها دارد. این روش به شکل موفقیت آمیزی به صورت مبتنی بر داده بر روی داده های لرزه ای اجرا شده است و مشکل مربوط به تداخل شیب ها را تا حد زیادی مرتفع نموده است. زمان بسیار طولانی مورد نیاز برای پردازش داده های لرزه ای، یکی از بزرگ ترین مشکلات این روش است.

به منظور مرتفع کردن این روش در این رساله روشی مبتنی بر مدل ارائه شده است. این روش فقط نیاز به یک مدل سرعت صاف شده دارد که نیازی به دقت بالای آن نیست. در این رساله روش جدید معرفی شده بر روی داده های لرزه ای مصنوعی Sigsbee2A و داده های لرزه ای واقعی اجرا شده است. سپس داده های کوچ داده شده بعد از برانبارش حاصل از این روش، با روش های معرفی شده پیشین مقایسه شده اند. این نتایج نشان می دهد که روش معرفی شده جدید زمان پردازش بسیار اندکی دارد. با این وجود مقاطع برانبارش شده حاصل از این روش حتی در بعضی موارد نسبت به نتایج روش های پیشین بهبود یافته است.

شماره : ۵۰۰۱۸۰۶/۴۶/ش
تاریخ : ۹۰/۷/۱۷
ویرایش :

بسمه تعالی

دانشگاه صنعتی شاهرود

مدیریت تحصیلات تکمیلی

صورتجلسه دفاع از رساله دکتری (ph.D)

فرم شماره ۱۱

بدینوسیله گواهی می شود آقای .هشم شاهسونی..... دانشجوی دکتری رشته ..مهندسی اکتشاف معدن..... ورودی .مهر..... سال .....۱۳۸۶..... در تاریخ ....۱۳۹۰/۰۶/۱۷ ..... از رساله خود با عنوان : .....

..... A model based approach to the common diffraction surface stack.....

دفاع و با اخذ ..... به درجه : ..... نائل گردید .

۱۹/۵۰

الف) درجه عالی : نمره ۲۰-۱۹ ☒	ب) درجه بسیار خوب : نمره ۱۸/۹۹ – ۱۷ ☐
ج) درجه خوب : نمره۱۶/۹۹– ۱۵ ☐	د) غیر قابل قبول و نیاز به دفاع مجدد دارد ☐
ذ) رساله نیاز به اصلاحات دارد ☐	

ردیف	هیئت داوران	نام و نام خانوادگی	مرتبه علمی	امضاء
1	دکتر ایرج پیروز	استاد راهنما	استادیار	
2	دکتر Juegen Mann	استاد راهنما / مشاور	استادیار	
3	دکتر Peter Hubral	استاد راهنما / مشاور	پروفسور	
4	دکتر محمد مختاری	استاد مدعو داخلی / خارجی	استادیار	
5	دکتر ابولقاسم کامکار	استاد مدعو داخلی / خارجی	استادیار	
6	دکتر غلام جوان دولوئی	استاد مدعو داخلی / خارجی	استادیار	
	دکتر مهرداد سلیمانی	سرپرست (نماینده) تحصیلات تکمیلی دانشکده	استادیار	

مدیر محترم تحصیلات تکمیلی دانشگاه

ضمن تأیید مراتب فوق مقرر فرمائید اقدامات لازم بعمل آید

رئیس دانشکده و رئیس هیأت داوران :

تاریخ و امضاء

دانشکده معدن و ژئوفیزیک
دانشگاه صنعتی شاهرود

دانشگاه صنعتی شاهرود، دانشکده مهندسی معدن،
نفت و ژئوفیزیک

روش مبتنی بر مدل برانبارش سطح پراش مشترک

به منظورأخذ درجه دکتری از
دانشکده مهندسی معدن، نفت و ژئوفیزیک
دانشگاه صنعتی شاهرود

دانشجو:
هاشم شاهسونی

زمان برگزاری جلسه دفاع :	۱۳۹۰/۶/۱۷
استاد راهنمای اول :	جناب آقای دکتر پیروز
استاد راهنمای دوم :	جناب آقای دکتر یورگن مان
استاد مشاور :	جناب آقای پروفسور پیتر هوبرال